# INVESTIGATION OF CURVED COMPOSITE PANELS UNDER HIGH-G LOADING

by

Staci Nicole Jenkins

S. B., Aeronautics and Astronautics
Massachusetts Institute of Technology (1997)

Submitted to the Department of Aeronautics and Astronautics in Partial Fulfillment of the Requirements for the Degree of

Master of Science
in Aeronautics and Astronautics

at the

Massachusetts Institute of Technology
June 1999



Signature of Author .....
Department of Aeronautics and Astronautics
May 18, 1999

Approved by .....
Brent Appleby
Member of Technical Staff, Charles Stark Draper Laboratory
Thesis Supervisor

Certified by .....
S. Mark Spearing
Esther and Harold E. Edgerton
Assistant Professor of Aeronautics and Astronautics
Thesis Supervisor

Accepted by .....
Jaime Peraire
Associate Professor of Aeronautics and Astronautics
Chairman, Department Graduate Committee

# INVESTIGATION OF CURVED COMPOSITE PANELS UNDER HIGH-G LOADING

by

Staci Nicole Jenkins

Submitted to the Department of Aeronautics and Astronautics
on May 18, 1999 in Partial Fulfillment of the
Requirements for the Degree of Master of Science in
Aeronautics and Astronautics

## ABSTRACT

Numerical and experimental work was conducted to investigate the use of composites within the Wide Area Surveillance Projectile (WASP) wing system by specifically studying the buckling behavior of curved composite panels under high-g loading. A finite element model was developed as a design tool to model the original WASP wing as a constant thickness curved panel and to predict the buckling response of the panels. The model predicted the critical buckling loads and mode shapes of the composite panels. Experimentally, controlled axial compression tests and high-g tests were performed to determine the buckling response of the panels. The buckling response, including critical loads and mode shapes, was obtained for the controlled axial compression tests. The high-g tests demonstrated that composite panels are a viable option for structures in a high-g environment. All of the samples tested showed no signs of damage and no loss in load carrying capability. The results were used to study the effect of lay-up, curvature, aspect ratio (width to height), and height on the buckling response. The results of the finite element model and the controlled axial compression tests showed good agreement. However, they do not accurately capture the buckling response of the composite panels in the high-g environment.

Thesis Supervisor: Brent Appleby
Title: Member of Technical Staff, Charles Stark Draper Laboratory

Thesis Supervisor: S. Mark Spearing
Title: Esther and Harold E. Edgerton Assistant Professor of Aeronautics and Astronautics

# Foreword

This thesis was prepared at The Charles Stark Draper Laboratory, Inc., under IRAD.

Publication of this thesis does not constitute approval by Draper or the sponsoring agency of the findings or conclusions contained herein. It is published for the exchange and stimulation of ideas.

Permission is hereby granted by the Author to the Massachusetts Institute of Technology to reproduce any or all of this thesis.

This work was performed in the Technology Laboratory for Advanced Composites (TELAC) in the Department of Aeronautics and Astronautics at the Massachusetts Institute of Technology. This work was sponsored by the Charles Stark Draper Laboratory.

# Acknowledgments

The completion of this work would not have been possible without the tremendous support I have received from my co-workers and friends. First, I would like to thank Draper Laboratory for funding this research and giving me the opportunity to work on such a great project. Also special thanks to my advisors, Mark Spearing and Brent Appleby, for all your support and guidance.

I want to thank all those involved in the project: John Deyst, Charlie Boppe, Mark Drela, Carlos Cesnik, Tan Trinh, Josh Bernstein, Matt Burba, Ted Conklin, Cory Hallam, David Iranzo-Grues, Vlad Gavrilets, Garrett Shook, Torrey Radcliffe, Thierry Casiez, Sebastien Katch, Jean-Marc Hauss, and Rodney Chui. It was great to have the opportunity to work with you.

Thanks to all the students and professors in TELAC, especially Seth Kessler and Thad Matuszeski (for all your help in the lab), Catherine Sanders (for proof-reading my thesis), Chris Dunn (for all your help), Dennis Burianek (for keeping the Sun working), and Mike Toribio (for help with the writing).

A special thanks to all those who have helped with manufacturing and testing: John Mahoney, John Kane, Dick Perdichizzi, and Don Weiner. Also thanks to Picatinny Arsenal (Alex Plotkin and Don Babcock) and the Naval Sea Warfare Center in Dahlgren, VA.

And of course, thanks to my friends: Reid (Konich...we made it!), Margarita (Europe, here we come), Ernest (It's Friends and Fish time), and Terry (for the laughs and coffee). And special thanks to Bonnie, Carol, Elissa, and Margaret -- I can not say enough thanks for all you have done.

Last, but most importantly I want to thank my family for your support and encouragement. Mom and Dad, this is for you.

# Table of Contents

# List of Figures

# List of Tables

# CHAPTER 1

# INTRODUCTION

Composites have gained an increasing role in structural components of aerospace applications. Their high specific strength and stiffness have made them an attractive option for high performance structures. One particular application in which composites appear to offer significant advantages over metallic alloys, is that of unmanned aerial vehicles.

Unmanned Aerial Vehicles (UAVs) have recently begun to play a crucial role in military reconnaissance missions. With this initial success of UAVs, the demand for rapidly responding, inexpensive reconnaissance at all levels of command has also become greater. In an attempt to meet this growing demand, the military has recently begun investigating the use of smart projectiles and artillery launched vehicles. One such vehicle, the Wide Area Surveillance Projectile (WASP), has been developed in a joint effort between the Massachusetts Institute of Technology and Charles Stark Draper Laboratory [1-12].

In such artillery launched vehicles, the main considerations are the structural integrity and flight characteristics, which are often in conflict. At launch, the vehicle is exposed to high accelerations in excess of 12,000g's (117,720 $m/s^2$). The requirements for structural integrity and the need to rapidly produce a prototype led to a completely metallic design for the initial WASP demonstration vehicle. However, with an entirely metallic design, the vehicle is overly heavy and does not have stable flight characteristics. For this

reason, the use of composites in the design has been gaining increasing interest. Certain structural components have been considered for the introduction of composite materials. One such component is the wing system. A composite wing would decrease the weight of the wing and hence the overall vehicle weight, but would also allow the structure to maintain its bending and torsion stiffness for flight conditions. The wing is sized by the need to survive the high launch accelerations. Since the wing is stowed axially within the WASP fuselage, buckling is the critical failure mode, which sizes the wing cross-section.

Extensive previous research has been performed to classify the behavior of composites under axial compressive loads. For composite plates, both analytical and experimental studies have investigated and characterized the buckling response. However, the buckling response of composite plates and shells in a high-g, gun-launched environment has not been studied.

When designing these gun-launched vehicles, the main design tool is through experimental testing. Models have not yet been developed that can accurately predict the behavior of structural components in this high-g environment. Therefore, experimental testing must be used to verify all components of the design. The standard approach is to use a building block methodology. This involves the design and testing of individual components at increasing levels of complexity, until the design is validated for high-g survivability. This procedure is carried out until the entire vehicle design has been validated. However, the experimental component of this approach can become every expensive and time consuming to perform. Therefore, there is a need to understand the gun launch environment and to try to develop less expensive and more efficient design tools.

The objective of the current work is to investigate the use of composites

within the WASP wing system design by specifically studying the buckling behavior of curved composite panels under high-g loading. This objective is accomplished through the development of a finite element model and experimental testing. The finite element model is developed as a design tool to investigate the buckling behavior of the curved composite panels. The main area of interest is the ability of the model to accurately predict the critical buckling load and the deformed mode shape of the panels. The experimental phase investigates the response of the composite panels when subjected to controlled axial compression tests and air gun tests. The results of the finite element model, axial compression tests, and air gun tests are then compared. In this way, the finite element model and experimental tests are used to provide a better understanding of the buckling response of curved composite panels under high-g loading. In addition, the air gun test results are used to validate the finite element model and axial compression tests as design tools for structures subjected to the high-g environment of a gun launch.

The work performed for this research is presented in the following manner. An overview of the WASP Project is presented in Chapter 2. Then, in Chapter 3, a detailed design of the current WASP wing system is described. Relevant previous work relating to the buckling behavior of composite plates is reviewed in Chapter 4. In Chapter 5, the finite element modeling is discussed, particularly with regard to modeling the wing as a constant thickness curved panel and determining its critical buckling load. The experimental procedures, for both the controlled axial compression tests and the air gun tests, are outlined in Chapter 6. This is followed by a presentation of the results in Chapter 7. Then, in Chapter 8, the results are discussed in farther depth. Based on the results, conclusions are drawn and recommendations for future work are made in Chapter 9.

# CHAPTER 2

# WASP PROJECT

## 2.1 MIT/Draper Technology Development Partnership Project

The MIT/Draper Technology Development Partnership Project was a joint effort between the Massachusetts Institute of Technology Aeronautics and Astronautics Department and the Charles Stark Draper Laboratory from May 1996 through July 1998. The main goals of the partnership were to develop a first-of-a-kind system that would meet an important national need. The system was to be taken from a conceptual stage to a hardware/software demonstration within a two year time frame. Initially five main projects were considered and a down-select process led to the decision to pursue the Wide Area Surveillance Projectile (WASP). The Wide Area Surveillance Projectile is a gun-launched reconnaissance vehicle.

### 2.1.1 Program Objectives

The goal of the MIT/Draper Partnership was to give graduate students the opportunity to work within an industry group setting on a systems engineering design project. The objectives of the MIT/Draper Technology Development Partnership Project were:

- Develop a first-of-a-kind system
- Provide a solution to a national problem, opportunity, or need
- Involve "high-risk" technologies, termed "unobtanium"
- Use integrated, multi-discipline product development techniques

- Take advantage of MIT's and Draper's enabling technologies
- Be applicable to several markets and customer needs

2.1.2 Schedule (Two year plan)

The project was to span a two year time frame (Figures 2.1 & 2.2). During the first year of the program, the project was selected and preliminary design began. Initially, national needs and opportunity areas were identified. The four main opportunity areas that were identified were Innovative Projectile Systems, Intelligent Cooperative Systems, Advanced Aircraft Navigation and Control, and Inexpensive Space Systems. For each of these opportunity areas, innovative and challenging solutions were identified. This then lead to the selection of five major projects : Autonomous Search and Rescue System, Autonomous Vertical Takeoff and Landing Aircraft, Hybrid Launch System, Solar Sail Propulsion Demonstrator, and Wide Area Surveillance Projectile. Each of these projects was carried through a preliminary conceptual design phase. Then a down-select process based on a market assessment and MIT/Draper capabilities lead to the decision to pursue the Wide Area Surveillance Projectile. Once the specific project was chosen, conceptual design began. For further information see References [1-5]. The second year continued with the design process until detailed designs were completed. A prototype was then manufactured and tested to validate the design of the system.

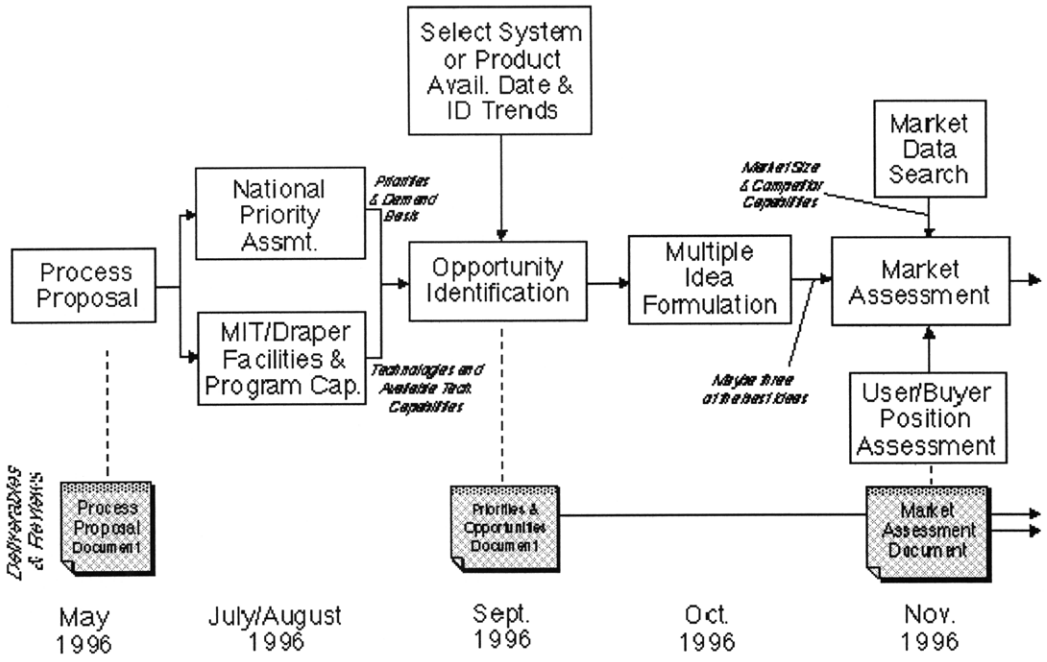


**Figure 2.1: Partnership Plan for May 1996 to November 1996**

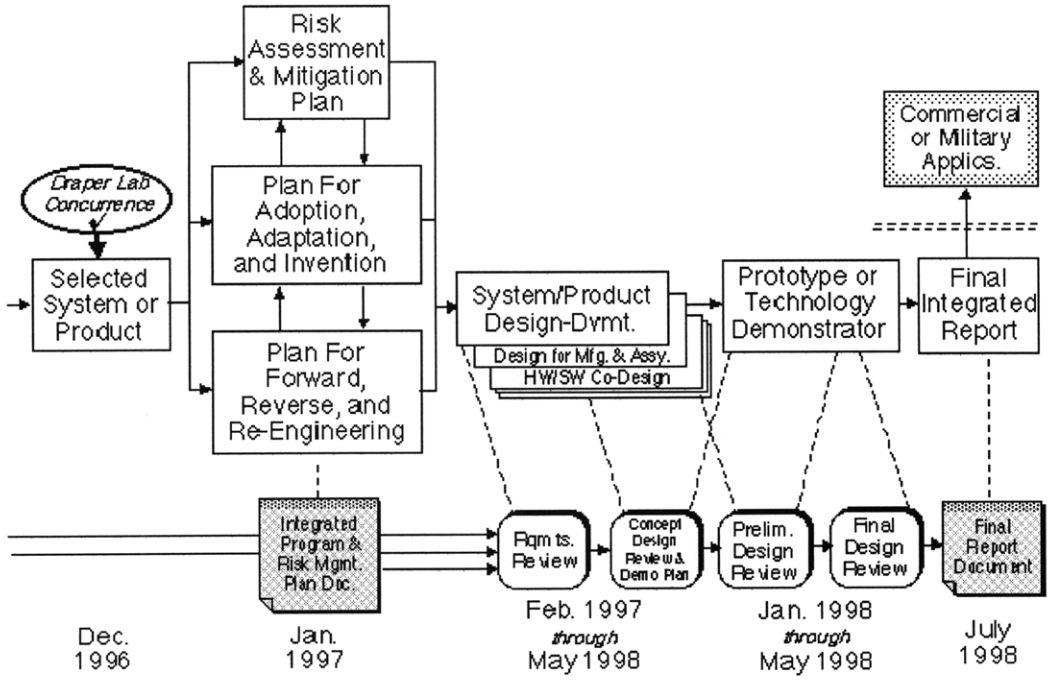


**Figure 2.2: Partnership Plan for December 1996 to July 1998**

## 2.2 Mission Overview

The Wide Area Surveillance Projectile (WASP) project is a gun-launched unmanned aerial vehicle. The mission objective is to provide fast response reconnaissance at a lower command level.

### 2.2.1 Market Assessment

On the battle field, the benefits of using reconnaissance vehicles to gain strategic and tactical information are widely appreciated. Currently several such vehicles exist to aid in military operations. The WASP system is designed to fill an existing hole in the available reconnaissance vehicles. At the top-most level, satellites are used for global reconnaissance. However, these can only view targeted areas at certain designated times and are controlled at a national level. The next level of reconnaissance vehicles consist of aircraft that perform high altitude and long endurance aerial reconnaissance. Again, these take time to reach a targeted area and the data is not readily accessible to battle groups. At the next level, there are Unmanned Aerial Vehicles (UAVs) which provide battlefield coverage. These must be dispatched to the area of interest and the data is not immediately accessible to the individual battle groups. The WASP system is designed to be used by individual tactical groups so that immediate unit-level reconnaissance information can be obtained. The system offers the benefits of fast response and a lower command chain, so that the information is immediately available to individual battle groups (Figure 2.3).

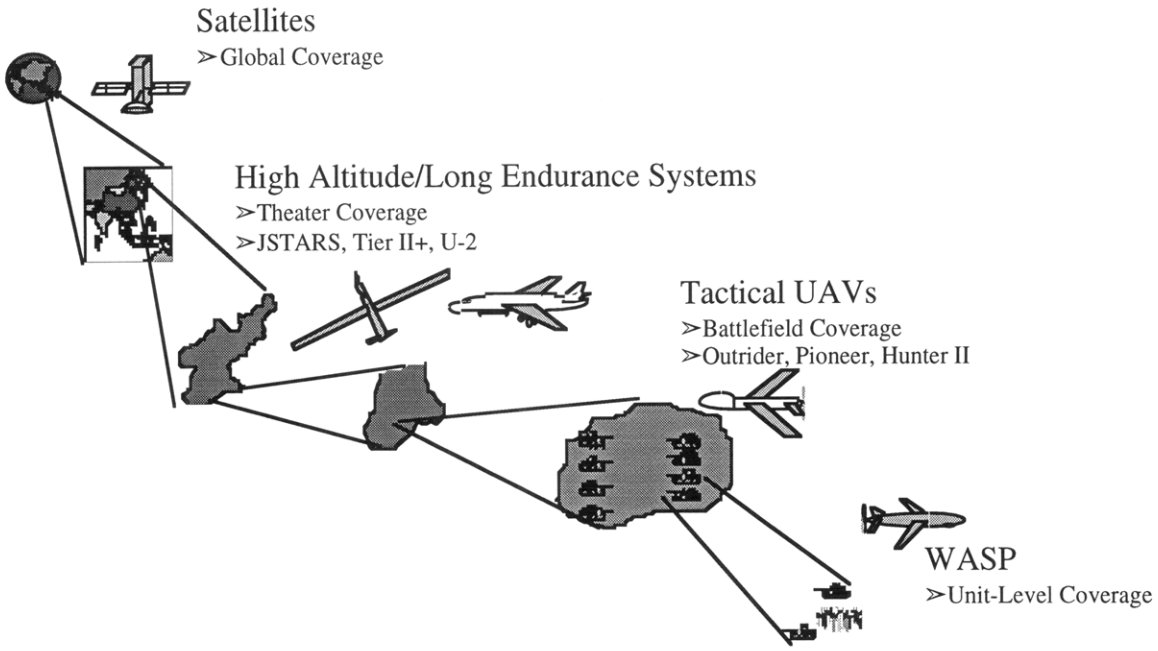


**Figure 2.3: Market Niche**

2.2.2 Mission Scenario

This system is designed to provide immediate reconnaissance information on a battlefield. An ideal situation to use this vehicle would be in parallel with an existing live artillery round. Two such scenarios in which WASP could be used are for targeting or damage assessment (Figure 2.4). The vehicle could be used initially to scout out the battlefield and identify the position of targets of interest prior to using a live round. Or in the reverse situation, the WASP vehicle could be deployed after a live round was used in order to view the battlefield and confirm whether a target was successfully engaged.

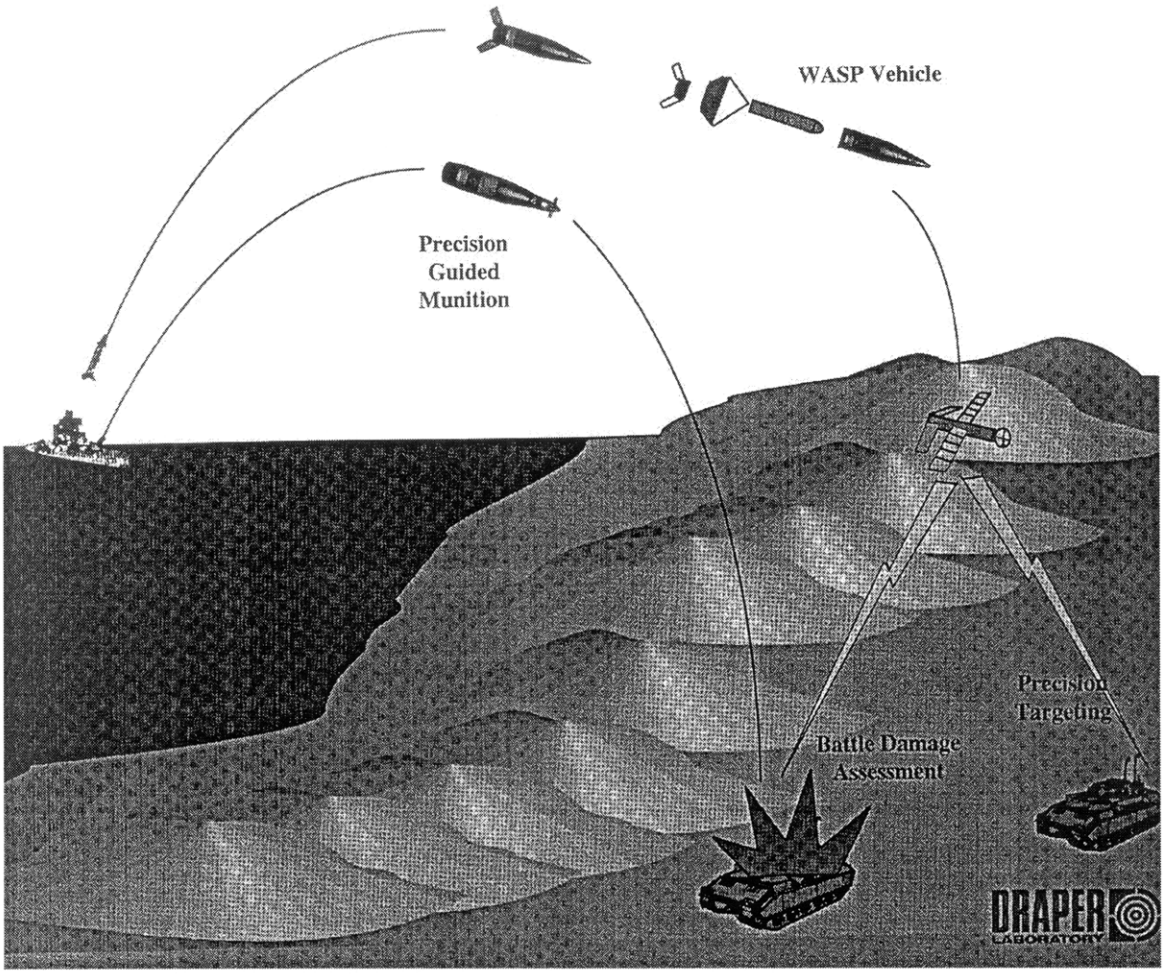


**Figure 2.4: Mission Scenario**

2.2.3 Mission Profile

The overall mission profile is shown in Figure 2.5. The system is launched from a 5-Inch Navy gun. After exiting the gun barrel, tail fins are deployed to stabilize the system during its ballistic trajectory. Once over the targeted area, the back-end of the shell separates and the parachute system is activated. The parachute's dual purpose is to extract the flyer from the shell and aid in its deceleration. As soon as the flyer is extracted from the shell, the tail fins are deployed to help stabilize and decelerate the system. The propeller is then deployed, and with the aid of a spring mechanism, the engine is started. Once the system has been decelerated, the folding wings are deployed. After all of the components are deployed, the parachute is released and the flyer performs a pull-up maneuver. It then carries out its reconnaissance mission.

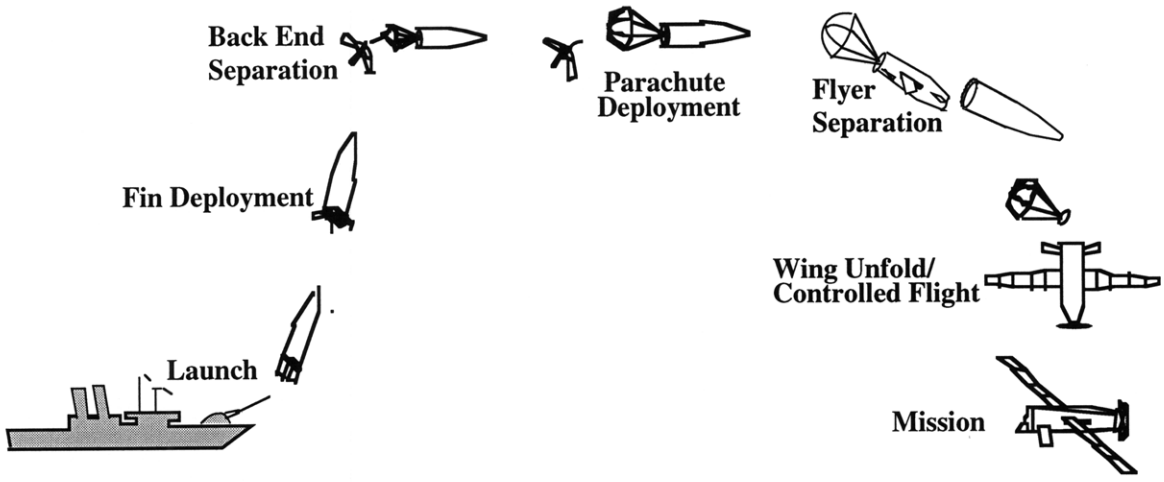


**Figure 2.5: WASP Mission Profile Schematic**

2.2.4 System Requirements

In order to fit within the described market niche and perform a successful reconnaissance mission, a set of system level requirements were developed. Initial requirements were determined after consulting with Draper

Laboratory personnel and Army and Navy officials. After studying the system in greater depth, the requirements were modified to better represent a realistic system. The final set of top level system requirements are:

- Compatible with 5-Inch Navy Gun
- Survive a 15,000g acceleration
- Loiter for 15 minutes
- Be autonomous and carry a camera
- Inexpensive and storable
- Ground station to receive real-time images and GPS coordinates of targets

### 2.2.5 Concept Demonstration

The WASP project generated a paper design of the entire system. The vehicle faces two main design challenges: high-g survivability and flight characteristics. In order to investigate each of these challenges separately, two test vehicles were used. The first of these vehicles, High-G Vehicle (HGV), is used to demonstrate the high-g survivability of the structural and mechanical components of the operational vehicle. The second vehicle, Flight Test Vehicle (FTV), demonstrates the flight characteristics and aerodynamic performance of the operational vehicle.

## 2.3 WASP High-G Vehicle Design

The WASP High-G System consists of two main components, the shell support and deployment system and the flyer. The main purpose of the shell support and deployment system is to safely deliver the flyer to the targeted area and initialize the deployment sequence. The main goal of the flyer is to successfully collect reconnaissance information.

2.3.1 Shell Support and Deployment System

The shell support and deployment system that is currently used in the design consists of a modified 5-Inch Navy Illumination Round, nose cone, attachment clamps, and an integrated shell base that contains the stabilizing tail fins and parachute system (Figure 2.6).

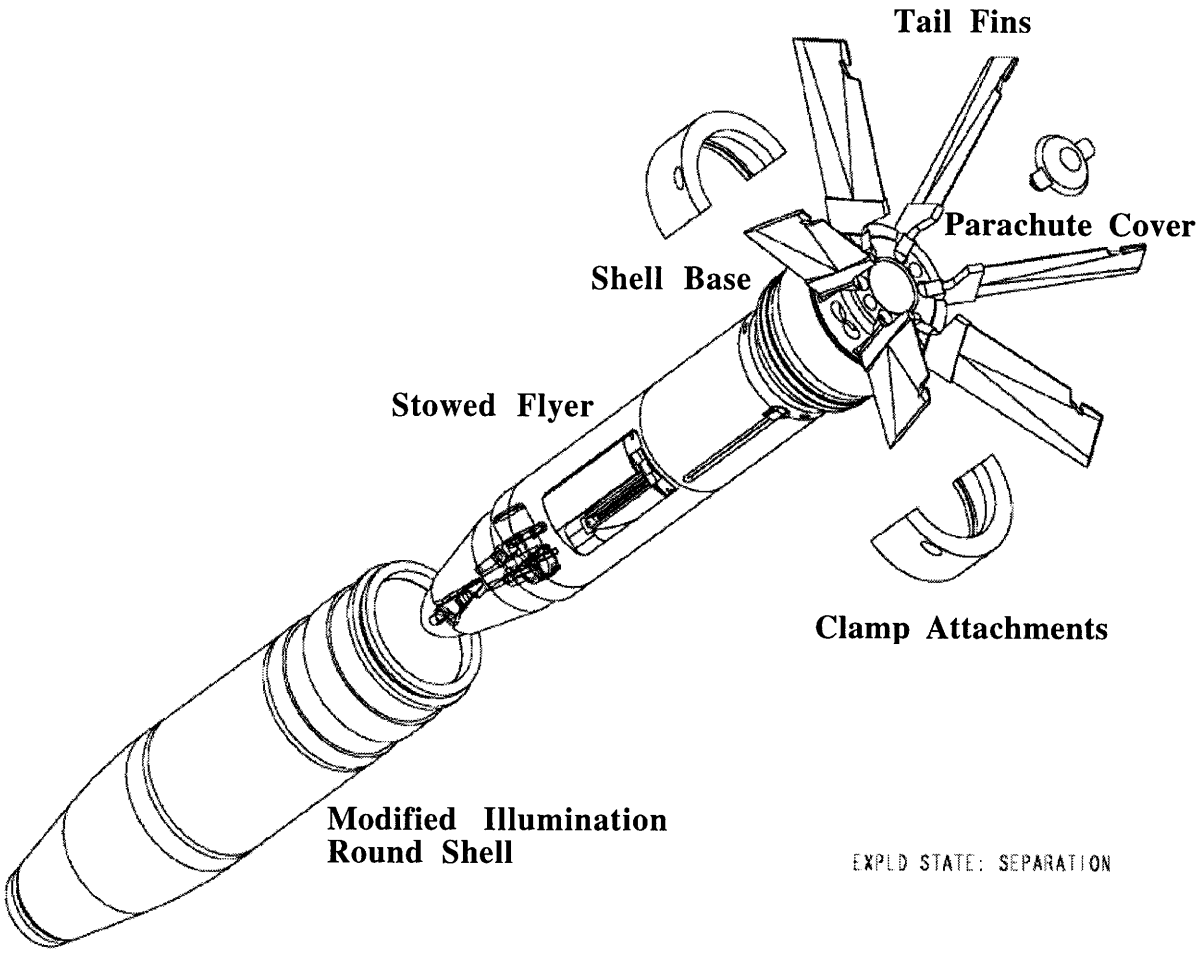


**Figure 2.6: Shell Support and Deployment System**

The purpose of the shell support system is to guarantee the safe delivery of the flyer to the targeted area. During the launch environment, the shell supports the flyer and protects it from the propellant gases. During the

ballistic trajectory of its flight, the shell also protects the flyer, and the tail fins ensure that the system remains stable. At the back end of the shell, there is a shape charge that entirely surrounds the shell. Once over the targeted area, this charge is activated and separates the back-end of the shell. Two pin thrusters are then used to release the parachute. The parachute is attached to the flyer through an explosive bolt. The parachute system is designed to apply a force to the flyer that is adequate to pull it out of the shell and then to decelerate it to the desired cruise speed. For more details on the shell support and deployment system refer to Reference [6]

2.3.2 Flyer

The flyer itself is divided up into three main sections: the forward propulsive module, the mid wing module, and the aft tail module (Figure 2.7). Dividing the flyer into three sections aids in the design and manufacturing of the system. The design leads to a very modular system that is integrated during the final stages of assembly.

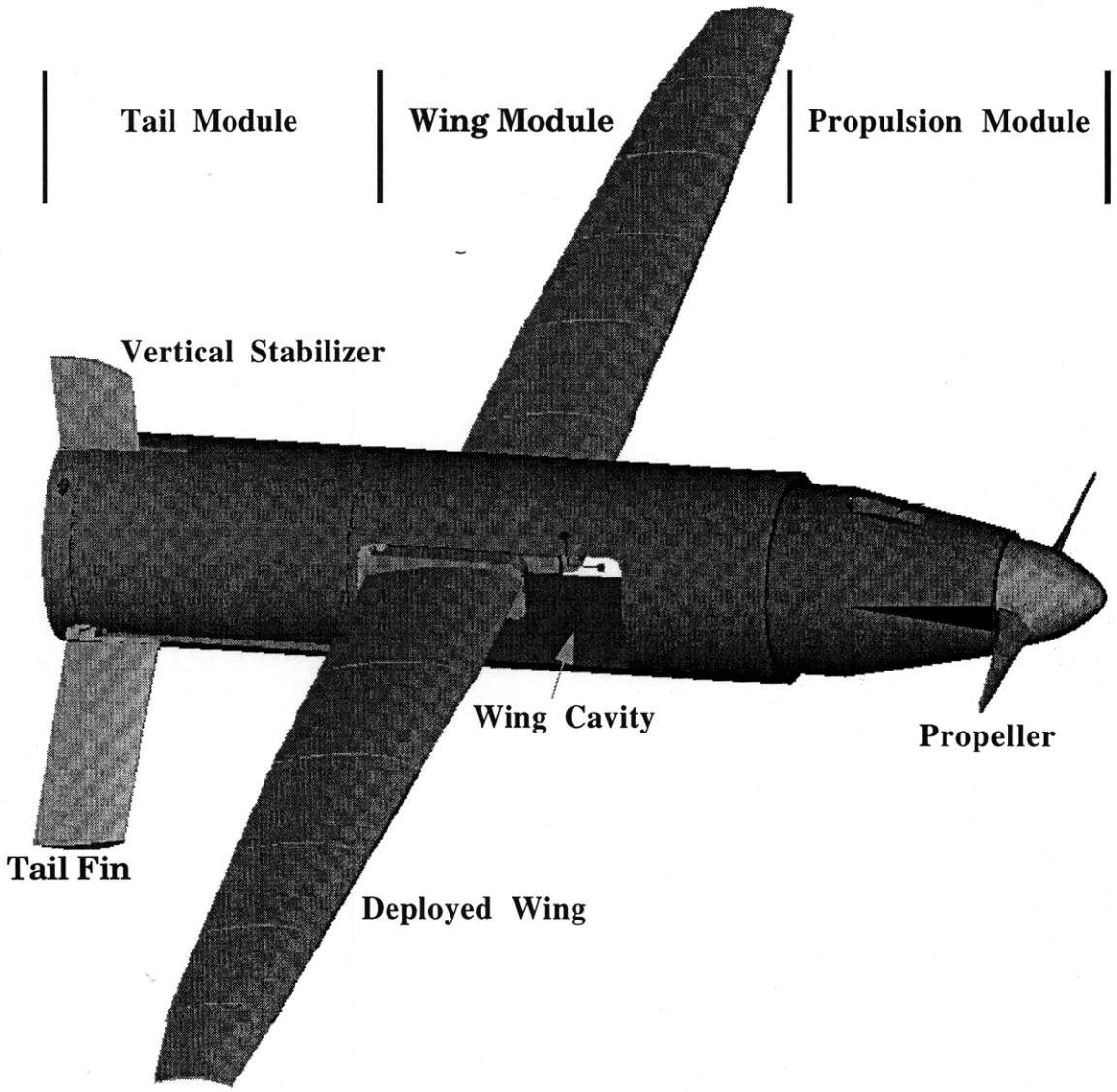


**Figure 2.7: Schematic Diagram of the WASP Flyer**

#### 2.3.2.1 Propulsive Module

The propulsive module consists of the nose cone, engine, throttle servo mechanism, propeller, and spring start mechanism. The design currently uses a 2 stroke engine produced commercially for radio-controlled model aircraft. The nose cone serves as the casing for the engine. The engine provides approximately 300 Watts of mechanical power to the system allowing the flyer to cruise at approximately 90 miles per hour. The propeller is initially folded back along the nose cone and is spring loaded so that as soon as the flyer is extracted from the shell, the propeller deploys. To aid in the starting of the engine, a spring start mechanism is used. The spring start mechanism is a coiled spring that produces sufficient torque to start the engine. The servo controls the throttle setting of the engine to obtain maximum performance.

#### 2.3.2.2 Wing Module

The center section of the fuselage is the wing module which contains the folded wing system, battery packs and fuel tank. The batteries are packaged in wax around the fuel tank structure at the front end of the wing module. The fuel tank holds enough fuel to allow for approximately 15 minutes of flight time. The main components of the mid section are the folding wings and their support structure for launch conditions.

#### 2.3.2.3 Tail Module

The tail module includes the tail fins, servo mechanisms, and place holders for the onboard electronics. The tail fin design is a V-tail configuration. The tail fins are spring loaded such that as soon as the flyer clears the shell, the tail fins are deployed. The servo mechanisms allow 7 degrees of rotation for the tail fins so that the flyer can be controlled. Also within the tail module, there are compartments for the onboard electronics that are being developed at Draper as part of the Competent Munition Advanced Technology

Demonstration (CMATD) project. For more details refer to Reference [7].

## 2.4 Experimental Testing for High-G Vehicle

Experimental testing was carried out to validate the design of the WASP High-G Vehicle. The testing was used to validate the individual component designs as well as the whole integrated system.

### 2.4.1 Air Gun Tests

Air Gun Tests were performed at Picatinny Army Arsenal in Dover, NJ. Air gun tests are used to simulate the accelerations that occur during launch. The same magnitude of acceleration can be achieved using an air gun as would be imparted to a projectile in an actual 5-inch gun. The main difference between the two acceleration profiles is the time taken to reach peak acceleration. In an air gun test, the peak acceleration is achieved in approximately 1 millisecond, whereas a 5-inch gun takes approximately 3 milliseconds to reach peak acceleration. However, the air gun test has been found to accurately predict the survivability of components under high-g loading at a much lower cost than an actual gun firing.

An air gun uses compressed air to accelerate a canister down a chamber. The canister that is used to test the components has an inner diameter of 3.9 inches and a height of 9.315 inches. Due to these size constraints, the whole WASP High-G Vehicle could not be tested using this method. However, the air gun tests were very instrumental in aiding and validating the design of the individual modules and their components.

### 2.4.2 Canister Test

The final test that was carried out to validate the entire design of the WASP High-G Vehicle was an 8-inch canister test at the Naval Sea Warfare

Center in Dahlgren, Virginia. This test uses an 8-inch Navy gun to launch a retrievable test canister. The desired g-loading level can be obtained by varying the amount of propellant charge that is used for the launch. The acceleration profile for the 8-inch round is relatively close to a 5-inch round. The main difference is that in the test scenario, the test article itself is enclosed in a canister so it is not exposed to the gases and pressures produced by the combustion process during launch. However, components that survive the 8-inch test are expected to survive the 5-inch gun launch.

The test canister that is used has a length of 22 inches and thus the entire WASP vehicle, without the tail fin system, fits within the canister. In order to mount the test article in the canister, the base of the shell was modified and a mounting support was added to the nose of the shell. The complete test article for the 8-inch canister test can be seen in Figure 2.8.

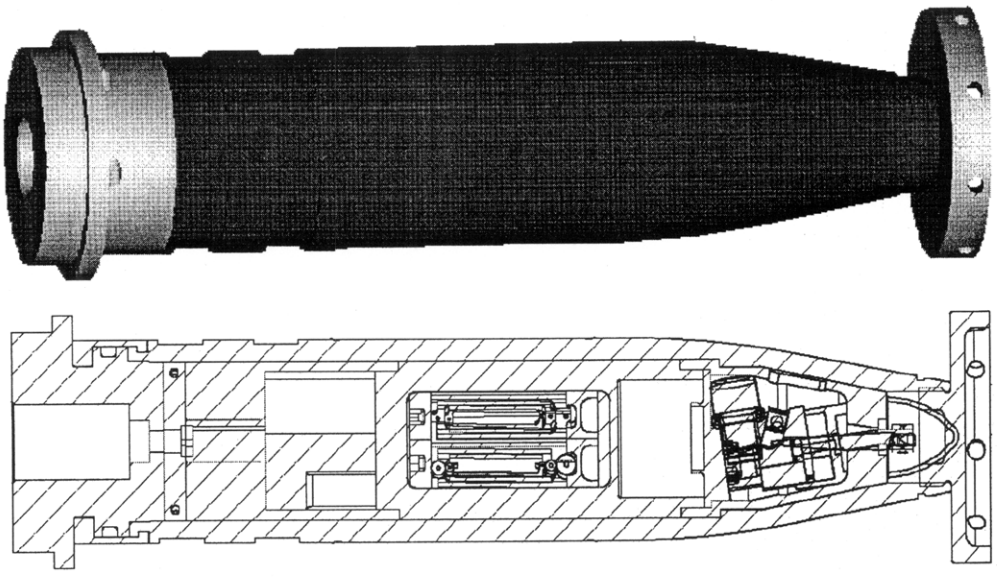

**Figure 2.8: Test Article for 8-Inch Canister Test**

On March 14, 1998 the canister test was performed. The acceleration recorded during launch was 12,026 g's and the canister reached an altitude of 7,700 feet. The test canister along with the 8-inch gun can be seen in the following picture.

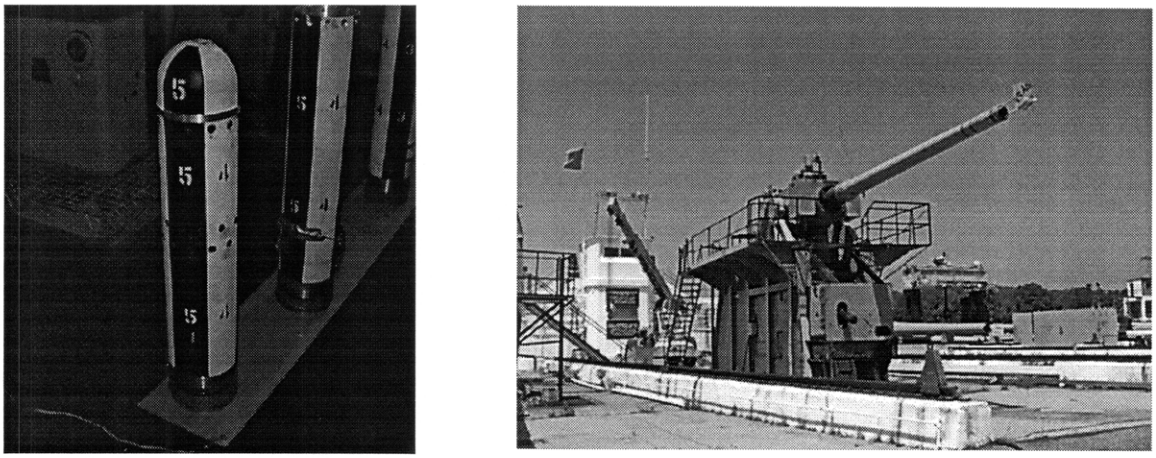

**Figure 2.9: 8-Inch Canister and Gun**

After the retrieval of the test canister, the canister was disassembled and the WASP High-G Vehicle was inspected. The vehicle was easily removed from the test canister and there was no physical damage to the outer shell and base of the vehicle. The deployment sequence of the vehicle was then carried out manually. The flyer slid out of the shell with no problem indicated that none of the structural components had jammed. The tail fins immediately deployed once they cleared the shell. The wing support blocks were then manually removed and the wings deployed successfully. Also there was no physical damage to the engine module. The entire system survived the 8-inch canister launch with no signs of damage, thus validating the high-g design of the WASP system.

## 2.5 Flight Test Vehicle Design

The Flight Test Vehicle is a scaled up model that is used to verify the flight characteristics of the operational vehicle (Figure 2.10). The vehicle uses off-the-shelf electronics and therefore its design was based on the size requirements of these elements. The vehicle's configuration is similar to the High-G Vehicle except that it is scaled by a factor of 1.28.

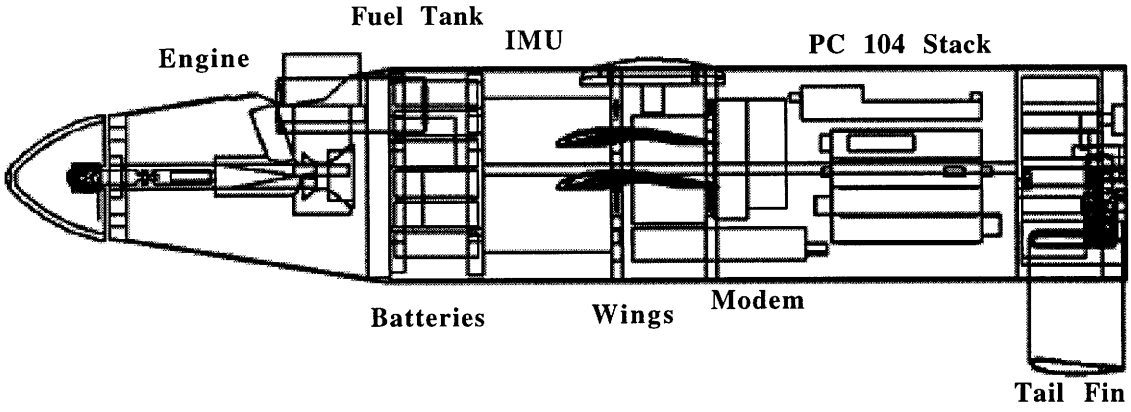


**Figure 2.10: Flight Test Vehicle Cross Section**

### 2.5.1 Structural Components

The FTV, a model of the operational vehicle, is not designed for high-g survivability. Therefore, it is constructed of readily available materials such as sheet metal, aluminum, and Plexiglas. The nose cone is rolled aluminum sheet metal and contains the engine. The body is constructed from an aluminum tube. There is a Plexiglas mount, upon which the engine rests, which serves to join the nose cone to the main body of the flyer. There is an electronic insert that contains all of the electronic components. The wings are simplified by manufacturing them as single piece carbon fiber composite

structures as opposed to the segmented hinged configuration to be used in the operational vehicle. The tail end of the flyer consists of a stereolithography component that represents a similar tail fin configuration as used in the HGV.

2.5.2 Propulsive System

The propulsive system of the FTV is also scaled up to support the increased size and weight of the vehicle. The system contains a larger engine than the HGV vehicle in order to provide extra power to the system.

2.5.3 Electronics

The FTV contains all of the electronic components that are necessary for autonomous flight. The electronic components are off-the-shelf hardware. The vehicle is sized specifically to incorporate all of the necessary electronics. The components along with their placement within the vehicle can be seen in the above picture of the FTV. For more information on the FTV electronics refer to References [8 & 9].

## 2.6 Experimental Testing for the Flight Test Vehicle

The Flight Test Vehicle went through a series of drop tests at an Army Testing Ground in Sudbury, Massachusetts (See Figure 2.11). The drop test used a remote controlled ultra-light to take the vehicle up to the appropriate altitude and cruise speed. The vehicle was strapped onto a test mount under the body of the ultra-light. The vehicle was then remotely released. Once the system was dropped, it was then controlled from the ground through a radio controlled link. Then when the system approached the ground, a parachute system was deployed to ensure that the system was not damaged when it impacted the ground on landing.

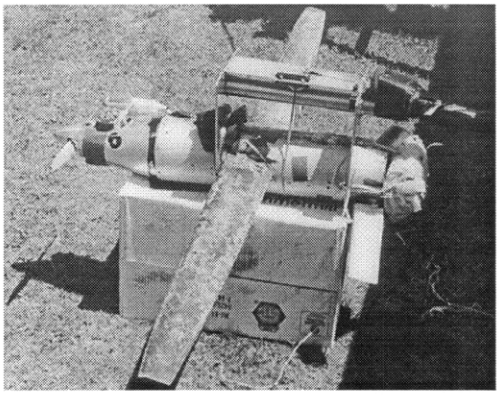

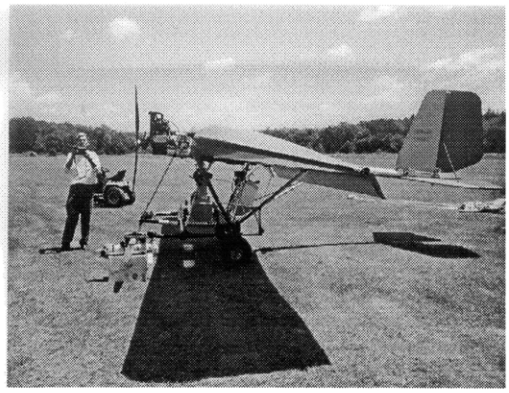

**Figure 2.11: Flight Test Vehicle and Ultra-Light**

The Flight Test Vehicle was not as successful as the high-g vehicle. The vehicle never demonstrated stable flight. Three theories were proposed as to why the system was not behaving as the simulation predicted. The first concern was the way the system was released from the mount on the ultra-light. The orientation of the flyer could have caused the vehicle to immediately go into a stall mode which would characterize the unstable behavior. Second, the vehicle was also being deployed from the ultra-light at a speed significantly below the vehicle's intended cruise speed. Third, the vehicle was believed to be too heavy and to have insufficient control surface authority.

## 2.7 Summary

This chapter presented an overview of the Wide Area Surveillance Projectile. The two main design concerns for the vehicle were its high-g survivability and flight characteristics. Through experimental testing each of these key concerns were addressed. The High-G Vehicle demonstrated the structural survivability of the WASP design. One key component of the design, which will be discussed in the following chapter, is the wing module. However, the Flight Test Vehicle was too heavy and not able to demonstrate stable

flight. This issue will later be addressed by investigating the use of composites within the WASP design.

# CHAPTER 3

# WING MODULE DESIGN

This chapter details the current design of the WASP vehicle's wing module. The key aspects of the wing and its support system are described in detail. Also, the progression of the design together with an integrated test program is described. A presentation of the wing module design can also be found in Reference [10].

## 3.1 Wing Requirements

The requirements for the wing are set by both the launch and flight conditions of the vehicle. The main requirements for the wing system of the WASP vehicle are:

- Survive 15,000g acceleration (Set back)
- Survive 4,000g acceleration (Set forward)
- Stored within a packaging volume of 643.5 cubic centimeters
    - 13cm x 5.5cm x 9cm
- Support vehicle weight of 8 kilograms in flight
- Deployment speed of 200 miles per hour
- Cruise speed of 90 miles per hour

## 3.2 Wing Concepts

Initially three wing concepts were investigated for the WASP vehicle. The main considerations in choosing the type of wing that would be a part of the vehicle were size, weight, complexity, cost, and ability to produce a prototype within a one

year period. The three choices for the wing system included a telescopic wing design, an inflatable wing design, and a folding wing design.

### 3.2.1 Telescopic Wing

The idea for a telescopic wing originated from aerospace applications where large structures are sometimes stored in a small compact configuration. The wing would have two spars that would telescope out with a flexible skin surface over top of the spars. This idea offers the benefit of allowing the wing to be small and compact for storage while in the launch configuration. However, the design also requires many moving parts for deployment which was ultimately deemed to be a high risk. For this reason, it was decided to look at other options.

### 3.2.2 Inflatable Wing

Another option for a deployable wing is an inflatable wing. This concept is currently being pursued by other companies that are designing similar gun launched systems. Primex Aerospace is currently heading-up the design of this wing [13]. The idea behind this concept is to use compressed air to fill an airfoil. However after investigating this option in further depth, the cost of developing such a wing was extremely high.

### 3.2.3 Folding Wing

The final concept that was investigated and chosen is the folding wing design. The idea for this type of wing system came from previous work in which a folding wing with two sections was investigated [14]. This folding wing concept uses gravity to initiate the unfolding process of the wing segments. Then the momentum of the unfolding wing, along with the lift generated by the wing, aids in continuing the unfolding process and holding the wing in a locked configuration during flight.

This design offers the benefits of being compact, having few mechanical moving parts, and being inexpensive relative to the other options.

## 3.3 Wing Design

The current wing design for the WASP vehicle is a six section folding wing (See Figure 3.1). The wing was manufactured out of aluminum 7075. The key dimensions of the wing are a total span of 40 inches, a root chord of 3 inches, a tip chord of 1.5 inches, and an aspect ratio of 17. The system uses a spring loaded pivot and hinge system for deployment.

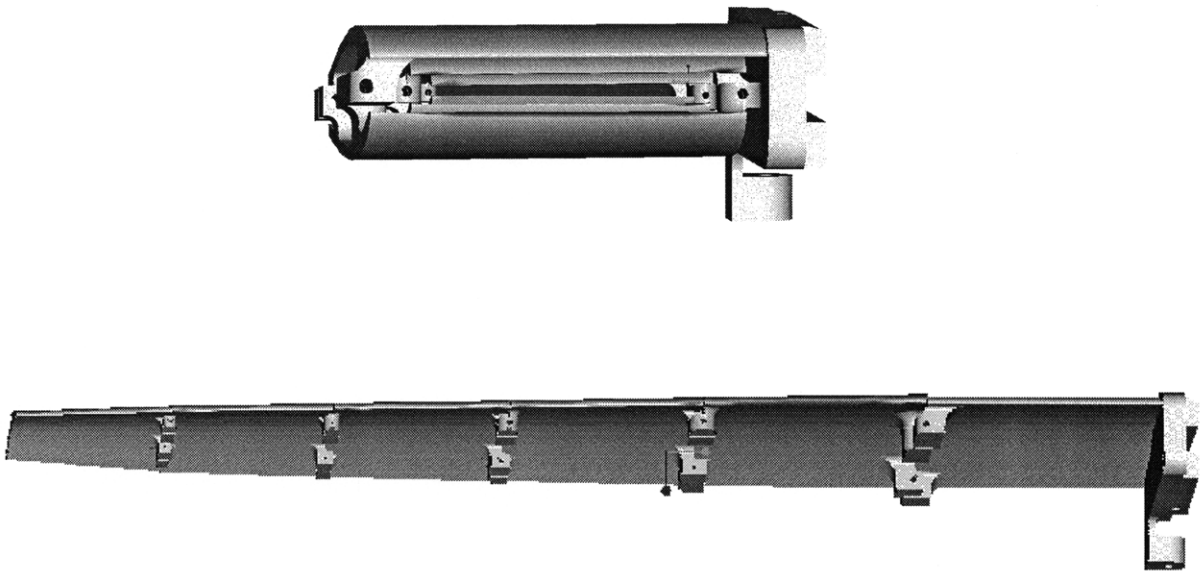

**Figure 3.1: Stowed and Deployed Wing**

### 3.3.1 Stacking Sequence

The wing design is based on a T16 wing profile. The stacking sequence was determined using Airset, a program developed at MIT [14]. With this program, a stacking sequence based on the volume constraints could be determined. By scaling

the wing profile, it was determined that six wing sections could be stacked successfully. The following figure shows a portion of the stacking sequence profile.

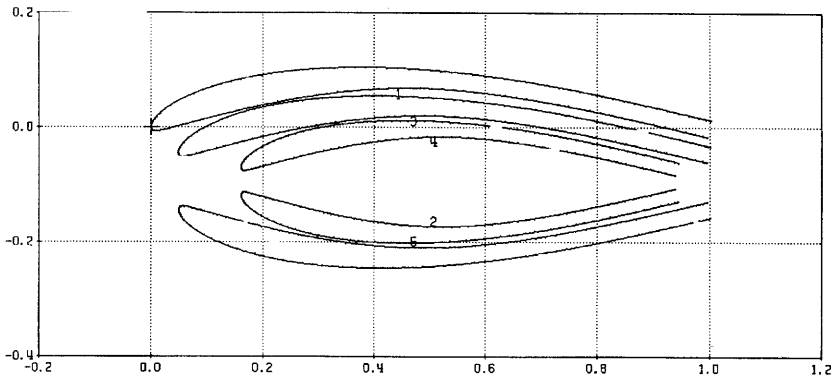


**Figure 3.2: Stacking Sequence**

From the stacking sequence, the root and tip chord of the wing segment was determined. A CAD package, Pro-Engineer™, was used to model and determine the length of the individual segments. Table 3.1 summarizes the dimensions of each wing segment.

| Wing Segment | Root Chord (in) | Tip Chord (in) | Span (in) |
|---|---|---|---|
| 1 | 3.00 | 3.00 | 3.40 |
| 2 | 3.00 | 2.83 | 3.25 |
| 3 | 2.83 | 2.57 | 2.85 |
| 4 | 2.57 | 2.33 | 2.57 |
| 5 | 2.33 | 2.09 | 2.36 |
| 6 | 2.09 | 1.52 | 1.67 |

**Table 3.1: Summary of Wing Dimensions**

3.3.2 Structural Considerations

The main structural loads that size the wing cross-section occur at launch. In designing the structure to ensure that the wing survives both the set back and set forward loads that occur during launch, two main areas of concern were identified. The locations where the wing is most likely to fail are at the pivot point and at the hinges. The design approach was used to isolate each of these key locations.

**3.3.2.1 Pivot Design**

The wing is designed to make an initial 90 degree pivot out of the flyer (See Figure 3.3). This 90 degree pivot is required to store the wings in such a way that would ensure survival during the launch. During the launch, the wing segments, which are basically curved panels, must withstand the load due to the 15,000g acceleration. The pivot is a spring loaded system that rotates the whole wing structure out of the flyer. The pivot and wing system is designed to allow for the maximum wing length in the given constrained volume.

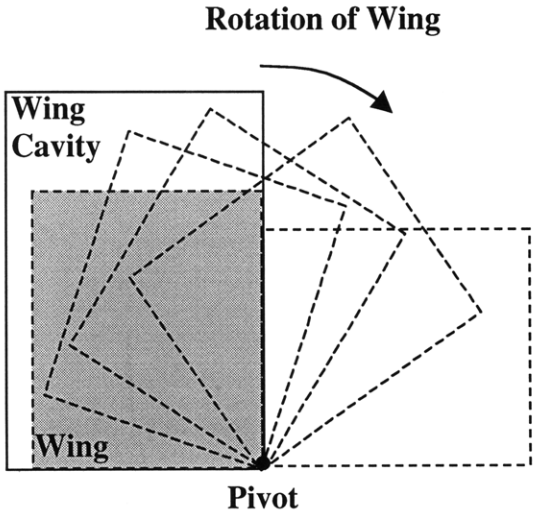


**Figure 3.3: 90 Degree Pivot Sequence of Wing**

The pivot system design is shown below in Figure 3.4. The pivot system consists of a base plate and a wing arm that supports the wing segments. The pivot mechanism joins the base plate to the wing arm. A torsion spring is used to provide the necessary torque to rotate the wing arm and wing segments out of the flyer.

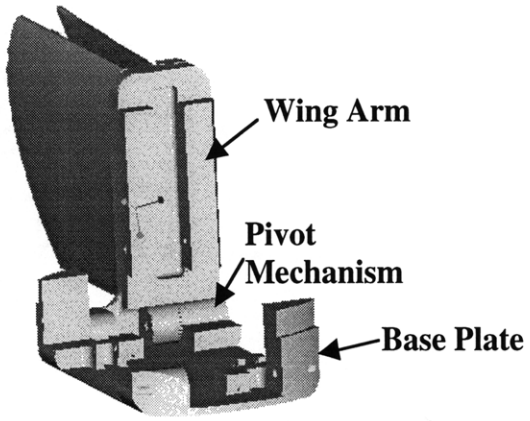


**Figure 3.4: Pivot Design**

#### 3.2.2.2 Hinge Design

The hinge is the second key aspect of the wing design. The hinges are designed so that the wings can be deployed using springs. The size of the hinges is governed by the volume that is available with the given stacking sequence. Each wing has two hinge segments. The hinge mechanisms are on the bottom side of the wing to reduce their effect on the aerodynamic performance of the wing. Between the hinge mechanisms, there is a torsion spring that is used for deploying the wing and holding it in a secure flight configuration. The following figure shows the hinge mechanism (Figure 3.5).

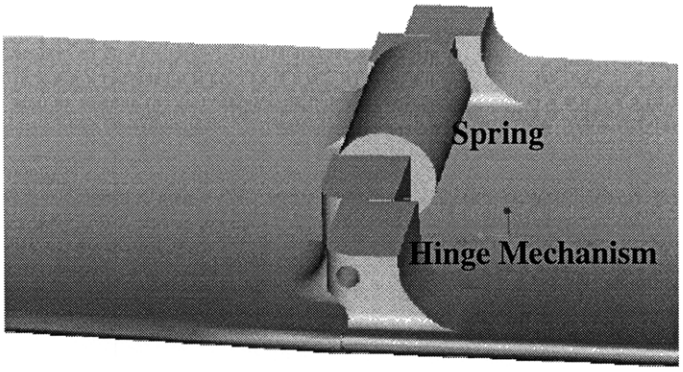


**Figure 3.5 Hinge Design**

The crucial part in the hinge design is to ensure that the hinges are adequately supported so that the load can be transferred to the support plates and the hinge itself is not carrying the majority of the load. This is achieved by assuring that the first hinge rests against the support blocks of the wing module and the second hinge rests against the base plate of the wing arm. The additional inner hinges are then designed so that they rest tightly against the outer hinges. The design is shown in Figure 3.6.

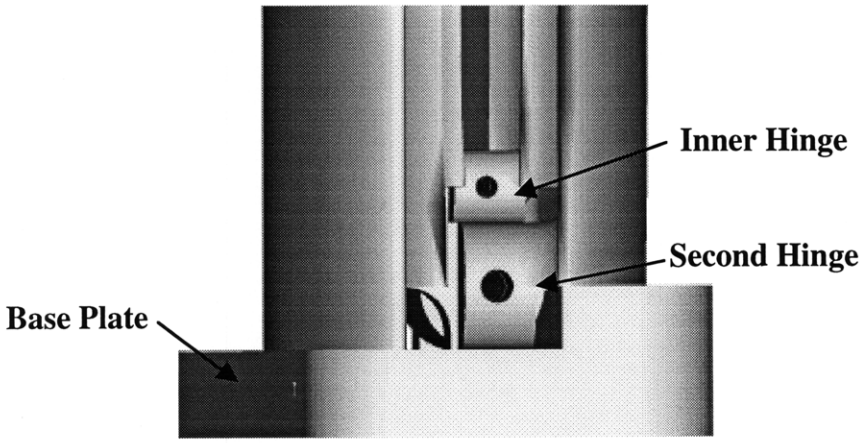


**Figure 3.6: Stacking Design of Hinges**

## 3.4 Wing Module Design

The wing module is designed to support the wing system both during launch and flight conditions. In addition to the wing itself, the key components of the wing module design are the support blocks for the set forward condition and the side covers for aerodynamic performance (See Figure 3.7).

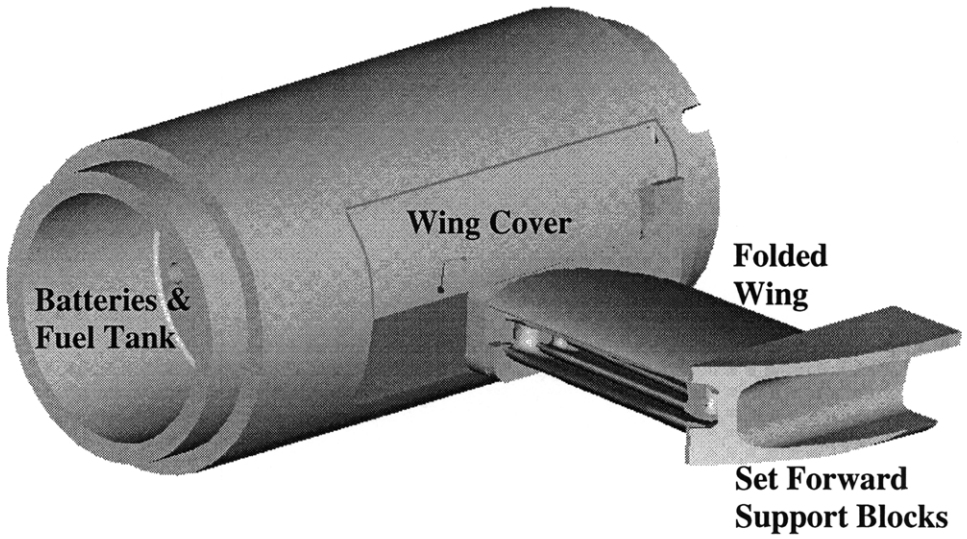


**Figure 3.7: Wing Module**

### 3.4.1 Set Forward Support Blocks

The support system for the wing system is crucial due to the large accelerations that are experienced during launch. The support blocks in the wing module are a necessary part of the design in order for the wing to survive the 4,000g set forward acceleration (See Figure 3.8). The wing module allows the load that is experienced during the set forward condition to be transferred to the support blocks so that the wing and hinges themselves do not have to support the entire load. The

support blocks are also designed to allow a smooth deployment. The blocks have an arc that is equivalent to the wing's pivot arc. This allows the wing with the support block to easily perform the initial 90 degree pivot out of the flyer. Once the wing has cleared the flyer, the support block will then fall away and allow the wing to continue its deployment.

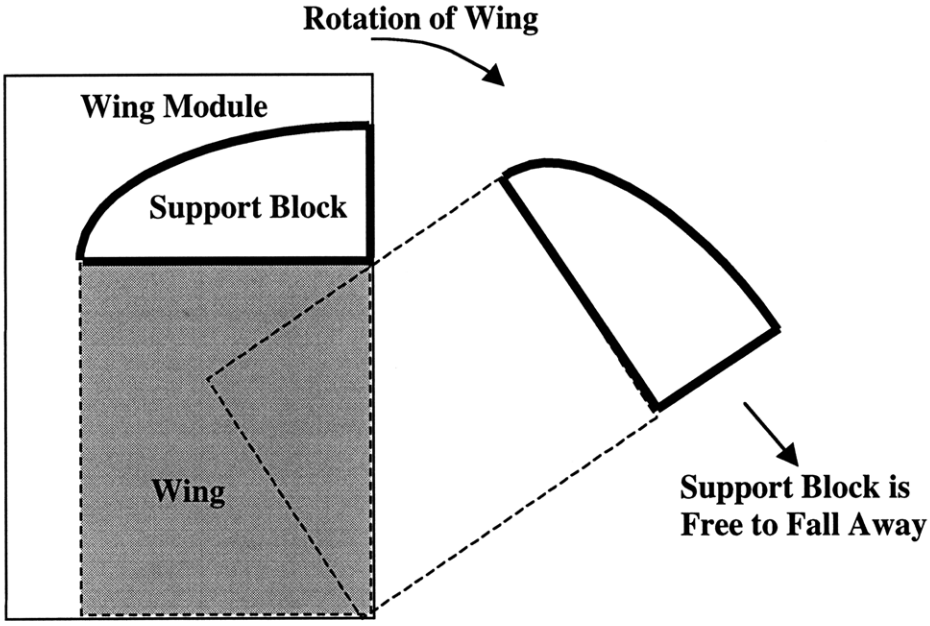


**Figure 3.8: Schematic of Support Block**

3.4.2 Wing Module Covers

The side wing module covers are included in the design in order to increase the aerodynamic performance of the flyer. The entire wing module cavity needs to be open for the assembly of the wings. However, once the wings are integrated into the wing module, only a portion of the wing module cavity needs to be open for the deployment of the wings. Since the opening in the wing module cavity increases the drag of the flyer, a plate was designed to cover the portion of the opening that is not needed for deploying the wings.

## 3.5 Experimental Tests

A series of air gun tests at Picatinny Arsenal were used to validate the design of the wing system. The testing phase followed the same progression as the design. The key elements were isolated and tested in phases, such that the pivot design was first verified and then the hinge design was verified. At the end, a final test was performed with the entire wing module. Once all of the key elements had been validated through air gun testing, a final 8-inch canister test was performed to validate the entire system.

### 3.5.1 Pivot Test

The first series of air gun tests were used to validate the design of the pivot, a device that is initially used to pivot the wing 90 degrees out of the flyer. The pivot test consisted of having the design of the wing arm and pivot deployment system (Figure 3.9). A small section of an airfoil was attached to the wing arm. A block representing the mass of the other wing sections was placed at the end of the airfoil.

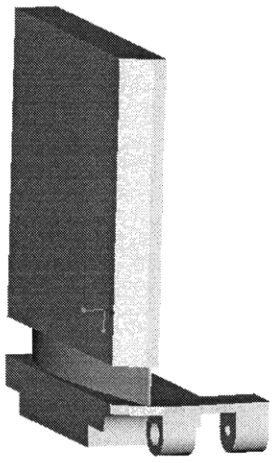

**Figure 3.9: Schematic of Pivot Test Article**

From the experimental test, the design of the pivot was verified for the 15,000g loading condition. However, the wing itself did not survive. The trailing edge of the wing section was too thin and thus buckled under the weight of the block. The test article along with a summary of the air gun test results can be seen below (Figure 3.10).

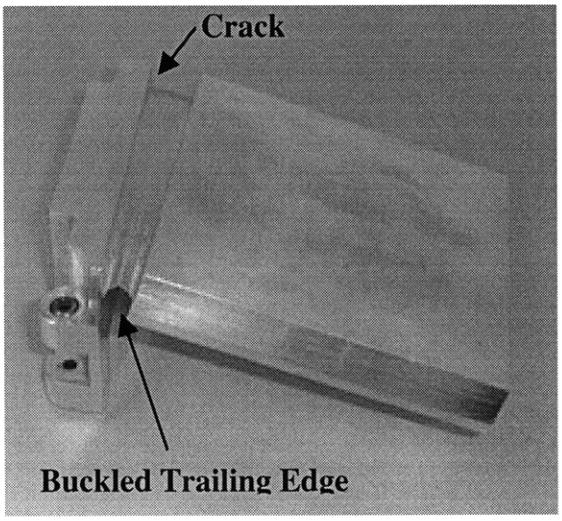


| Test | G Load | Results |
|---|---|---|
| 1 | 1400 | No Damage |
| 2 | 4962 | Wing Slightly Bent |
| 3 | 15100 | Wing Buckled |

**Figure 3.10: Pivot Test Article and Results**

The results of the pivot test led to a redesign of the wing's trailing edge thickness. The original thickness of the trailing edge was 0.3 millimeters. After performing a structural analysis for the buckling conditions under 15,000g and investigating the thickness for the deployment condition, it was shown that the

trailing edge thickness should be increased by a factor of 8 [10]. This redesign then led to a wing with a trailing edge thickness of 2.3 millimeters

3.5.2 Hinge Test

The second set of tests that were performed verified the design of the hinge (Figure 3.11). The test consisted of the entire first wing section which included the wing arm, the pivot deployment system, the redesigned wing and the first hinge. The second section consisted of a small portion of a wing with hinges and a block to simulate the mass of the remaining wing sections.

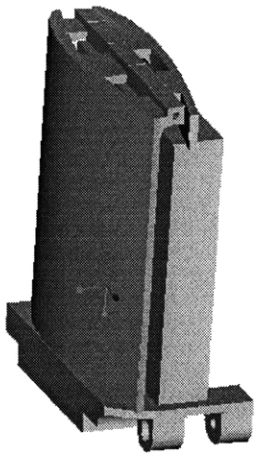

**Figure 3.11: Schematic of Hinge Test Article**

The test showed that the redesign of the wing panel was successful. Also the tests showed that support is a crucial aspect of the design. In three of the tests, a block was used to support the second section of the test article and there was no damage to the structure. However, when the support block was removed, the hinge failed. This knowledge then fed into the design of the final wing. The test article along with the air gun results follow (Figure 3.12).

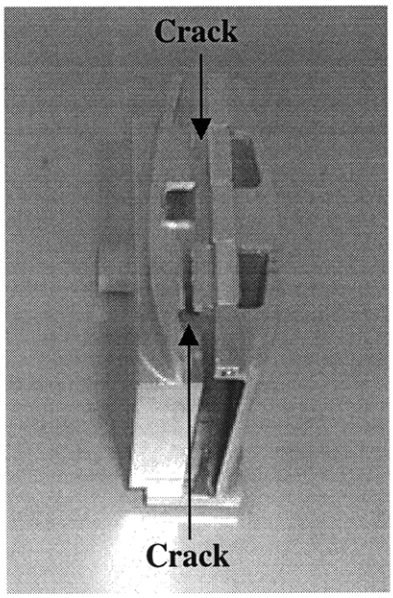


| Test | Support | G Load | Results |
|---|---|---|---|
| 1 | Yes | 6000 | No Damage |
| 2 | Yes | 12313 | No Damage |
| 3 | Yes | 14270 | No Damage |
| 4 | No | 11302 | Hinge Failed |

**Figure 3.12: Pivot Test Article and Results**

3.5.3 Wing Module Test

The final series of air gun tests studied the entire wing configuration under both the set back and set forward loading conditions. The test consisted of the entire wing structure and the packaging of it within the wing module.

The entire wing system survived the set back and set forward conditions. The wing test article along with the air gun results follow (Figure 3.13).

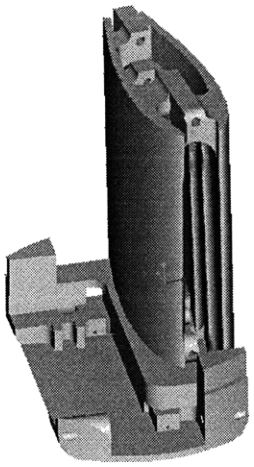

| Test | Load Direction | G Load | Results |
|---|---|---|---|
| 1 | Set Back | 7536 | No Damage |
| 2 | Set Back | 14883 | No Damage |
| 3 | Set Forward | 3673 | No Damage |

**Figure 3.13: Wing Test Article and Results**

## 3.6 Summary

A detailed design of the current WASP vehicle's wing module was presented in this chapter. The main requirements and key aspects of the design were discussed. Through experimental testing, the high-g survivability of the wing system was validated. The lessons learned through the development of the WASP vehicle's wing system were then used to aid in the present research of investigating the design of a composite high-g wing.

# CHAPTER 4

# BACKGROUND

In order to implement a composite wing design, the behavior of composite plates under high-g loading needs to be understood. A review of past work turned up no publications within this specific area of research. However, the buckling behavior of composite plates in axial compression gives some insight as to the behavior that might be observed. Specific to this research, the buckling behavior of curved composite plates needs to be understood. This section will detail previous work on the buckling behavior of plates and shells. Section 4.1 will present different loading conditions for plates and shells. Previous analytical studies on the buckling behavior of plates and shells will be discussed in Section 4.2. Experimental studies on the buckling behavior of plates and shells will then be presented in Section 4.3. Section 4.4 will describe previous work that has been focused on the dynamic buckling response of plates and shells.

## 4.1 Loading Cases for Plates and Shells

The buckling behavior of plates and shells can be studied by applying different types of loads (See Figure 4.1). The buckling behavior of plates is studied by applying an in-plane axial compressive load to the plate. The buckling response of curved shells is either characterized by applying an axial load or a transverse load to the shell. Similar to the plate loading, the axial load

for a shell is an in-plane load. The transverse load is characterized by an applied out-of-plane load.

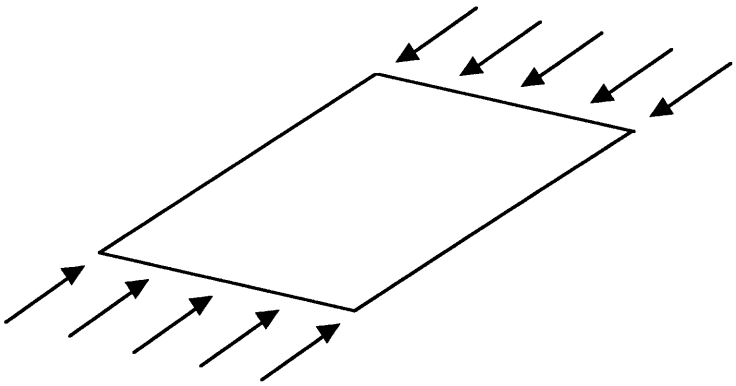

a) Axial Loading of Plate

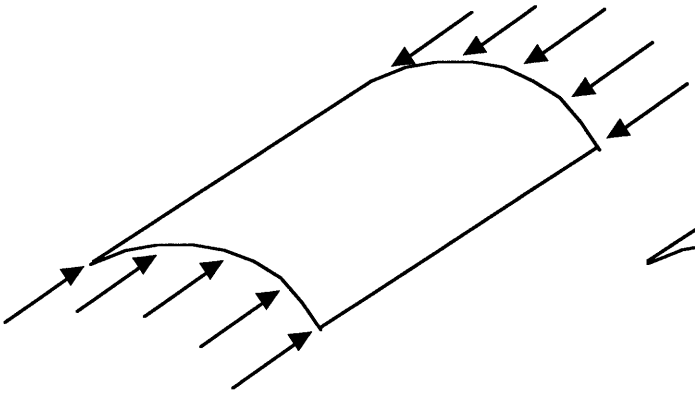

b) Axial Loading of Shell

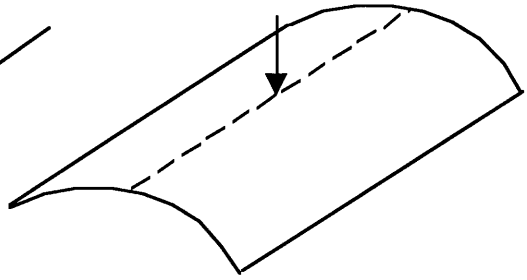

c) Transverse Loading of Shell

**Figure 4.1: Schematic of Buckling Loading Cases**

This research investigates the buckling behavior of curved composite panels under an axial compressive load, therefore, the following discussion of previous work will be limited to the axial loading of plates and shells. The buckling behavior of axially loaded structures is characterized by the state in

which the in-plane load reaches a point where the original structure is no longer in an equilibrium state. If the applied load is less than the critical buckling load, the structure only undergoes axial compression and remains stable. However, when the load reaches a critical value, the structure becomes unstable and laterally deflects out of plane. This buckling behavior for plates and shells subjected to axial loading has been given considerable attention and is well understood.

## 4.2 Analytical Studies

There has been much effort in the past years to analytically characterize the buckling behavior of plates and shells. This section discusses the theories that have been developed to characterize the buckling response of both isotropic and composite plates and shells.

### 4.2.1 Isotropic Plates and Shells

The buckling behavior of isotropic plates and shells has been given considerable attention and is well understood. The classical plate theory for determining the critical buckling load of isotropic plates and shallow shells can be found in a number of text books [16-18]. However, these closed form analytical solutions exit only for simple geometries, loadings, and boundary conditions.

### 4.2.2 Composite Plates and Shells

The analytical study of composite plates in compression can be broken down into two categories: classical thin plate theory and shear deformation theory [19].

#### 4.2.2.1 Classical Laminated Plate Theory

The first of these categories, classical thin plate theory, ignores the effects of shear strains, normal strain, and normal stress in the transverse direction. This theory is commonly referred to as classical laminated plate theory [20]. This theory, which is an extension of the classical plate theory for isotropic plates, is used to study the behavior of laminated plates. Classical laminated plate theory is restricted to the analysis of thin plates that consist of orthotropic layers of material.

In classical laminated plate theory, the constitutive relations, equilibrium equations, and compatibility equations are used to form the governing buckling differential equations for a laminated composite plate. The governing equations can be set up and solved for both plates and shells. In the case of shells, an extra curvature term needs to be added to the constitutive law. A common method used for solving the governing differential equations is the Rayleigh-Ritz energy method. The idea behind the Rayleigh-Ritz energy method is to minimize the total potential energy of the system. This method assumes displacements that satisfy the geometric boundary conditions. These assumed displacements are then introduced into the total potential energy equation, and through a minimization, a system of linear equations is obtained. The solution to this set of linear equations can then be obtained by solving the standard eigenvalue problem. The critical buckling load is given by the lowest eigenvalue of the system.

#### 4.2.2.2 Shear Deformation Theory

The second of these theories, shear deformation theory, is a more advanced theory [19, 21-23]. These theories take into account the transverse shear deformations. For thin plates and shells, the first-order deformation theory produces good results. Higher-order theories also exist and must be

used for thick laminates in order to take into account the effects of cross-sectional warping. This research only looks at thin plates and shells, so the discussion will be limited to the first-order shear deformation theory.

The first-order shear deformation theory takes into account a constant transverse deflection and thus uses shear correction coefficients. The shear correction factors are introduced in the constitutive law of the laminated plate. Similar to the classical laminated plate theory, the governing differential equations, which take into account the transverse shear, can then be solved The solution of this problem is again obtained as the solution to a standard eigenvalue problem.

#### 4.2.3 Results of Analytical Studies

In general, these analyses have highlighted two key issues relevant to the current research described in this thesis. First, the boundary conditions are very important in defining the analytical problem since they govern the assumed deflections. Second, initial curvature plays a critical role in determining the buckling load of shells. The critical buckling load of the panel increases with an increase in curvature.

### 4.3 Experimental Studies

The buckling behavior of composite plates has also been studied experimentally [24, 25]. Similar to the analytical studies, the focus of the work has been on simple geometries, loadings, and boundary conditions. The primary loading case has been limited to uniform distributed compressive edge loading. The prescribed boundary conditions have also been very limited. Experimental work has examined such configurations as square composite plates, simply supported on all edges [24]. Also configurations with shells have

been studied [25]. However, these again were for simple boundary conditions such as clamped boundary conditions for the curved edges and either simply supported or clamped boundary conditions for the straight edges.

In general, the correlation between the experimental results and analytical results is good. Also two key points that were made throughout the experimental work are that the boundary conditions and imperfections of the composite structures effect the buckling response.

## 4.4 Dynamic Buckling Response

One area of research that directly relates to the gun launch environment is that of dynamically impacted composite plates. In both cases, the plate is suddenly loaded for a short duration. In previous work, the dynamic buckling behavior of plates has been studied both analytically and experimentally.

### 4.4.1 Analytical Studies

The analysis of dynamic buckling for axial loading has covered isotropic and composite plates. The most comprehensive treatment of this work is in a series of papers by Hutchinson and Budiansky [26,27]. They developed an analytical model for imperfect panels of isotropic material that are suddenly loaded and held at a constant load for a finite length of time. The model relates the dynamic buckling load to the static buckling load. The results of the analytical model show that for a perfect structure the dynamic buckling load could be several times larger than the static buckling load, for an imperfect structure the dynamic buckling load is closer to the static buckling load. However, when applying this analytical model, there are two necessary conditions that must be met. The first is that the inertia associated with the

pre-buckling mode of the deformation of the structure must be negligible. The second is that the dynamic buckling mode must be the same as the static buckling mode. Also this model can not be justified in studying the dynamic buckling load when the length of the time of the load application is very short. Similar to the work on isotropic plates, the dynamic buckling behavior of composite plates has been studied [28]. The results support the conclusion that the dynamic buckling load is higher than the static load.

### 4.4.2 Experimental Analysis

Previous work has also been performed to understand the dynamic buckling behavior of composite structures [29] Similar to the isotropic analysis, the results support the conclusion that the dynamic buckling load is higher than the static load. Experimental work done by Abranovich and Grunwald [29] on flat composite plates show that the dynamic load factor, ratio of dynamic buckling load to static buckling load, is usually above one.

### 4.4.3 Conclusions

The review of past work has lead to two main conclusions concerning dynamically loaded structures. The first observation is that the dynamic buckling load is generally greater than the static buckling load. The second is that the dynamic buckling behavior is not well understood for short duration, high load level impacts.

# CHAPTER 5

# MODELING

This chapter describes the finite element modeling that was performed in order to predict the buckling behavior of composite wing sections under high-g loading. Initially, the first wing section of the current WASP wing design was investigated and modeled as a constant thickness curved panel. Subsequently, the model was used to predict the buckling behavior of composite panels. The validity of the finite element model was investigated through experimental testing.

## 5.1 Overview

I-DEAS™ Master Series and ABAQUS™ Version 5.8 were used to construct the finite element models. All of the pre- and post-processing was performed with I-DEAS™ Master Series. The processing of the models was done within ABAQUS™.

I-DEAS™ Master Series was used to construct the model geometries. Both the wing geometry and the constant thickness curved panel geometry were created as three-dimensional configurations. The geometries were meshed using standard I-DEAS™ solid and shell elements where possible. In the case of the wing geometry, a solid brick mesh element had to be developed.

ABAQUS™ was used to define the material properties, boundary conditions, and loading conditions of each model. With the above information,

ABAQUS™ solved for the critical buckling load factor, which is a multiplier of the perturbation load. The total buckling load, P, is given as

$$P = P^N + \lambda Q^N \qquad [5.1]$$

where $P^N$ is the base state load, $Q^N$ is the perturbation load, and $\lambda$ is the multiplier. The structure's stiffness, K, at this load state can be described as

$$K = K_P^{NM} + \lambda K_Q^{NM} \qquad [5.2]$$

where $K_P^{NM}$ is the base state stiffness and $K_Q^{NM}$ is the perturbation stiffness. The critical buckling load factor is then calculated by setting up the standard eigenvalue problem

$$[K_P^{NM} + \lambda_i K_Q^{NM}]\Phi_i^M = 0 \qquad [5.3]$$

where $\lambda_i$ are the eigenvalues that represent the multipliers which provide the buckling load and $\phi_i$ are the eigenvectors that represent the corresponding mode shapes. The critical buckling load corresponds to the lowest eigenvalue. ABAQUS™ uses an iteration method to converge on the solution [30]. The code generated within ABAQUS™ can be found in Appendix A.

I-DEAS™ is used to post-process the results from ABAQUS™. The profile of the original configuration along with the displacement profile are displayed. Also the calculated critical buckling load factor is given.

## 5.2 Model of Original Wing Design

Initially the original WASP wing design was modeled. This section details the model that was developed for the wing profile and the model that was developed to simplify the design to a constant thickness curved panel.

### 5.2.1 WASP Wing Finite Element Model

The wing profile and mesh were generated in I-DEAS™ by producing a NASTRAN™ code. A Pro-Engineer™ model of the current wing existed from previous work on the WASP design. Using Pro-Engineer™, a cross section profile of the wing design was obtained. On Pro-Engineer™ this cross section was meshed into quadrilateral units using a finite element tool within the program. The data points for the spline to create the wing profile along with the data points necessary to generate the mesh were then exported to a NASTRAN™ file. The NASTRAN™ file was then modified to make the two dimensional profile into a three-dimensional model with eight node solid elements. The following figures show the model that was generated in I-DEAS™.

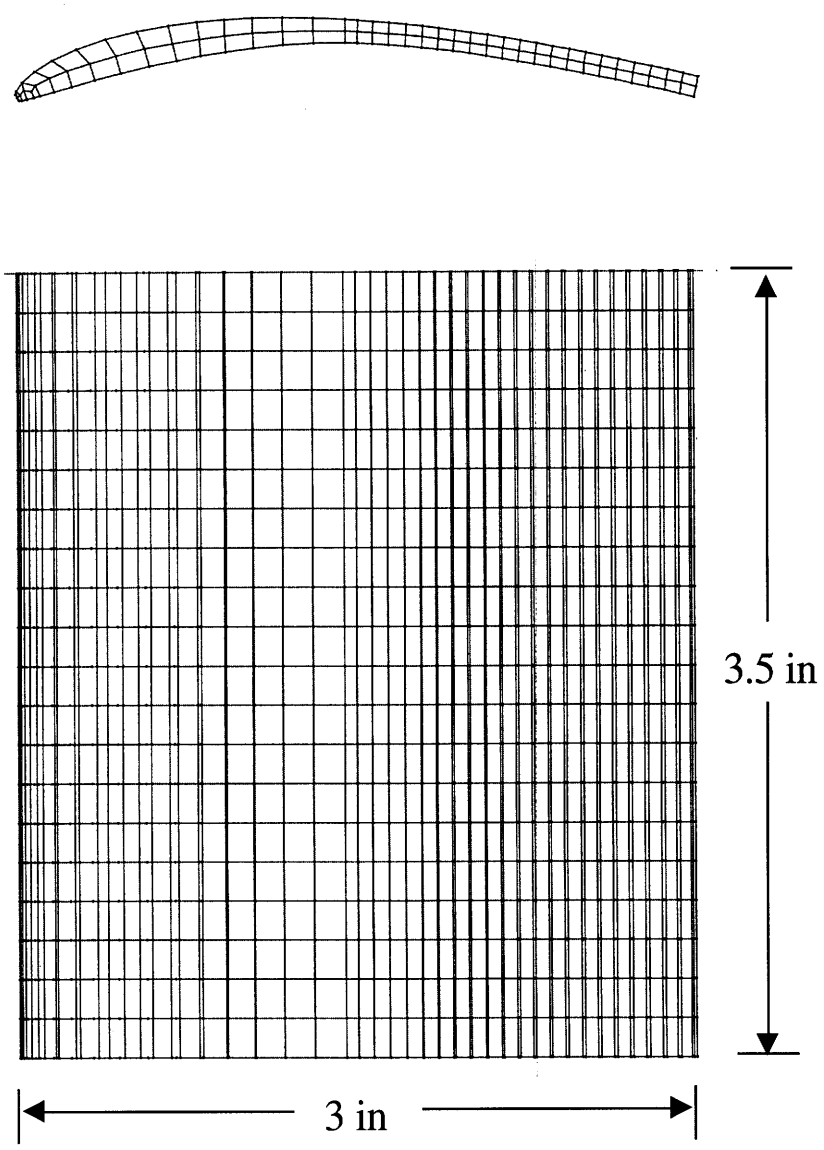


**Figure 5.1: Wing Geometry and Mesh**

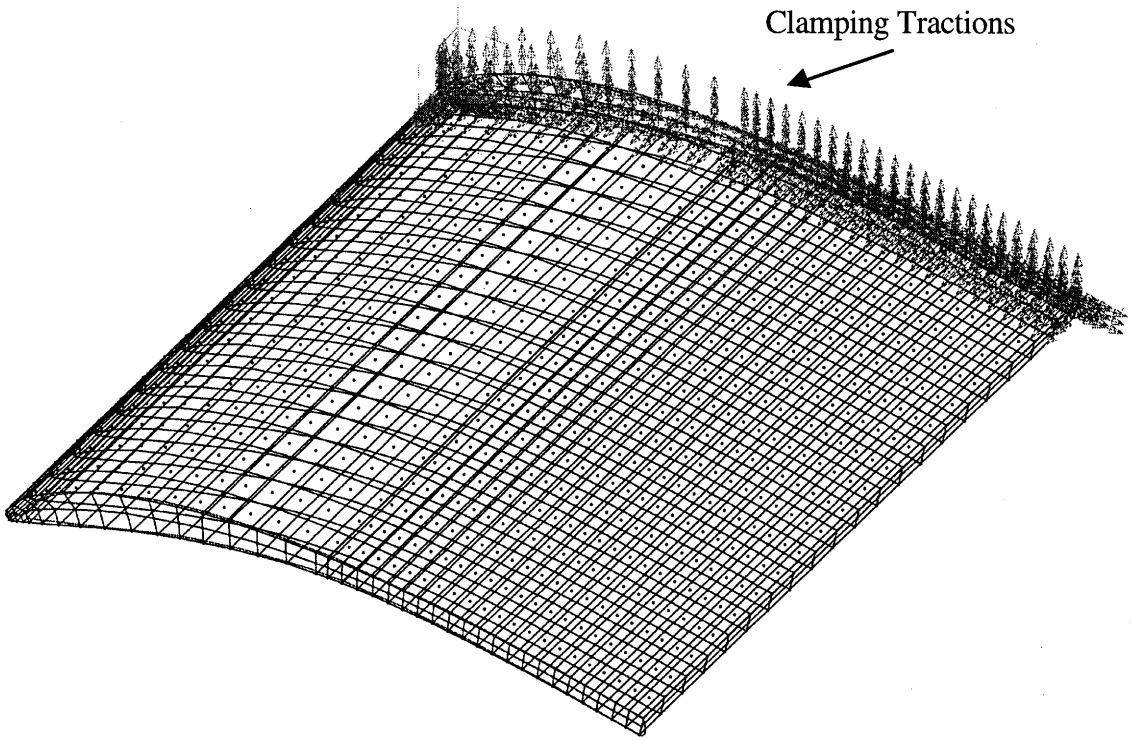


**Figure 5.2: Three Dimensional Model of Wing With Boundary Conditions**

ABAQUS™ was used to calculate the critical buckling load factor. The model used material properties for aluminum 7075, with a modulus of 71 GPa, a Poisson's ratio of 0.3, and a density of 2800 kg/m$^3$. At the bottom edge of the model, a clamped boundary condition was applied to all of the nodes (See Figure 5.2). A gravity load of 15,000g's was applied to all of the elements within the model to represent the launch conditions in the gun environment.

The model was post-processed in I-DEAS™. The prediction for the critical buckling load factor of the original WASP wing design was 7.07, which corresponds to a load of 106,050 g's. The original WASP wing was designed so that the first section could support the weight of the other five sections at

launch. However, due to the stacking sequence that was developed for the wing segments, this was not the case. For the model that was developed, the analysis investigated the first wing section with the assumption that the first wing section would only have to support its own weight. This is the reason that the predicted critical buckling load is large and the wing appears over-designed.

In order to validate the model, the wing design used for the pivot test (See Section 3.4.1) was investigated. The pivot test article was modeled as a small wing section that was meshed using the eight node solid brick elements. The block representing the mass of the other wing sections was treated as a distributed load. The predictions of the model were then compared to the experimental air-gun results. The contour plots of the displacements and stresses can be seen below. The model did not predict that the structure would buckle. However, the model shows a large deflection and a maximum stress of 5.78e12 Pa, which is above the yield strength of aluminum (4.00e8 Pa), at the trailing edge of the wing. This location agrees with where the damage occurred in the actual test article. Thus the model was deemed acceptable, and the results of this analysis were then used to model the wing as a constant thickness curved panel.

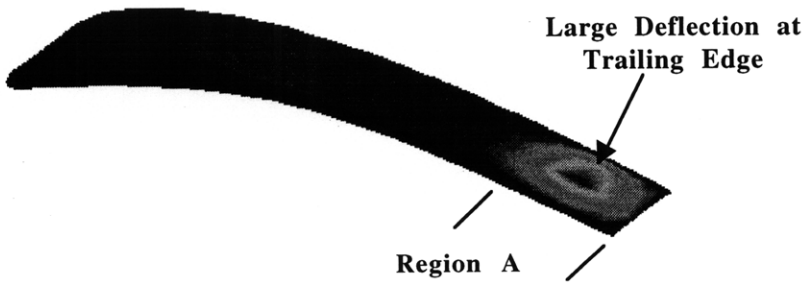


**Figure 5.3: Contour Plot of Deflection**

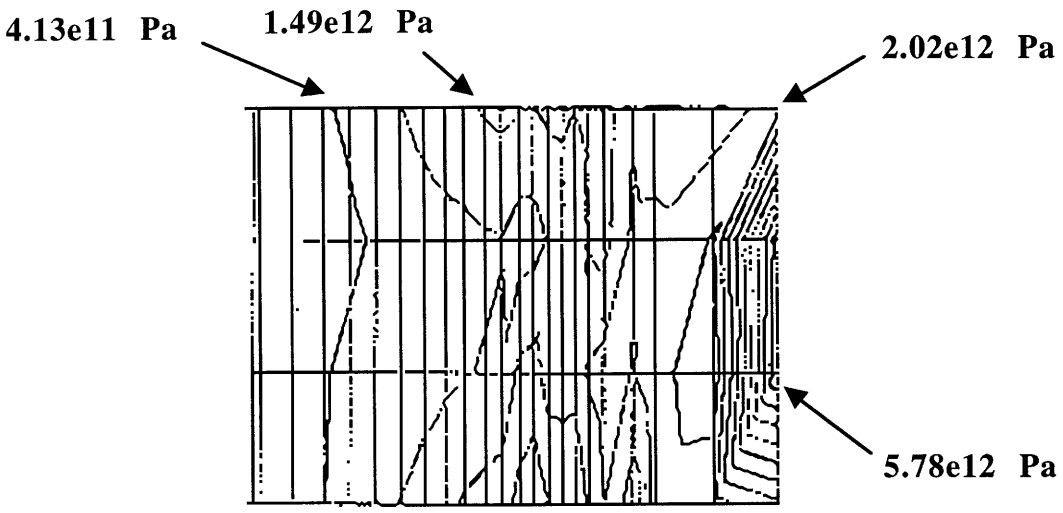


**Figure 5.4: Contour Plot of Stresses at Trailing Edge of Wing (Region A)**

5.2.2 Constant Thickness Curved Panel

The approach that was taken was to model the wing as a constant thickness curved panel. This simplifies the problem to a geometry that can be easily modeled and manufactured. The key aspects of the curved panel geometry that had to be determined were the radius of curvature, length, width, and thickness. The length and width were based exactly on the first section of the wing. The curved panel was assigned a length of 3.5 inches to correspond to the span of the first wing section. The panel was assigned a width of 3 inches to correspond to the chord length of the wing. The radius of curvature was determined by taking an average radius of curvature for the wing profile. The radius of curvature that was chosen was 4.5 inches. With these dimensions based on the original wing geometry, the thickness of the panel was determined to be 0.1 inches in order to give the same buckling response as the wing geometry.

The analysis was carried out in the same manner as the wing analysis described above. The model was generated in I-DEAS™ using eight node solid elements. The same material properties, boundary conditions, and loading conditions were assigned to the model. ABAQUS™ was used to calculate the buckling load factor and the first mode shape. The analysis predicted a buckling load factor of 7.04, which corresponds to a loading of 105,600 g's.

The above analysis showed good agreement between the two models. Compared to the analysis of the WASP wing design, the panel's critical buckling load factor only differed by 0.4%. Also both models demonstrated the same first mode shape. The following figure shows the original geometry and the deformed mesh for both models (See Figure 5.5). Both of the models deflect against the curvature of the geometries. Also, the maximum deflection of the curved panel is approximately equal to the maximum deflection of the wing, which occurs at the trailing edge. The analysis verified that the first wing section could be reasonably modeled as a constant thickness curved panel with the above dimensions.

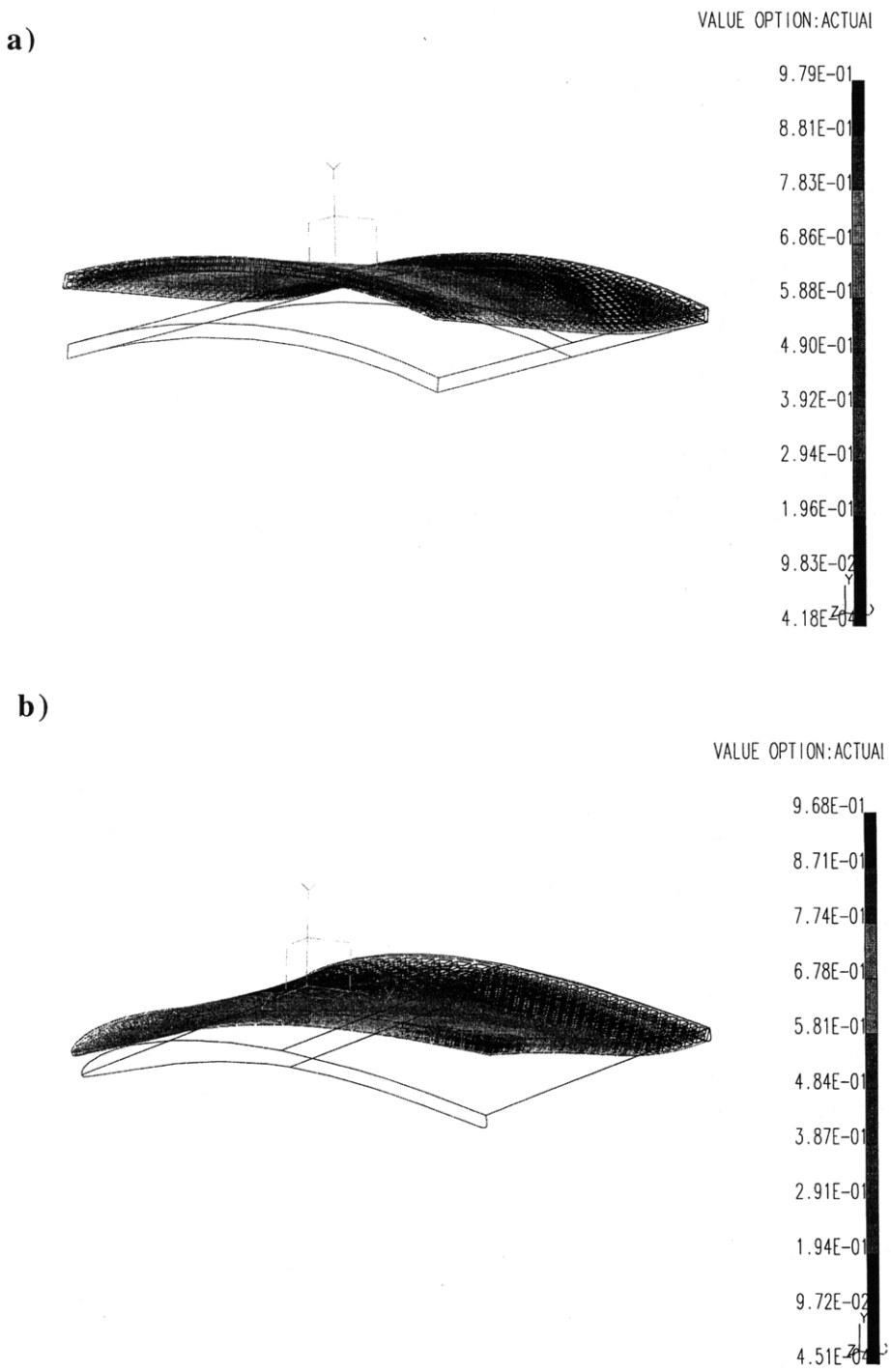


**Figure 5.5: Original Geometry and Deformed Mesh of the First Mode**

**a) for curved shell with equivalent cross-sectional properties to**

**b) the original WASP wing**

## 5.3 Constant Thickness Curved Composite Panels

The model that was constructed to represent the wing as a constant thickness curved panel was modified to include the analysis of laminated composites. This section describes the modifications that were made to the model and the final configurations that were analyzed.

### 5.3.1 Construction of Model

The composite panels were analyzed in a similar manner as the previously described analysis for the aluminum panel. The main differences were the material properties assigned to the model, and the elements used in constructing the model.

The material properties assigned to the model were based on those of AS4/3501-6, the material used in manufacturing the panels for testing. The following table summarizes the material properties for AS4/3501-6:

| Material Property | Value |
|---|---|
| $E_1$ | 138.0 GPa |
| $E_2$ | 9.0 GPa |
| $\nu_{12}$ | 0.33 |
| $G_{12}$ | 6.9 GPa |
| $G_{13}$ | 6.9 GPa |
| $G_{23}$ | 4.5 GPa |
| Density | 1660 kg/m$^3$ |
| Ply Thickness | 1.27e$^{-4}$ m |

**Table 5.1: Material Properties of AS4/3501-6**

Instead of using eight node solid elements for the mesh, four node shell elements were used. Shell elements were necessary in order to allow for the construction of the composite laminate. Using shell elements, the model can be represented as individual layers of material and each layer can be defined separately. In this way, the thickness and ply orientation for each layer of a composite laminate can be assigned.

The analysis was performed in the same manner for each composite laminate configuration and the predicted buckling load factor was determined. The model was validated by inserting the material properties for aluminum into the shell model and comparing the results with those obtained for the solid model. The following figure shows the model developed for the constant thickness curved composite panels. At the bottom one inch of the sample, a clamped boundary condition was applied to the model in order to represent the conditions that were used for testing (See Section 6.2).

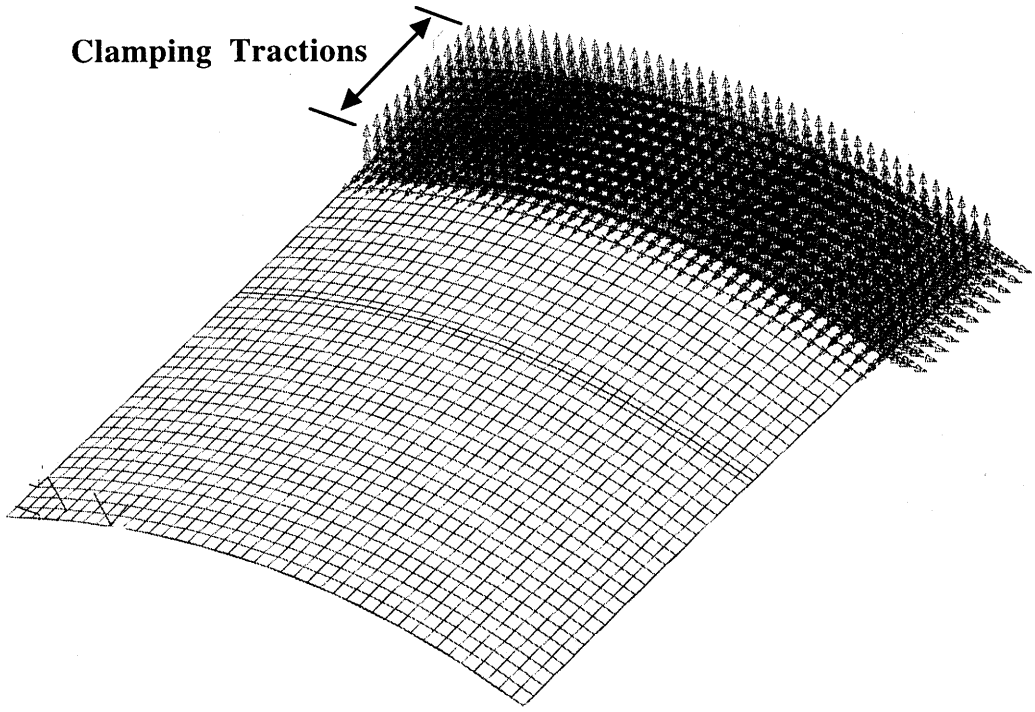


**Figure 5.6: Model of Panel With Boundary Conditions**

5.3.2 Configurations

From the preliminary finite element modeling of the composite panels, four key aspects were identified that affected the panel's critical buckling load factor. The four key aspects were lay-up, curvature, height, and aspect ratio (length to width ratio) of the composite panels. A baseline design was chosen based on the previous analysis that was performed of the original WASP wing and aluminum panel. Variations from the baseline design were chosen so as to investigate each of the key aspects that affect the critical buckling load.

The baseline configuration was a constant thickness cylindrically curved composite panel with a radius of curvature of 4.5 inches, a length of 4.5 inches, a width of 3 inches, and a lay-up of $[0/+45/-45]_s$. The geometry for the baseline

configuration came directly from the panel dimensions in the previous analysis. The one change in the dimensions is the length of the panel. This was due to the fact that the samples needed to be potted for testing purposes. Therefore it was determined that the length of the panel should be increased by one inch so that one inch of the sample could be used for providing the clamped boundary condition during testing. In the analysis, this entire one inch of the sample was modeled and given a clamped boundary condition. The lay-up for the baseline configuration was determined by investigating lay-ups that would be feasible for an actual wing structure. Initially quasi-isotropic laminates were investigated as a starting point. However, after the initial analysis, it was determined that the $[0/+45/-45]_s$ lay-up would work well. This lay-up was chosen because it provided the appropriate range of critical buckling loads that could be obtained in testing and it was also a reasonable lay-up for a wing structure[31]. The zero degree plies aid the structure both in preventing buckling at launch and increasing the bending stiffness during flight. The 45 degree plies provide torsional stiffness during flight.

The configurations for the composite panels were determined based on the baseline design and the key aspects that affect the critical buckling load. Each of the key aspects was investigated separately by taking variations from the baseline design. There were eight different configurations that were both modeled with the finite element analysis and experimentally tested. The results of the analysis along with a comparison to the experimental findings can be found in Chapter 8. The following table shows the configurations of the composite panels.

| Configuration | Lay-Up | Radius of Curvature | Aspect Ratio | Length |
|---|---|---|---|---|
| **Baseline** | $[0/+45/-45]_s$ | 4.5" | 3 : 3.5 | 4.5" |
| **Lay-Up** | | | | |
| Variation #1 | $[0/+60/-60]_s$ | 4.5" | 3 : 3.5 | 4.5" |
| **Curvature** | | | | |
| Variation #1 | $[0/+45/-45]_s$ | 6.0" | 3 : 3.5 | 4.5" |
| Variation #2 | $[0/+45/-45]_s$ | flat plate | 3 : 3.5 | 4.5" |
| **Aspect Ratio** | | | | |
| Variation #1 | $[0/+45/-45]_s$ | 4.5" | 2 : 3.5 | 4.5" |
| Variation #2 | $[0/+45/-45]_s$ | 4.5" | 1 : 3.5 | 4.5" |
| **Length** | | | | |
| Variation #1 | $[0/+45/-45]_s$ | 4.5" | 3.5 : 3 | 4.0" |
| Variation #2 | $[0/+45/-45]_s$ | 4.5" | 3.5 : 3 | 5.0" |

**Table 5.2: Composite Panel Configurations**

# CHAPTER 6

# EXPERIMENTAL PROCEDURES

This chapter describes the experimental procedures that were used in order to investigate the behavior of composites panels under high-g loading. Descriptions of the manufacturing process and experimental testing procedures are included.

## 6.1 Manufacturing Process

This section details the manufacturing process of the composite panels. Included are the descriptions of the material, mandrel, cure cycle, and final preparation.

### 6.1.1 Graphite/Epoxy Pre-Preg

The panels were manufactured out of AS4/3501-6 pre-preg. Standard TELAC procedures were followed when working with AS4/3501-6 [32]. Initially, the pre-preg roll is removed from the freezer and allowed to sit out at room temperature for an hour before it is removed from its sealed storage bag. This procedure ensures that no moisture condenses onto the material. The pre-preg material is then cut using an utility knife. Standard TELAC templates are used to produce the angled plies. The templates ensure that the fibers are continuous for all given angle arrangements.

Once all of the individual plies have been cut, the plies are assembled to form the laminate. This is done by using a squaring device that ensures that there is one square corner. The paper backing is removed from the pre-preg and the individual

plies are stacked in the appropriate order. The final laminate is 12 inches wide by 14 inches long.

### 6.1.2 Cylindrical Mandrel

The cylindrical mandrel manufacturing technique was based on previous work that was performed in TELAC [33]. In this previous research, mandrels were manufactured with radii of 6 inches, 12 inches, and 18 inches. For the present research, the 6-inch radius mandrel was used and a new 4.5-inch mandrel was manufactured.

The mandrel assemblies are manufactured from aluminum. They consist of a base plate, bulkheads, two bottom sheets, and clamping bars. Figure 6.1 shows the mandrel assembly that was used in the manufacturing process.

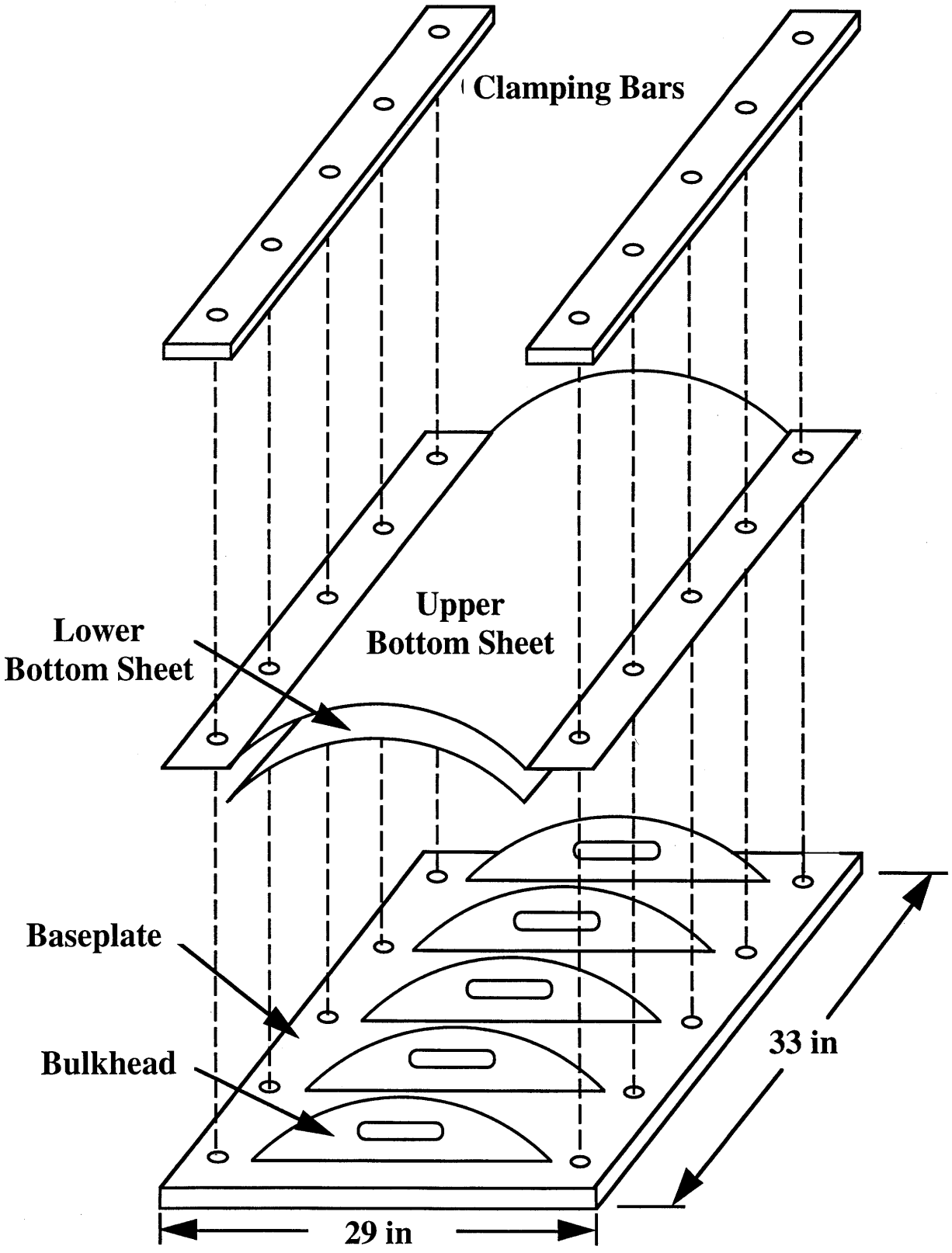


**Figure 6.1: Mandrel Assembly [33]**

The base plate is 33 inches long, 29 inches wide, and 3/8 inches thick. There are five bulkheads, for both the 6-inch and 4.5-inch radii, that are bolted into grooves in the baseplate. The bulkheads are each 3/8 inches thick and have a hole through their center to ensure that equal pressure is obtained during the curing process. Each of the two bottom sheets of aluminum are 32 mils thick. A sheet metal roller was used to roll the bottom sheets to the appropriate radius. It was found that with only one bottom sheet, the bulkheads would locally deform the aluminum sheet and give it a ribbed effect. Using two bottom sheets, this problem was avoided and a smooth cylindrical surface was obtained. The two bottom sheets were held in place using clamping bars.

### 6.1.3 Cure Process

The lay-up process varied slightly from the standard TELAC cure procedures [32]. The steps that were performed in the cure process are discussed in depth below.

The first step was to properly prepare all of the surfaces for the lay-up. All of the aluminum surfaces were cleaned using acetone. Tape was then placed around the outer inch of the mandrel to keep the surface clean for vacuum bagging. The surface was then sprayed with Mold Wiz ™, a mold release which helped prevent the epoxy from adhering to the aluminum sheet. Three coats of Mold Wiz were applied to the surface. The tape was then removed and the non-coated surface was cleaned with acetone. Guaranteed nonporous teflon (GNPT) was then flash-taped to the aluminum surface. The GNPT covered the entire Mold Wiz™ surface, leaving approximately an inch on every edge uncovered for vacuum tape.

The laminate was then placed on the mandrel. The laminate was originally manufactured as a flat panel, but was easily formed to the curvature of the mandrel. Special care was taken to assure that the laminate was lying square on

the mandrel by using a T-square. The rolled top plate, which was the same size as the laminates and 20 mils thick, was then placed over the top of the laminate. The top plates had been prepared by coating them with Freekote™, a releasing agent, and then covering them with guaranteed nonporous teflon. To ensure that the GNPT did not wrinkle, the top plate was sprayed with Spray Mount; the GNPT was then placed on the top plate and the wrinkles were worked out by hand. Small cork dams, approximately an inch long, were then placed at the length-wise edge of the laminate to prevent it from moving during the cure process. The top plates were then covered with bleeder paper, and then a layer of air breather was placed on top.

The final step was to assemble the vacuum bag. A slot was made in the slightly oversized vacuum bag for the vacuum port. The vacuum port was placed directly on the mandrel. Special care was taken to ensure that the vacuum port was not placed on top of the laminate's top sheet in order to prevent damage to the samples during the curing process. Vacuum tape was then applied around the outer edge of the mandrel surface, taping down the vacuum bag. The vacuum was checked to ensure that there were no leaks before curing. Figure 6.2 shows a schematic of the entire cure assembly that was used.

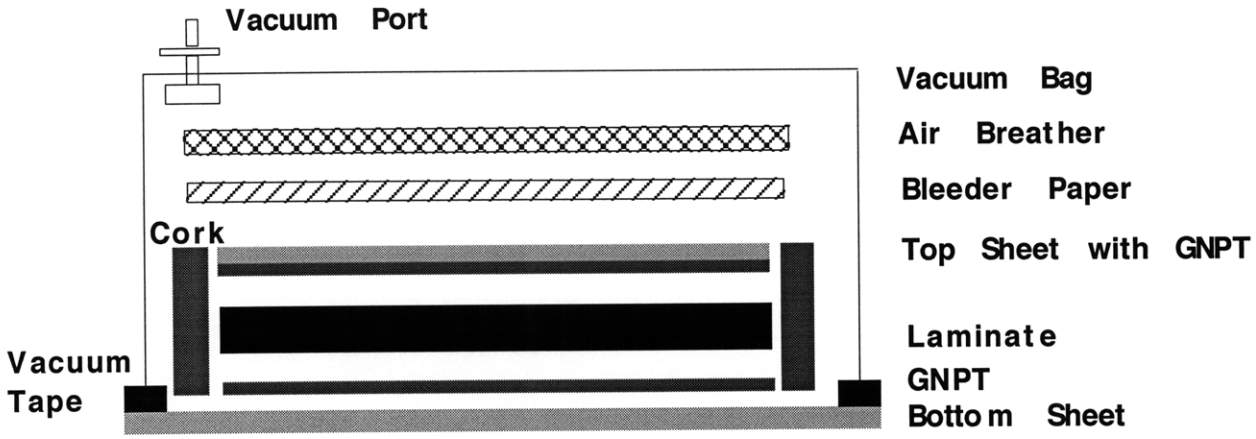


**Figure 6.2: Cure Assembly**

The standard cure cycle for AS4/3501-6 was used [32]. A vacuum of 25-30 inches of mercury was pulled on the sample and maintained throughout the cure cycle. Initially, the autoclave was pressurized to 85 pounds per square inch. The temperature was then increased to 240 degrees Fahrenheit and the sample was held at this temperature for one hour. Next the temperature was increased to 350 degrees Fahrenheit and held at this temperature for 2 hours. The cool-down process was then performed; the sample was brought down to 180 degrees Fahrenheit by cooling the sample five degrees every minute. The pressure and vacuum were then released and the sample was removed from the autoclave. The laminates were removed from the mandrel and post-cured at a temperature of 350 degrees Fahrenheit for 8 hours. The standard cure temperature, pressure, and vacuum profiles can be seen in Figure 6.3.

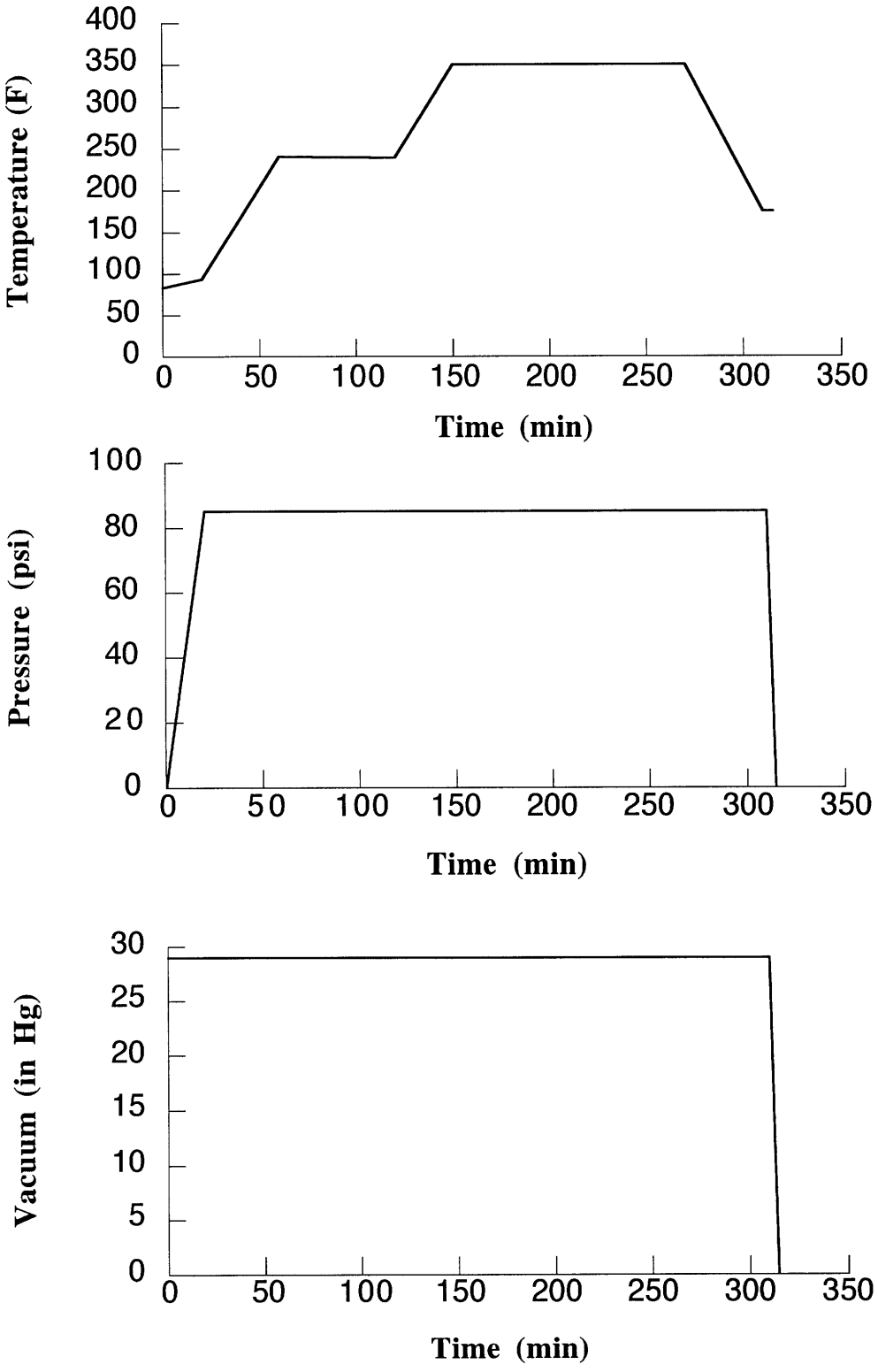


**Figure 6.3: Temperature, Pressure, and Vacuum Profiles for Cure Cycle**

6.1.4 Post-cure Preparation of Samples

The laminates were cured as 12 inch by 14 inch panels. After the curing process, the panels were machined to the appropriate sizes. Due to some damaged areas that occurred during curing, each panel had a different cutting configuration. The panels were machined by the MIT central machine shop. A mounting fixture was made and used to guide the panels as they were cut to ensure that the sides were parallel and there was no waviness in the cut. Due to the cylindrical shape, a 9 foot carbide band saw blade was used to cut the panels. The samples were cut into the appropriate sizes (See Table 5.2).

In the machining process, some of the samples were damaged. The damage consisted of rounded edges and not perfectly parallel sides. There were also some delaminated areas on the edge of the samples where the blade caught the fibers. All of the samples were investigated and all of the damaged areas were noted.

## 6.2 Test Fixtures

In order to obtain the appropriate boundary conditions for experimental testing, a special test fixture had to be designed and machined. The test fixture was designed to give one end of the composite panels a clamped boundary condition. Also the test fixture was designed to be compatible with both the mechanical compression tests and the air gun tests.

The design for the test fixture is based on the dimensions of the 5-inch air gun canister (Figure 6.4). The fixture is manufactured out of Aluminum 7075. It is a solid disc that has two grooves manufactured into it for holding the samples in place. The diameter of the fixture is 3.85 inches, which is governed by the size of the air gun canister. The test fixture is 1.5 inches thick and contains two machined grooves that are each one inch deep. The samples are held in place in the test fixture by a crystalline wax substance (CA #790) manufactured by Greater

Southwest Chemicals, Inc. Wax is first melted into the groove and then the sample is placed into the slot. The composite sample is held in its vertical position by using a T-square as the wax flows and surrounds the sample. The fixture and wax is then allowed to cool. As the wax hardens, it holds the sample in place, creating the clamped boundary condition.

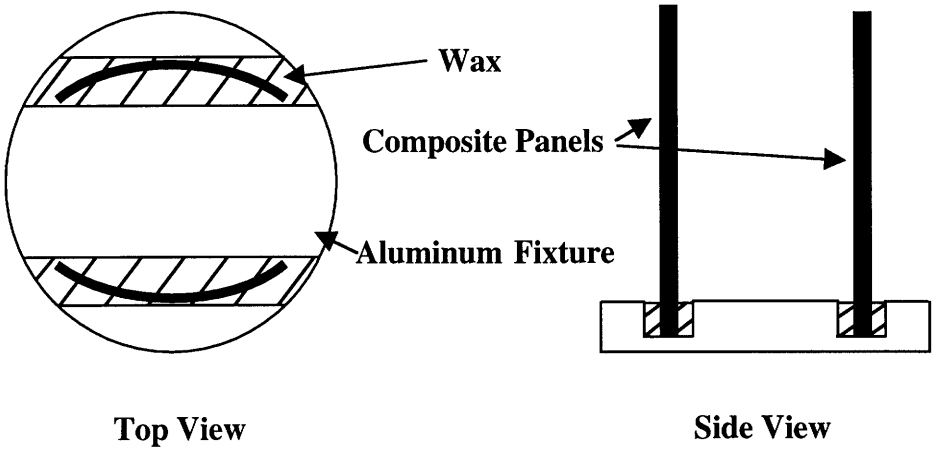


**Figure 6.4: Test Fixture**

For the MTS test machine, only one sample was potted at a time. For the gun tests, two samples were potted at a time, allowing two samples to be tested simultaneously. Also, a slight modification had to be made to the test fixture for the air gun tests. In order to lock the test fixture in place in the canister during testing, a support rod was added to the fixture. This required a hole to be drilled through the test fixture. The set-up will be discussed in more detail in the testing section.

## 6.3 Testing

The following section describes the tests that were performed. Both the mechanical compression tests and the air gun tests are described.

### 6.3.1 Test Matrix

From the finite element model, four key aspects that affect the critical buckling load were identified: lay-up, radius of curvature, aspect ratio, and length. Each of these key elements was investigated using both the MTS machine and air gun tests. In order to ensure that adequate data was obtained, three tests for each configuration were performed except in one case. For the air gun test, only one sample was tested for the configuration that had an aspect ratio of 2:3.5 due to an inadequate number of samples. The following table summarizes the configurations and the number of samples that were tested.

| Configuration | Mechanical Tests | Air Gun Tests |
|---|---|---|
| **Baseline** | 3 | 3 |
| **Lay-Up** | | |
| Variation #1 | 3 | 3 |
| **Curvature** | | |
| Variation #1 | 3 | 3 |
| Variation #2 | 3 | 3 |
| **Aspect Ratio** | | |
| Variation #1 | 3 | 1 |
| Variation #2 | 3 | 3 |
| **Length** | | |
| Variation #1 | 3 | 3 |
| Variation #2 | 3 | 3 |

**Table 6.1: Test Matrix**

6.3.2 Controlled Axial Compression Tests

Controlled axial compression tests were carried out using the MTS hydraulic testing machine with an Instron digital controller. The tests were used to investigate the critical buckling load of the curved composite samples.

#### 6.3.2.1 Test Configuration

The following picture (Figure 6.5) shows the test set-up for the MTS test machine. The test sample was potted in the test fixture. This was then placed on the bottom platen. The sample was centered in order to ensure proper loading. The bottom platen was then raised until the sample just barely touched the top platen. This gave the sample one clamped boundary condition at the test fixture, and one frictionally pinned boundary condition where the top platen rests on the sample.

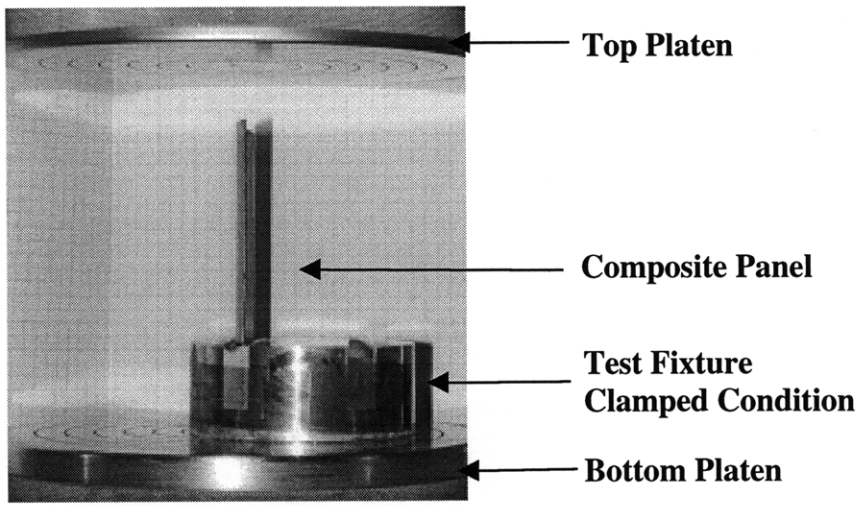


**Figure 6.5: Instron Test Machine**

#### 6.3.2.2 Data Acquisition

The main data that was obtained through the controlled axial compression tests was the critical buckling load. All the tests were performed using displacement control. The displacement rate was set at 0.01 inches per minute. For each of the samples, LabVIEW was used to record the load and the displacement data. Also, three of the samples were instrumented with back to back strain gauges. For these samples, the strain readings were also recorded. Data was recorded for each sample from before loading, through buckling, and until first ply failure as seen by the dramatic loss in load carrying capability.

6.3.3 Picatinny Arsenal Testing

In order to simulate the launch conditions experienced during an actual live gun firing, air gun tests along with shock table tests were performed at Picatinny Arsenal in Dover, NJ. Initially, the plan was to use the 5-inch air gun to conduct all of the tests. However, due to unforeseen circumstances, some of the tests were carried out using the 5-inch air gun and shock table, but most were carried out with the 155-millimeter air gun. The following figure shows the acceleration profiles that can be obtained from both guns as well as the acceleration profile for an actual live gun.

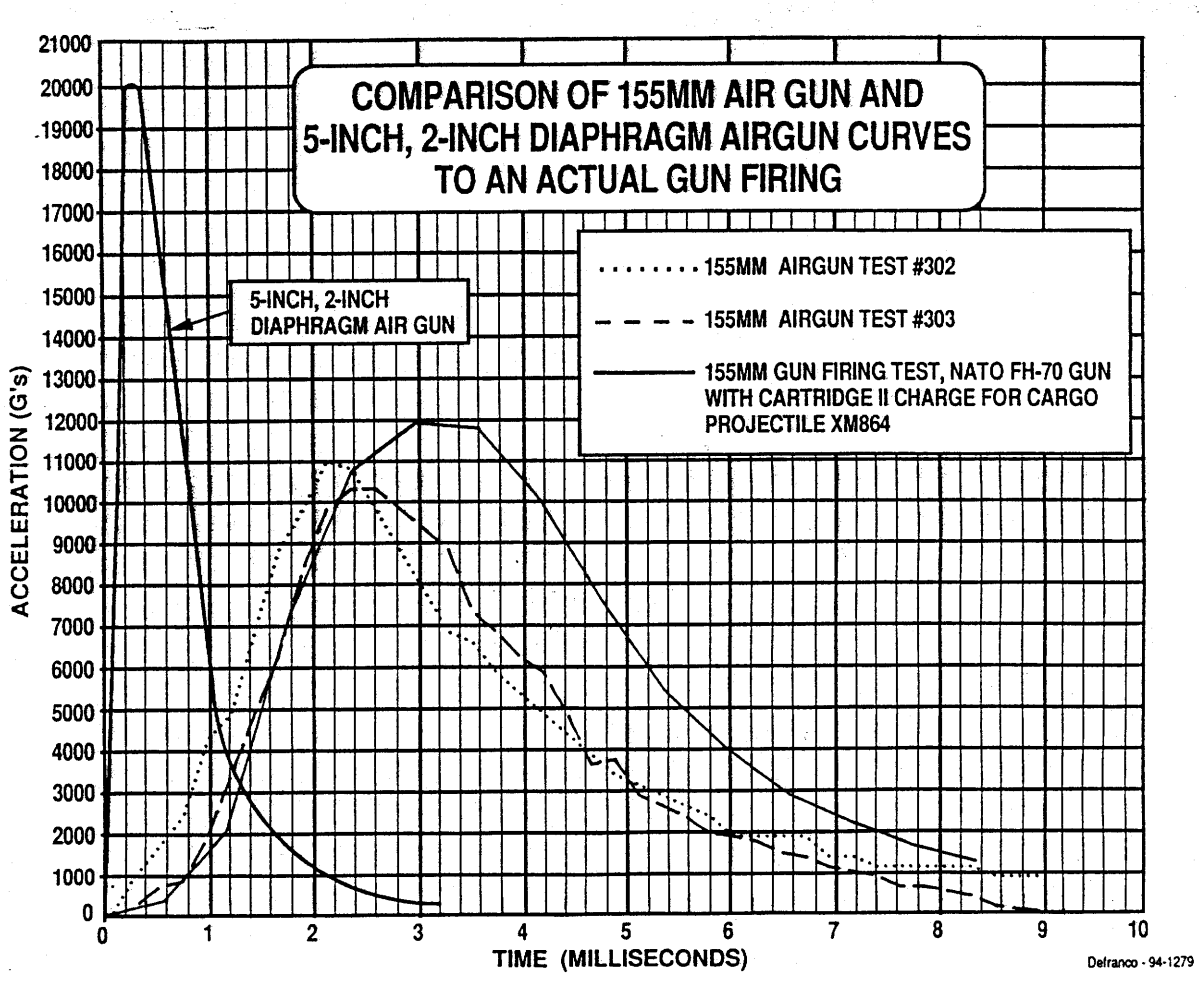


**Figure 6.6 Acceleration Profiles**

### 6.3.3.1 Five-Inch Air Gun

The general premise behind the 5-inch air gun was discussed in Section 2.4.1. In this section, the specific tests that were performed with the composite samples are described in more depth.

The 5-inch air gun uses compressed air to accelerate a canister down a test chamber. To do this, the gun builds up pressure behind an aluminum diaphragm that is attached to the test canister. When a critical pressure is obtained, the diaphragm shears and the test canister is accelerated down the barrel of the gun and into the test chamber. Meanwhile, at the other end of the test chamber, a muzzle pressure is built-up so that as soon as the test canister is fired, this back-pressure is released and decelerates the test canister.

The thickness of the diaphragm is selected based on the desired acceleration. However, the exact acceleration is not known until after the test is completed. This uncertainty is due to the fact that the diaphragm could fail at a higher or lower pressure than predicted. Therefore, the shot can be fired at an acceleration of plus or minus 2,000 g's. However, when the shot is fired, the exact pressure where the diaphragm broke and accelerometer reading are recorded. From this information, the acceleration that the canister experienced can be determined.

The test canister for the 5-inch air gun was manufactured out of aluminum 7075. The canister consists of a cylindrical test section and a back-end nut and bolt system (See Figure 6.7). The test section of the canister has an inner diameter of 3.9 inches and a height of 9.315 inches. The test section is then sealed by attaching a threaded lid to the canister. The back-end of the test canister consists of a nut and bolt system that is used to attach the diaphragm to the canister. The diaphragm is placed onto the bolt and slid up against the test section of the canister. The nut is then used to lock the diaphragm in place during firing.

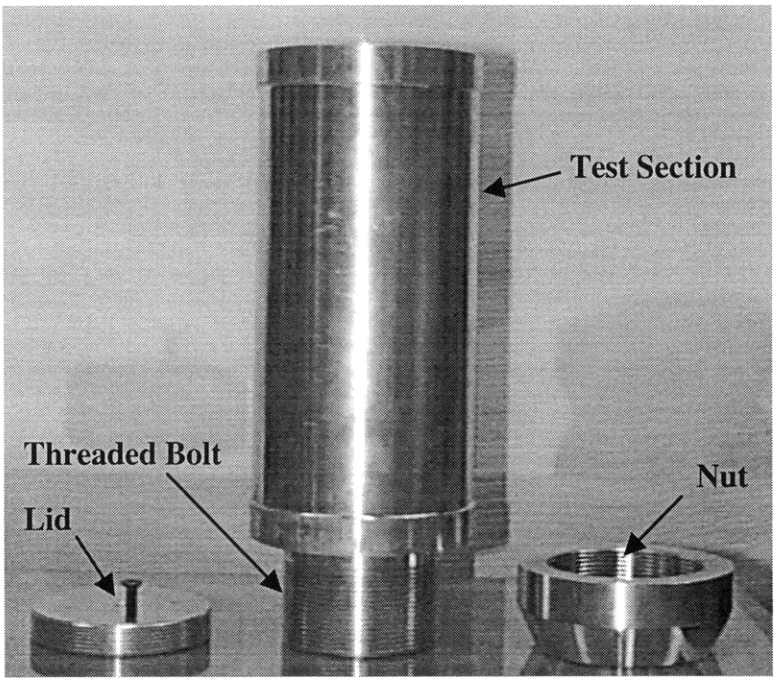


**Figure 6.7: Photograph of the Test Canister**

Three shots, each with two samples, were fired with the 5-inch air gun. For each of the shots, two samples were potted with wax in the test fixture as described in Section 6.2. A solid aluminum rod, with a diameter of 1 inch and length of 7 inches, was attached to the test fixture in order to hold the test article in place during testing.

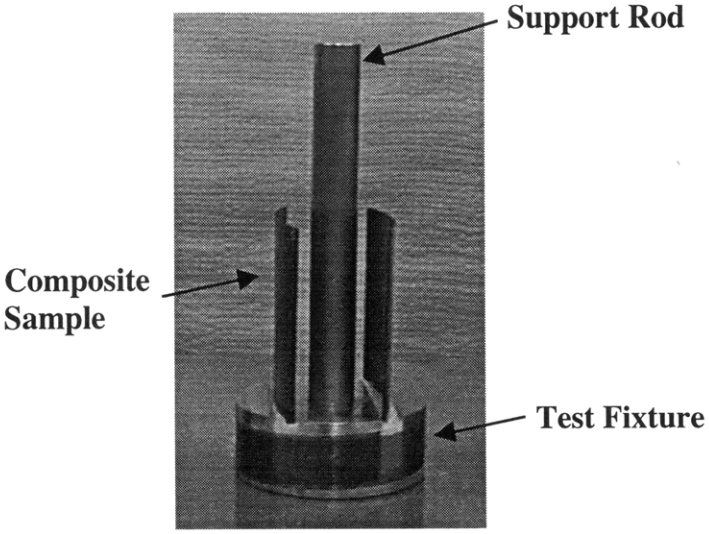


**Figure 6.8: Photograph of Test Article for 5-Inch Air Gun Tests**

The test article was then inserted into the test canister. The threaded lid was screwed down onto the aluminum rod and held the whole set-up in place within the canister. The test fixture provided a clamped boundary condition at one end of the sample and a free boundary condition at the other three. An accelerometer was attached to the lid of the canister. The entire canister was then fired down the test chamber at the desired acceleration. The pressure at which the diaphragm broke along with the acceleration profile was obtained. The samples were then visually inspected for any signs of failure.

#### 6.3.3.2 155-Millimeter Air Gun

The 155-millimeter air gun varies slightly from the 5-inch air gun. As seen in Figure 6.6, the 155-millimeter air gun provides an acceleration profile which more closely approximates that of a live firing. The main disadvantage of using the 155-millimeter air gun for testing is that the gun can not produce as high an acceleration as the 5-inch air gun. With the test configuration as described above, the 155-millimeter gun could not produce an acceleration above 20,000 g's. However, this did not prove to be detrimental given the desired g-loadings.

Similar to the 5-inch air gun, the 155-millimeter air gun uses compressed air to accelerate a canister down a test chamber. However, the mechanism for producing the acceleration is quite different. The 155-millimeter air gun utilizes a pressure sleeve, into which the test canister is inserted. This is then loaded into breach of the gun. Pressure is built up in the gun chamber, but unlike the 5-inch gun, the pressure completely surrounds the test canister. When the desired chamber pressure is obtained for the desired acceleration, the canister is then released from the sleeve and accelerated down the chamber. The 155-millimeter air gun allows the shot to be fired more precisely at the desired acceleration, however, the canister can not be instrumented with an accelerometer. Therefore, the acceleration that is achieved must be back calculated from the breech pressure.

The canister for the 155-millimeter air gun consists entirely of a test chamber with an inner diameter of approximately 4.75 inches and a height of approximately 9 inches. Seven shots were fired on the 155-millimeter air gun with accelerations ranging between 10,000 and 20,000 g's. Since the test fixture was designed for the 5-inch air gun, the test article did not fit tightly into the canister. However, it was determined that when the lid was tightened down onto the aluminum support bar, the entire fixture was held in place and did not move laterally during testing.

#### 6.3.3.3 Shock Table

Due to the limitations of the air guns, the tests that required lower accelerations had to be completed using a shock table. Two tests were performed using the shock table. The test article was securely mounted onto the table. The table was raised to a predetermined level based on the desired acceleration. By having the table drop and hit a base plate, a shock with the desired acceleration was imparted to the test article.

#### 6.3.3.4 Summary of Tests

This section summarizes the experimental tests that were performed at Picatinny Arsenal. The tests consisted of 5-inch air gun tests, 155-millimeter air gun tests, and shock table tests. The following table shows the method of testing and the accelerations obtained for each configuration.

| Configuration | Acceleration #1 | Acceleration #2 | Acceleration #3 |
|---|---|---|---|
| **Baseline** | 15,000 | 20,000* | 25,600* |
| **Lay-Up** | | | |
| Variation #1 | 15,000 | 20,000 | 20,500 |
| **Curvature** | | | |
| Variation #1 | 10,000 | 16,500 | 20,000 |
| Variation #2 | 1,000+ | 4,200+ | 6,700* |
| **Aspect Ratio** | | | |
| Variation #1 | 20,500 | | |
| Variation #2 | 4,200+ | 6,700* | 10,000 |
| **Length** | | | |
| Variation #1 | 10,000 | 20,000 | 25,600* |
| Variation #2 | 10,000 | 16,500 | 20,000* |

* Indicates test performed on 5-inch air gun
+ Indicates test performed on shock table
All other tests performed with 155-millimeter air gun

**Table 6.2: Summary of Tests at Picatinny Arsenal**

# CHAPTER 7

# RESULTS

The results from the finite element modeling and the experimental testing are presented in this chapter. The numerical results from the finite element modeling include the critical buckling load and deflection characteristics. The experimental results are discussed for both the controlled axial compression tests and the testing performed at Picatinny Arsenal.

## 7.1 Modeling Results

This section details the results of the finite element modeling. The configurations and modeling approach can be found in Chapter 5. Initially, the predicted critical buckling loads will be discussed. Subsequently, the predicted deflections for the first mode shape will be presented. The last section will discuss the characteristics of the second buckling mode.

### 7.1.1 Critical Buckling Loads

The finite element model, as described in Chapter 5, was used to investigate the buckling behavior of each composite configuration. The panels were modeled with one clamped boundary condition and three free edges. The load was applied in the form of an axial acceleration, with a magnitude of 15,000g. The model was used to calculate the lowest eigenvalue, which corresponds to the buckling load factor. The critical buckling load was then determined by multiplying the applied load (15,000 g's) by the buckling load

factor. The following table summarizes the critical buckling load results of the finite element model (Table 7.1).

| Configuration | Buckling Load Factor | Critical Buckling Load (g Load) |
|---|---|---|
| **Baseline** | 1.69 | 25,400 |
| **Lay-Up** | | |
| Variation #1 | 1.48 | 22,100 |
| **Curvature** | | |
| Variation #1 | 1.35 | 20,300 |
| Variation #2 | 0.240 | 3,600 |
| **Aspect Ratio** | | |
| Variation #1 | 1.66 | 24,900 |
| Variation #2 | 0.355 | 5,320 |
| **Length** | | |
| Variation #1 | 2.38 | 35,800 |
| Variation #2 | 1.10 | 16,500 |

**Table 7.1: Critical Buckling Load Results from the Finite Element Model**

7.1.2 First Buckling Mode

The finite element model was also used to determine the first buckling mode of the panels. In the analysis of the first buckling mode, two distinct mode shapes were predicted. The first of these, which will be referred to as the twist mode, characterizes the behavior of most of the panels. At the free edge, one of the corners deflects with the curvature of the panel and the other corner deflects against the curvature of the panel. This causes the panel to twist as shown below in Figure 7.1.


**Figure 7.1: Twist Mode**

The second mode shape will be referred to as the bending mode (Figure 7.2). In this case, the panel only deflects in one direction, against the curvature of the panel .

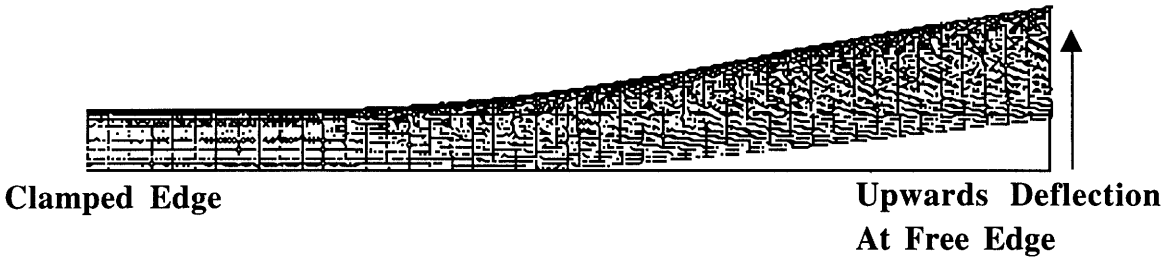


**Figure 7.2: Bending Mode**

The following figures represent the two types of deflected shapes that were observed with the model. The original shape of the panel, along with the deformed mesh can be seen. Figure 7.3 shows the deflected shape of the baseline design, which exhibited the twist mode. Figure 7.4 shows the deflected shape of the flat plate, which demonstrated the bending mode. The twist mode shape was observed in all of the configurations except for two cases: the flat plate and the panel with an aspect ratio of one. These two panel configurations demonstrated the bending mode shape.

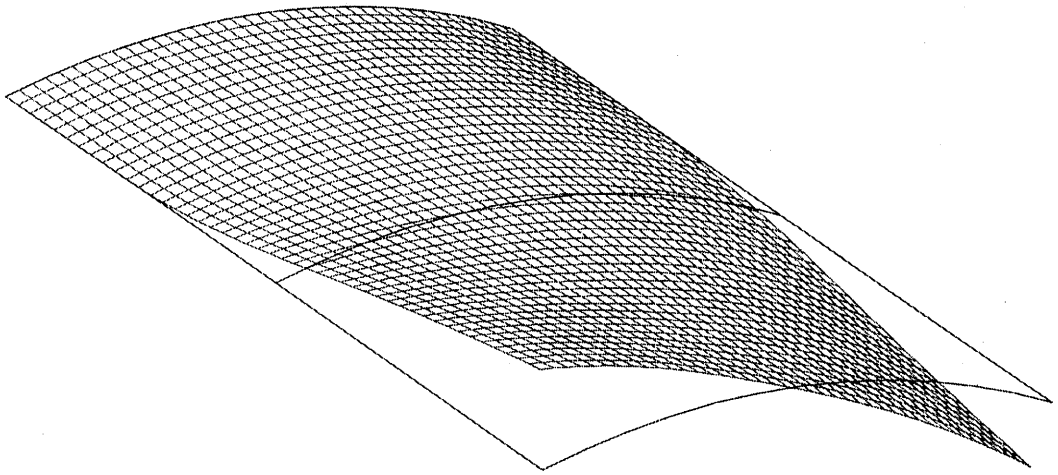

**Figure 7.3: Deflected Shape of Baseline Configuration (Demonstrates Twist Mode)**

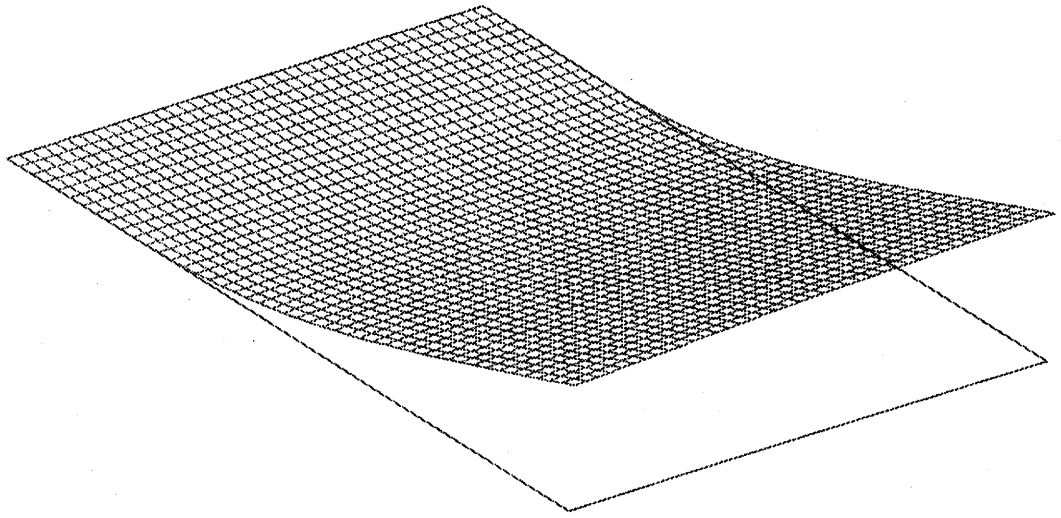

**Figure 7.4: Deflected Shape of Flat Plate Configuration (Demonstrates Bending Mode)**

7.1.3 Second Buckling Mode

The buckling response of a structure is generally governed by the lowest eigenvalue, which represents the critical buckling load, and the corresponding eigenmode, which gives the first buckling mode. However, in order to interpret some of the results that occurred in the experimental testing, the characteristics of the second buckling mode were also investigated. This section will discuss the buckling loads and mode shapes that were associated with the second buckling mode.

To investigate the second buckling mode, the same procedures were performed as discussed in Section 7.1 for the first buckling mode. However, in order to identify the buckling load, the second lowest eigenvalue was used. The

following table summarizes the finite element results for the second buckling mode (Table 7.2).

| Configuration | Buckling Load Factor | Buckling Load (G Load) |
|---|---|---|
| **Baseline** | 3.56 | 53,500 |
| **Lay-Up** | | |
| Variation #1 | 3.98 | 59,700 |
| **Curvature** | | |
| Variation #1 | 3.09 | 46,300 |
| Variation #2 | 0.909 | 13,600 |
| **Aspect Ratio** | | |
| Variation #1 | 2.07 | 31,100 |
| Variation #2 | 2.43 | 36,500 |
| **Length** | | |
| Variation #1 | 4.56281 | 68,442 |
| Variation #2 | 3.16887 | 47,533 |

**Table 7.2: Second Buckling Mode Results from the Finite Element Model**

The mode shapes were also investigated for the second buckling mode. In this case, there were four different mode shapes. Two of the mode shapes, the twist mode and bending mode, were the same as for the first buckling mode. The third shape, which characterizes the behavior of most of the panels, will be

referred to as the corner bending mode. In this case, the two corners at the free edge deflect against the curvature of the panel, while the center section remains in place. The last deflection shape is a combined twist and bending mode.

The following figures demonstrate the deflected shapes that were predicted by the finite element model. The original shape of the panel along with the deformed mesh can be seen. Figure 7.5 shows the deflected shape of the base line design, which exhibited the corner bending mode. The three configurations which did not exhibit this mode shape were the flat plate, the panel with an aspect ratio of two, and the panel with an aspect ratio of one. The flat plate demonstrated the twist mode, which was previously shown in Figure 7.3. As seen in Figure 7.4, the bending mode was exhibited by the panel with an aspect ratio of two. The panel with aspect ratio of one exhibited the combined twist and bending mode (Figure 7.6).

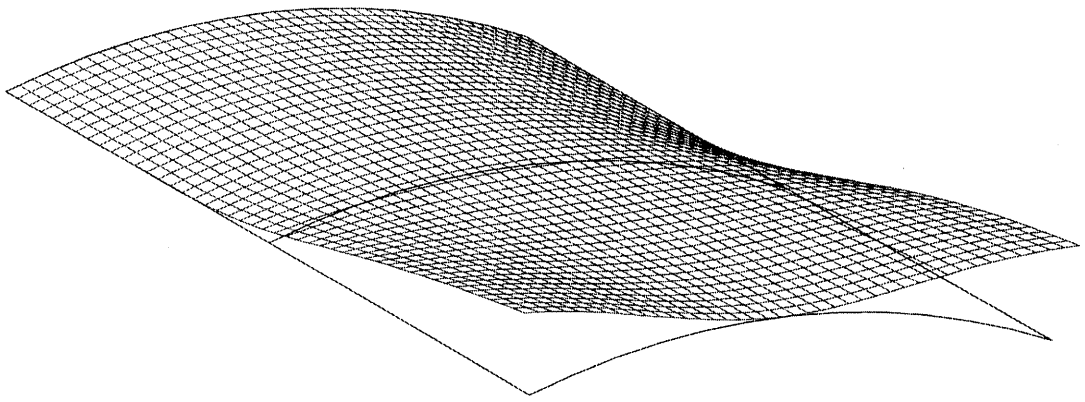

**Figure 7.5: Second Buckling Mode of Baseline Configuration (Demonstrates Corner Bending Mode)**

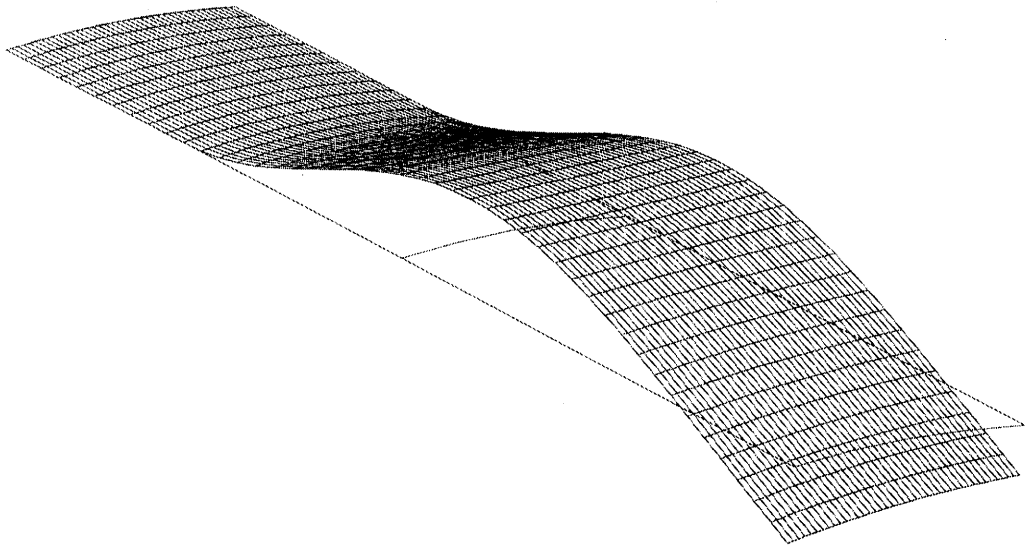

**Figure 7.6: Second Buckling Mode of Panel with an Aspect Ratio of One (Demonstrates Combined Twist and Bending Mode)**

## 7.2 Experimental Results

This section details the results of the experimental testing that was performed. Initially, the axial compression tests will be discussed. Then the tests conducted at Picatinny Arsenal, which include the air gun tests and shock table tests, will be discussed.

### 7.2.1 Controlled Axial Compression Test Results

The axial compression tests were used to investigate the buckling behavior of the composite panels in a controlled setting. The test results characterize the overall loading response of the composite panels. The loading

response of the panels will be presented by discussing the load versus displacement data, the deflection mode shapes, and the critical buckling loads for each panel configuration.

#### 7.2.1.1 Loading Response

The loading response of each tested panel was characterized by a load versus displacement curve. Figure 7.7 shows the load versus displacement curve for one of the baseline samples that was tested. This curve demonstrates the typical response of most of the panels. At low loads, the load increases linearly with displacement. This region is followed by a non-linear region. Finally, the load reaches the limit point, which corresponds to the peak load. This is followed by a region where the load remains constant while the deflection continues to increase, until the first damage occurs. The damage formation is usually associated with a large, sudden drop in the load and a loud cracking sound. Although the load versus displacement curve does not show this, the panels behaved elastically in the sense that they all returned to their original shape as soon as the load was removed. The load versus displacement curves for all of the samples can be found in Appendix B.

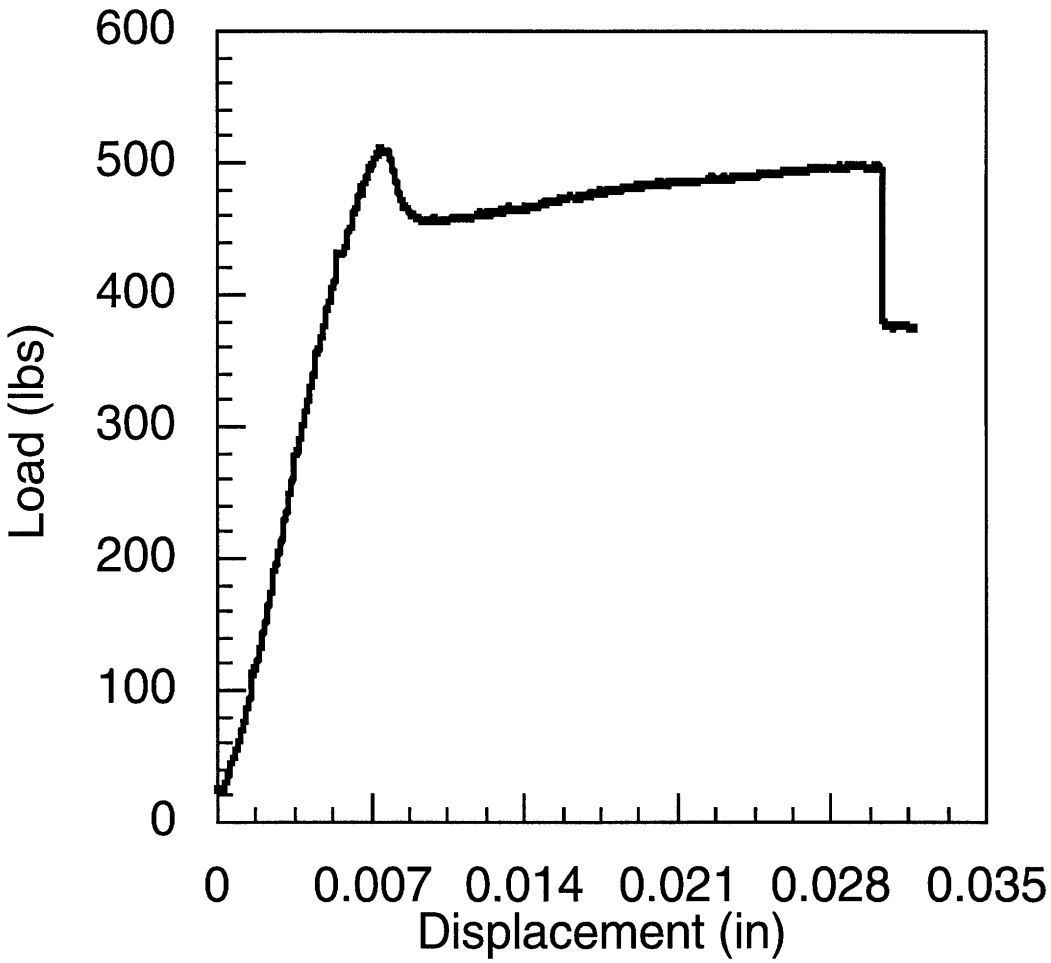


**Figure 7.7: Load-Displacement Curve for Baseline Panel**

### 7.2.1.2 Deflection Mode Shapes

Similar to the finite element analysis, two primary characteristic mode shapes were visually observed. The two shapes again were the twist mode shape and the bending mode shape. These two mode shapes can be seen below in Figure 7.8 and 7.9.

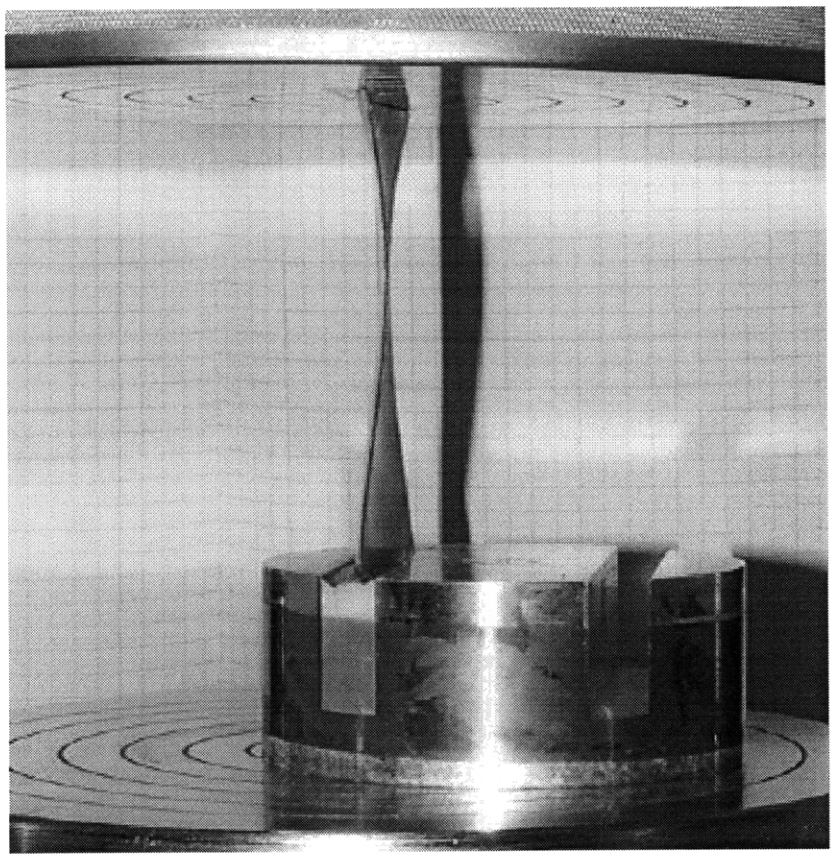

**Figure 7.8: Panel with Six Inch Radius of Curvature Buckling in the Twist Mode During Controlled Axial Compression Test**

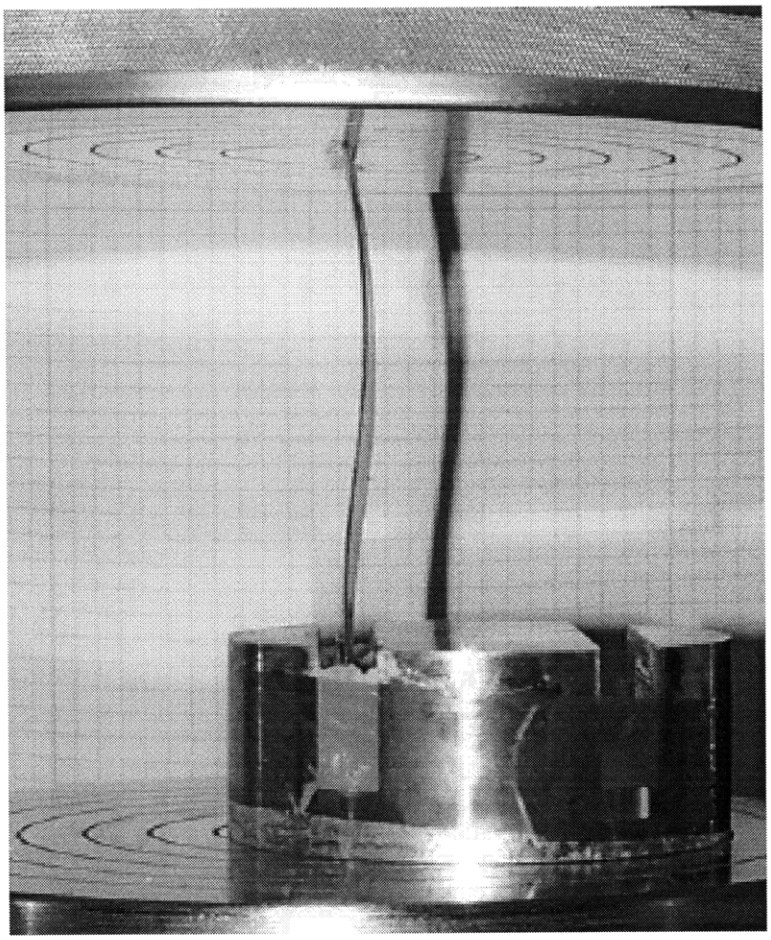

**Figure 7.9: Panel with Aspect Ratio of One Buckling in the Bending Mode During Controlled Axial Compression Test**

However, there were some samples that demonstrated both of these mode shapes. The panel would initially deform into a corner bending mode where the corners of the panel would bend backwards against the curvature. The panel would then suddenly snap into the twist mode shape. This was usually accompanied by a loud popping sound and a sudden drop in the load. Also, the panels that demonstrated this behavior would initially have a higher critical buckling load. However, when the panel went into the twist mode, it would have approximately the same load carrying capability as those panels

that went directly into a twist mode. For example, the following three figures show the load-displacement behavior of the $[0/+60/-60]_s$ lay-up. In this case, one of the samples immediately demonstrated the twist mode and its load-displacement curve can be seen in Figure 7.10. The other two samples originally demonstrated the corner bending mode and then suddenly snapped into the twist mode (See Figures 7.11 and 7.12).

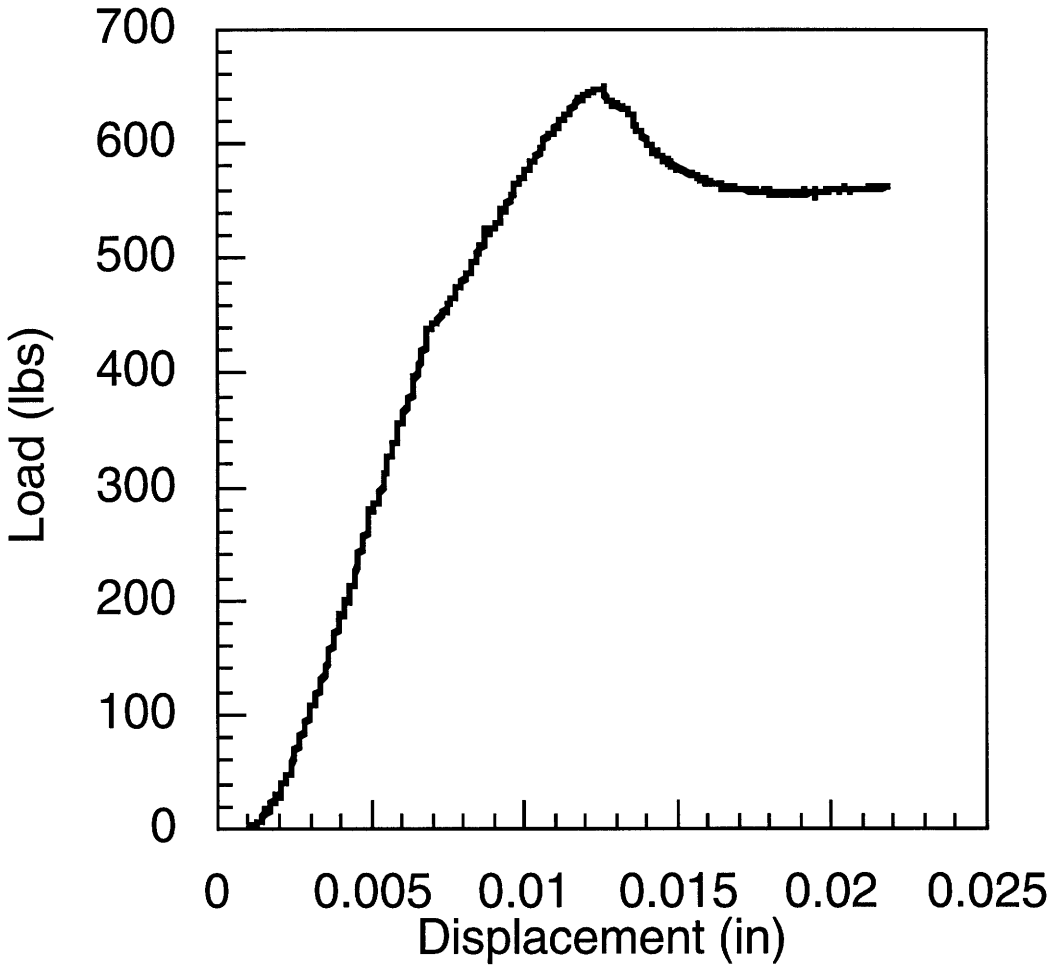


**Figure 7.10: Load-Displacement Curve for [0/+60/-60]s Configuration Which Demonstrates Twist Behavior**

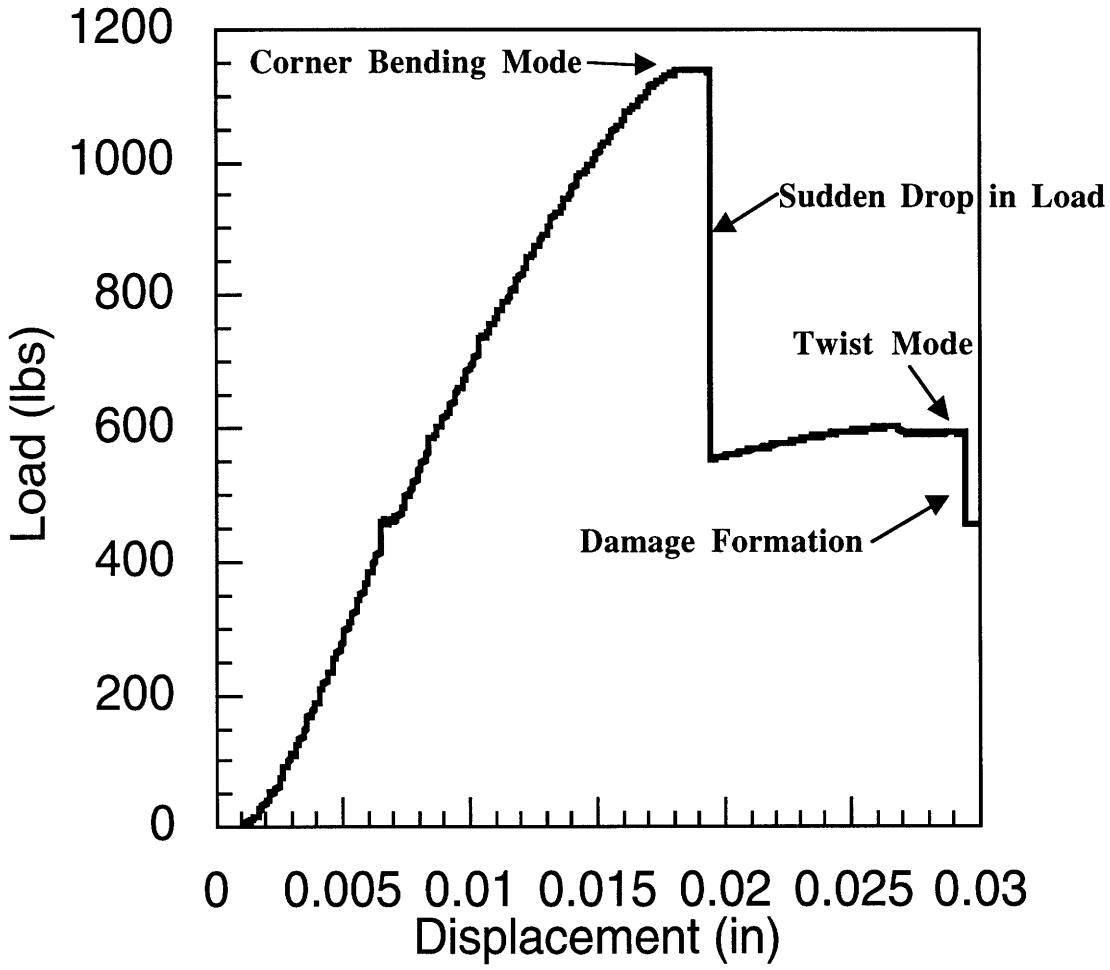


**Figure 7.11: Load-Displacement Curve for [0/+60/-60]s Configuration Which Demonstrates Corner Bending Mode Followed by Twist Mode**

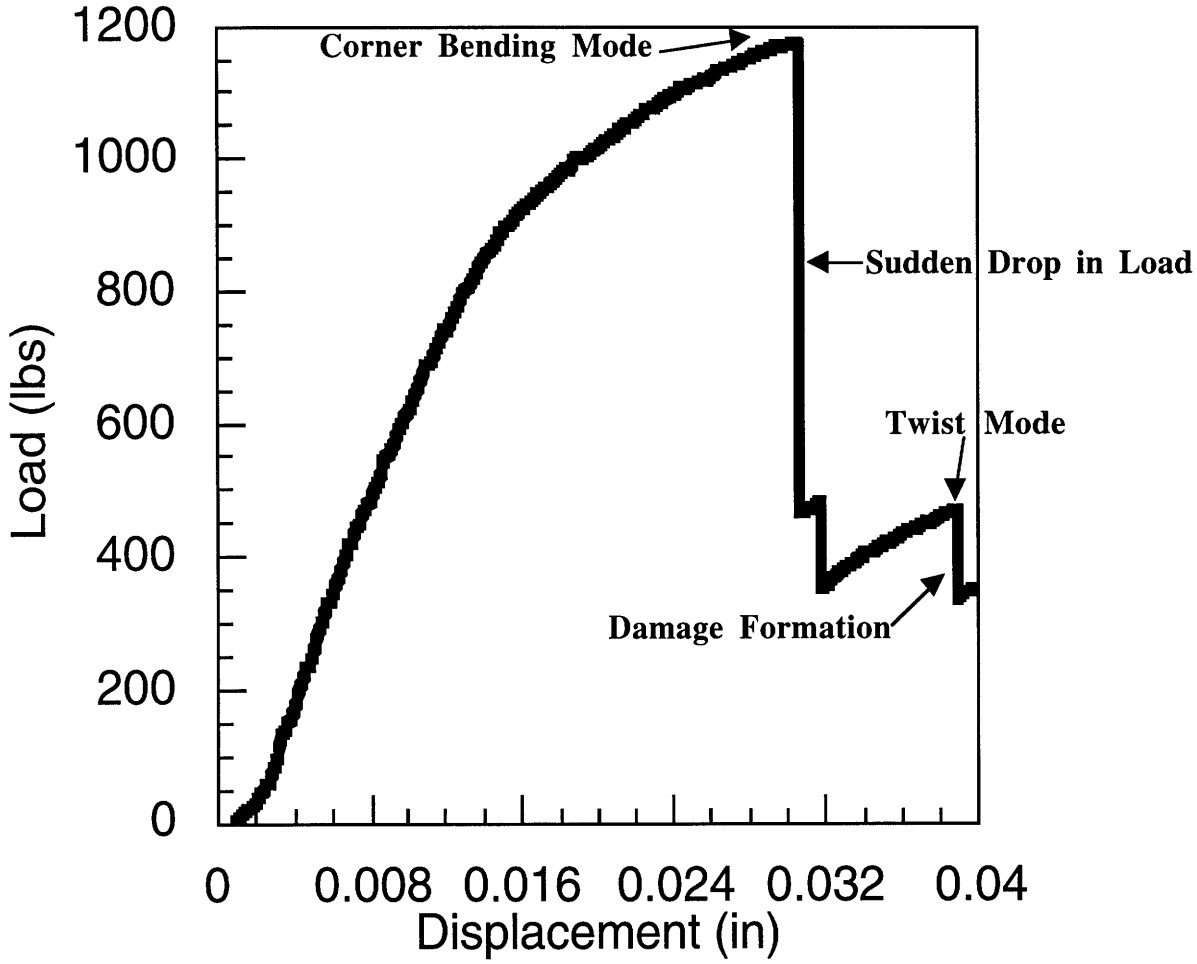


**Figure 7.12: Load-Displacement Curve for [0/+60/-60]s Configuration Which Demonstrate Corner Bending Mode Followed by Twist Mode**

#### 7.2.1.3 Critical Buckling Loads

For each of the samples that was tested, the critical buckling load was determined from the load versus deflection data. The following table summarizes the results of the axial compression tests (Table 7.3). For the samples that demonstrated both the bending and twist mode, the critical buckling load associated with each of the mode shapes is shown.

| Configuration | Critical Buckling Load (lbs) | | Average (lbs) | |
|---|---|---|---|---|
| | Bending | Twist | Bending | Twist |
| **Baseline** | | 510 | 936 | 568 |
| | | 626 | | |
| | 936 | | | |
| **Lay-Up** | | | | |
| Variation #1 | | 648 | 1156 | 572 |
| | 1173 | 467 | | |
| | 1138 | 601 | | |
| **Curvature** | | | | |
| Variation #1 | | 450 | 721 | 496 |
| | 639 | 419 | | |
| | 802 | 619 | | |
| Variation #2 | 192 | | 170 | |
| | 164 | | | |
| | 155 | | | |
| **Aspect Ratio** | | | | |
| Variation #1 | 468 | | 431 | |
| | 472 | | | |
| | 354 | | | |
| Variation #2 | 72 | | 67 | |
| | 65 | | | |
| | 63 | | | |
| **Length** | | | | |
| Variation #1 | | 538 | 802 | 613 |
| | 778 | 568 | | |
| | 827 | 732 | | |
| Variation #2 | | 518 | | 463 |
| | | 450 | | |
| | | 420 | | |

**Table 7.3: Summary of Controlled Axial Compression Tests**

7.2.2 Results of Testing Performed at Picatinny Arsenal

The following section discusses the results of the tests that were performed at Picatinny Arsenal as described in Chapter 6. The 5-inch air gun, 155-mm air gun, and shock table tests were used to investigate the buckling behavior of the composite panels under high-g loading. The load levels and the test method for each panel configuration can be seen in Table 6.2. The loading response of the panels will be presented by first discussing the load profiles that were obtained with each type of test. Subsequently, the results of the experimental testing will be discussed. The last section will present testing that was performed in order to characterize the damage state of the samples.

**7.2.2.1 Load Profiles for High-G Testing**

The 5-inch air gun, 155-mm air gun, and the shock table all have different acceleration versus time profiles. The profiles for the air guns can be seen in Figure 6.7, where they are compared with an actual 5-inch gun acceleration profile. Acceleration profiles were obtained for all of the samples that were tested using either the 5-inch air gun or the shock table. However, those samples that were tested with the 155-mm air gun could not be instrumented with an accelerometer.

For each of the 5-inch air gun tests, the canister was instrumented with an accelerometer. From the accelerometer profile, the air gun's launch acceleration was determined. The data obtained from the acquisition system was averaged to obtain a smoother acceleration profile. The following figure shows a sample plot of the smoothed acceleration profile (See Figure 7.13).

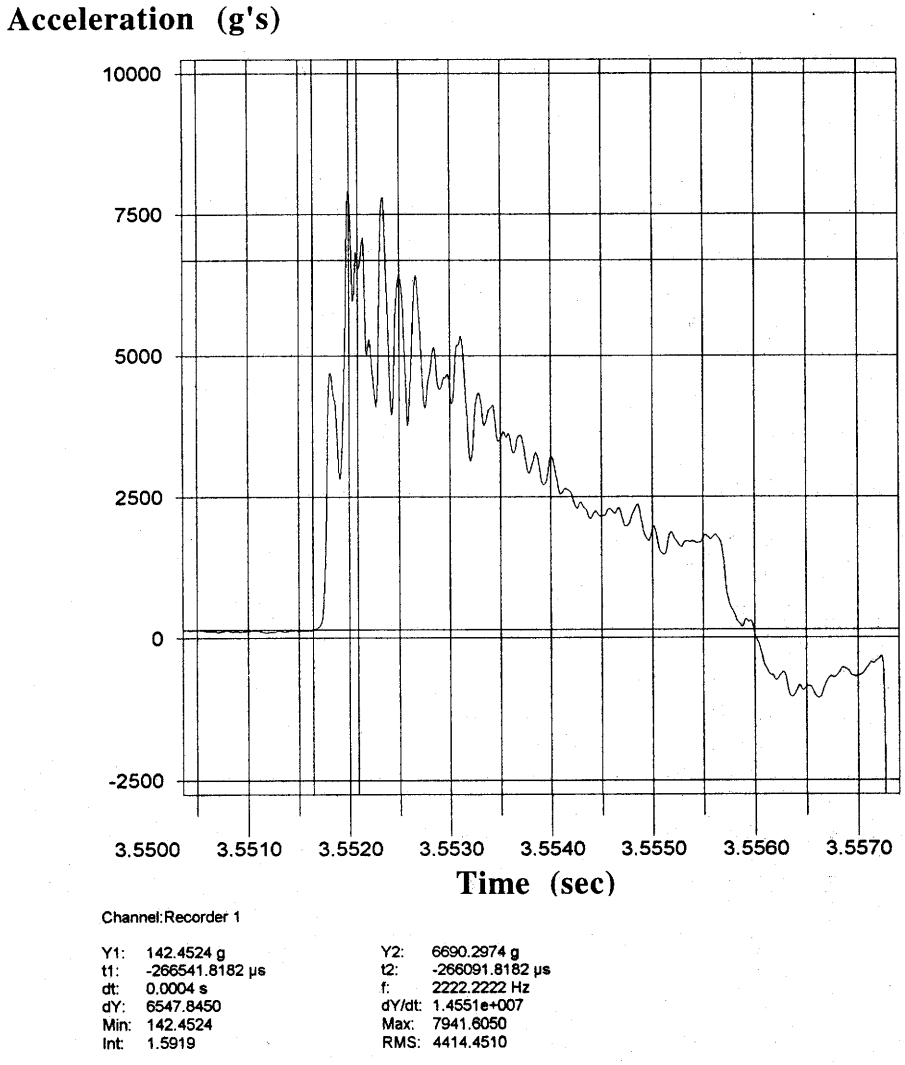


**Figure 7.13: Smoothed Acceleration Profile of 5-Inch Air Gun**

The shock table tests were also instrumented with an accelerometer. The following plot shows a sample acceleration profile that was obtained from one of the tests (See Figure 7.14). Compared to the air gun test, the acceleration profile for the shock table is much cleaner. Therefore, this data was not averaged and the acceleration was determined by taking the peak acceleration from the profile.

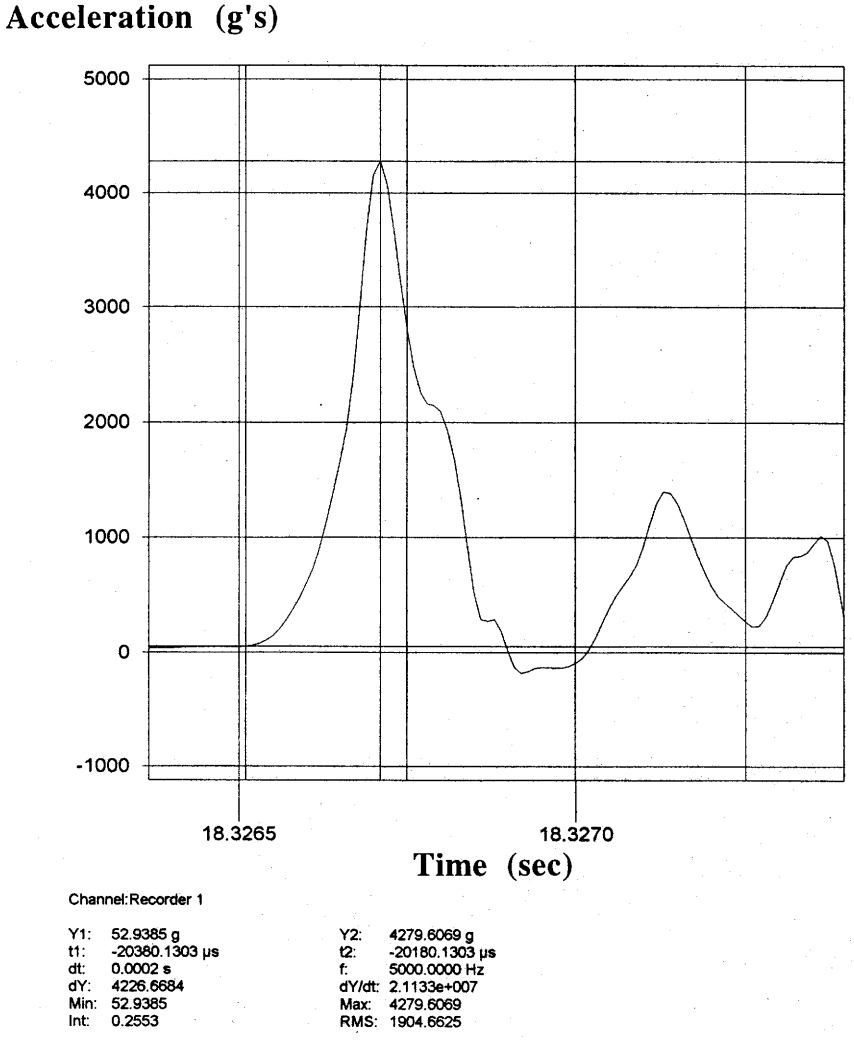


**Figure 7.14: Acceleration Profile of Shock Table Test**

#### 7.2.2.2 Observed Results

All of the sample configurations were tested for loads that were below, at, and above their predicted critical buckling load. After performing the tests, the panels were visually inspected for damage. There were no visible signs of damage to any of the panels. Even when the panels experienced loads that were twice as high as their predicted critical buckling loads, the panels remained intact and were in their original undeformed configurations.

#### 7.2.2.3 Damage Assessment of the Panels

Since the panels showed no signs of visible damage, two approaches were taken to assess whether the panels had experienced internal damage. The first of these approaches was to take x-rays of the samples to determine if there were any areas of delamination or cracks within the samples. In order to investigate the validity of this approach, samples that had previously been tested in the axial compression tests were studied. However, even samples that were known to have buckled and to have experienced fiber damage showed no signs of damage on the x-rays.

The second approach was to retest the samples, as in the controlled axial compression tests, and determine if there was a difference in the loading response of the panels. Figures 7.15 and 7.16 show the buckling load response of test panels that were loaded in the MTS mechanical test machine multiple times. Figure 7.15 shows the load response of a sample panel that was taken to its critical buckling load multiple times. Each time, as soon as the critical buckling load was reached, the load was released and then the sample was loaded again. As can be seen in the Figure 7.15, each consecutive loading showed no sign of loss in the load carrying capability of the panel.

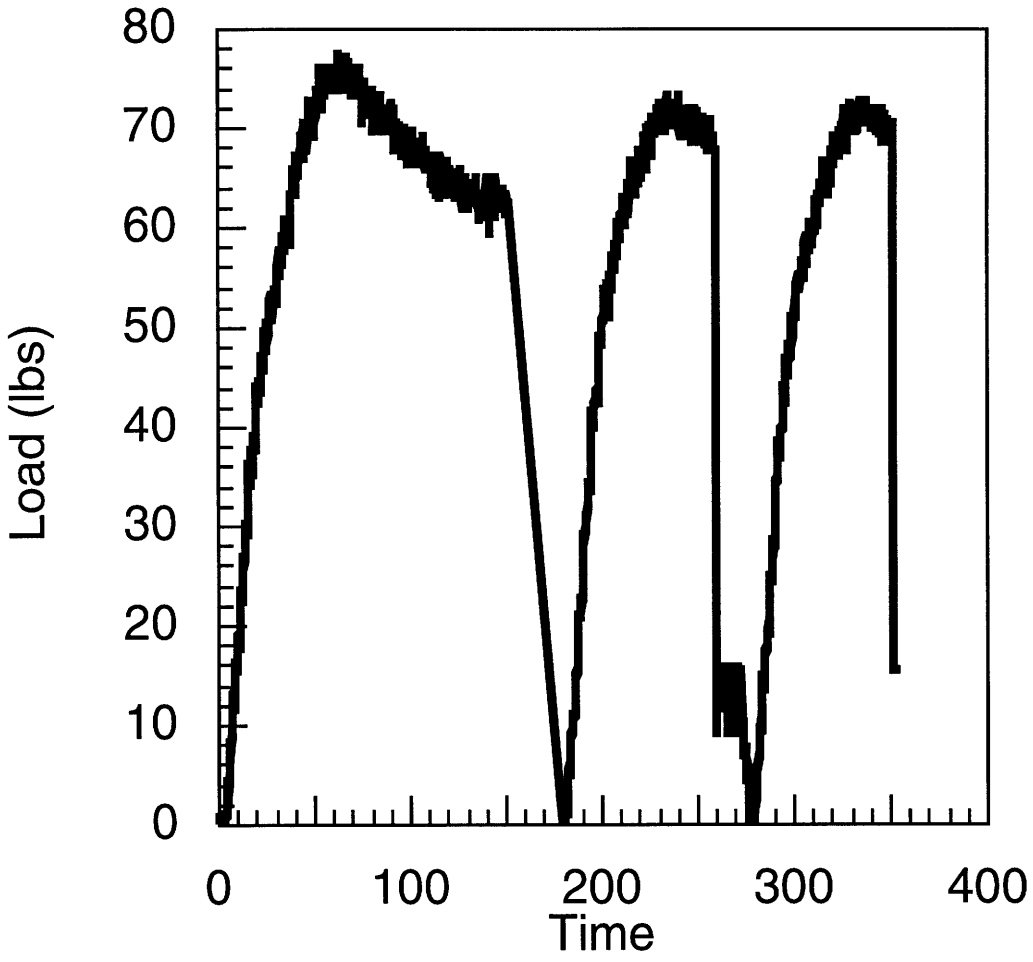


**Figure 7.15: Buckling Load Response of Test Sample (Panel with an Aspect Ratio of One) That was Taken to Its Critical Buckling Load Multiple Times**

Figure 7.16 shows the buckling load response of a sample that had been taken to its critical buckling load twice. On the second load sequence, the panel was subjected to a greater applied displacement, thus increasing its out of plane deflection, until damage was introduced into the panel. The introduction of damage was detected by a loud cracking sound and the sudden drop in load. On the subsequent loading cycle, the sample was not able to carry as high a load due to the damage, and its effect on the specimen's stiffness. This suggests that the onset of damage is determined by the loads and deformations experienced in the post-buckling regime rather than the onset of buckling.

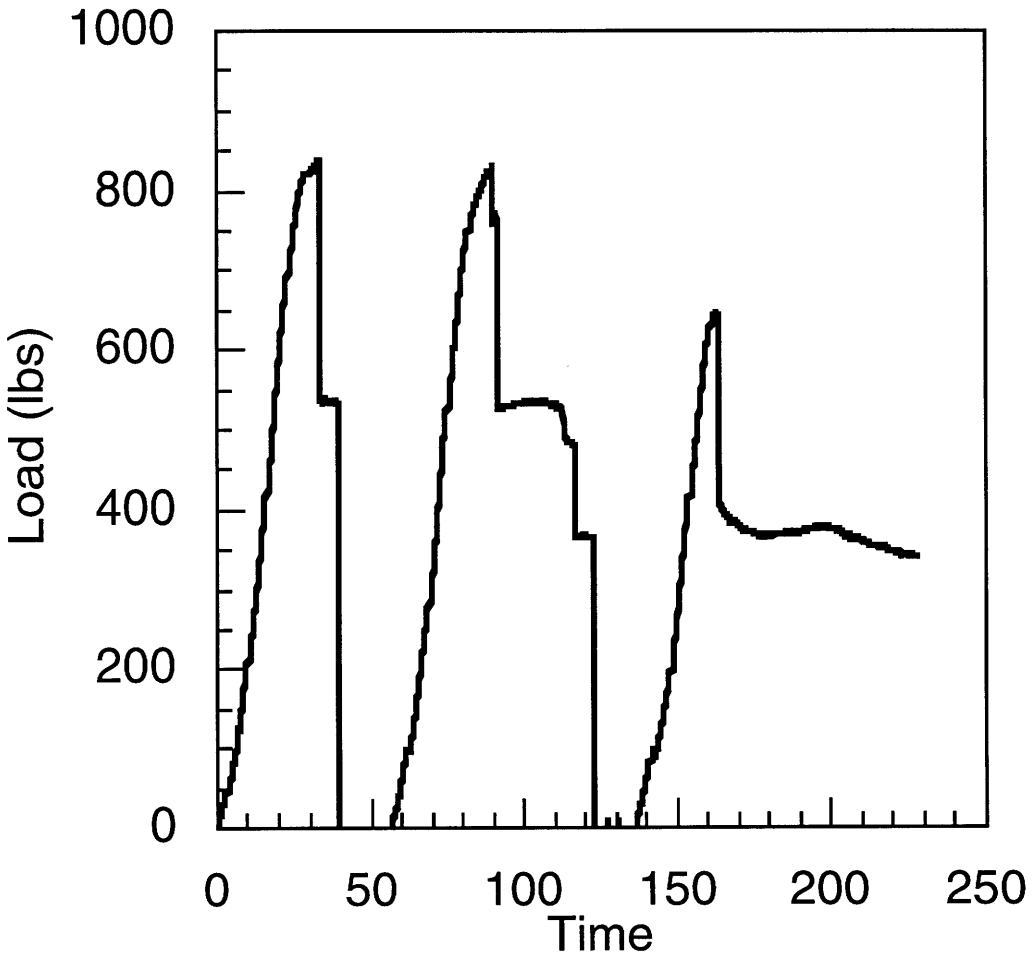


**Figure 7.16: Buckling Load Response of Test Sample That was Taken to Its Critical Buckling Load Multiple Times and Subjected to Damage**

By testing the air gun samples with the MTS compression machine, the loading response of the samples post air gun was determined. The post air gun samples demonstrated the same behavior as the original axial compressed samples. The following figure gives an example of the axial compression response of a baseline sample that had experienced an acceleration of 30,000g's (See Figure 7.17). The controlled axial compression tests showed an average critical buckling load of 568 pounds, which is in good agreement with this load-displacement data.

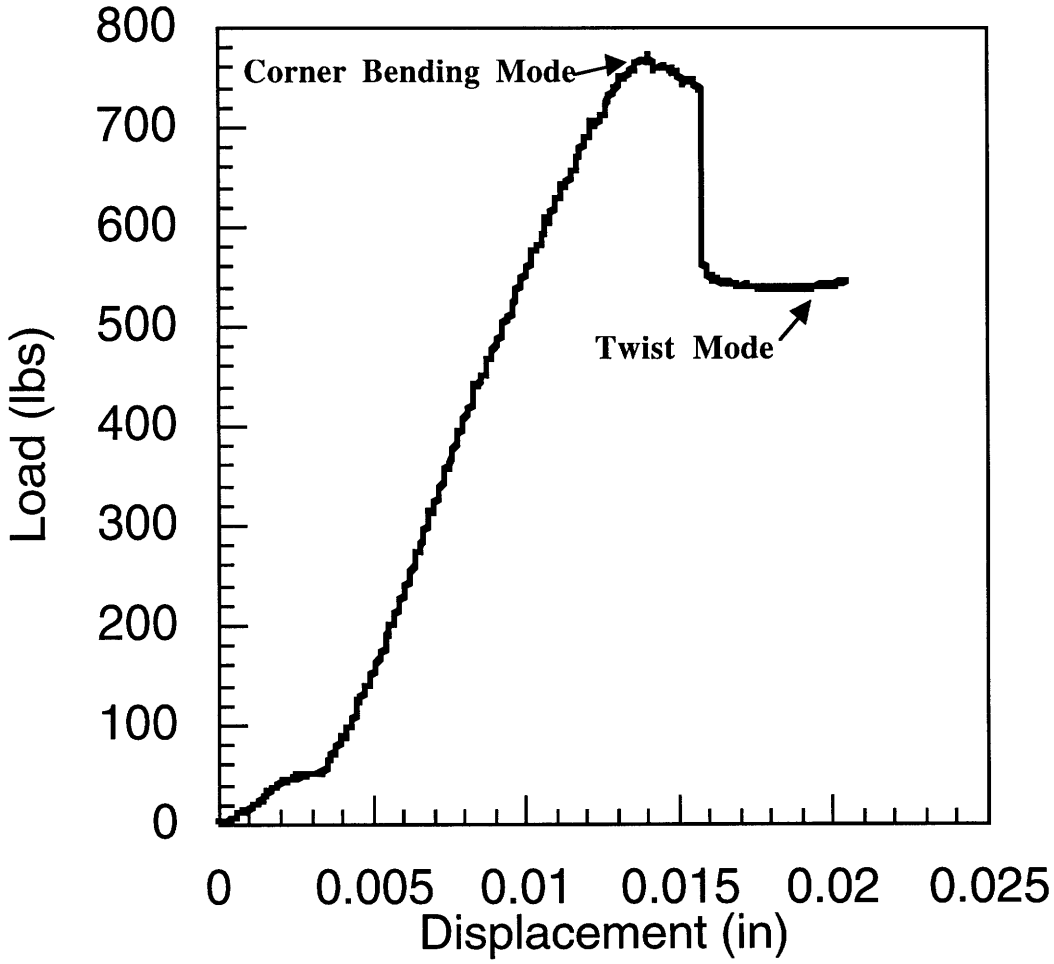


**Figure 7.17: Post-Air Gun Load-Displacement Curve for Baseline Panel**

## 7.3 Summary

This chapter presented the results of the finite element model and the experimental testing. The buckling response of all of the panel configurations were determined for both the finite element model and the axial compression tests. The air gun test showed that the composite samples were able to survive the high-g accelerations experienced in a launch environment. The results will be discussed in further detail in Chapter 8.

# CHAPTER 8

# DISCUSSION

This chapter presents a discussion of the results that were presented in Chapter 7. Section 8.1 compares the finite element model results and the controlled axial compression test results. Section 8.2 presents a discussion of the effect of lay-up, curvature, aspect ratio, and length of the composite sample on the critical buckling load. Section 8.3 discusses the results of the high-g testing performed at Picatinny Arsenal. Section 8.4 assesses whether the finite element model and controlled axial compression tests can be used as design tools.

## 8.1 Comparison of Finite Element Model to Axial Compression Tests

This section presents an overall comparison of the finite element results to the controlled axial compression test results. When investigating the buckling response of a structure, the two key aspects to study are the critical buckling load and the corresponding mode shape. For both the finite element model and the controlled axial compression tests, these two characteristics of the buckling response were obtained.

The results from the analytical and experimental work of Chapters 6 and 7 are presented in Figures 8.1 through 8.4. The figures compare the results of the finite element model to the controlled axial compression tests by individually investigating each key element: lay-up, curvature, aspect ratio, and length. For the finite element model, both the first and second buckling

mode responses are presented. The experimental results are presented for all observed mode shapes.

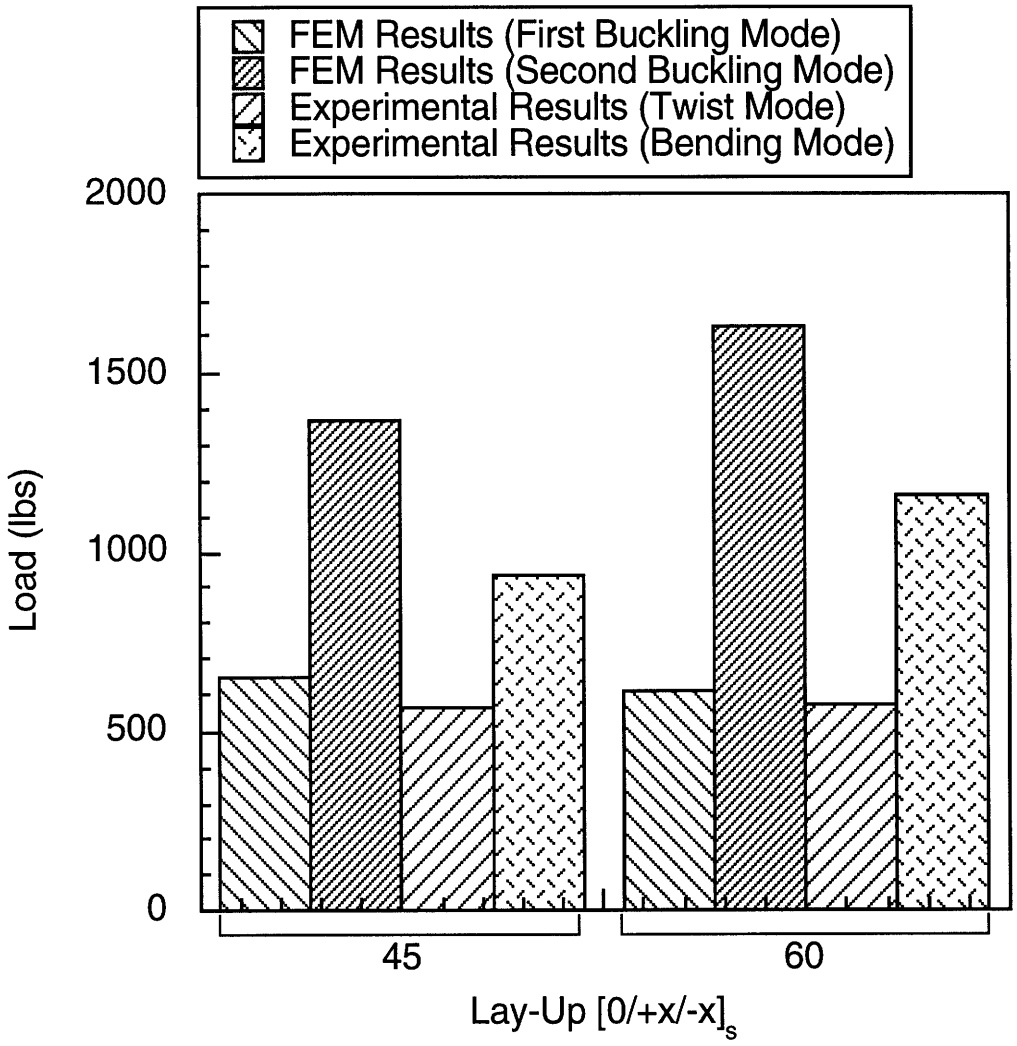


**Figure 8.1: Influence of Lay-Up on the Critical Buckling Load**

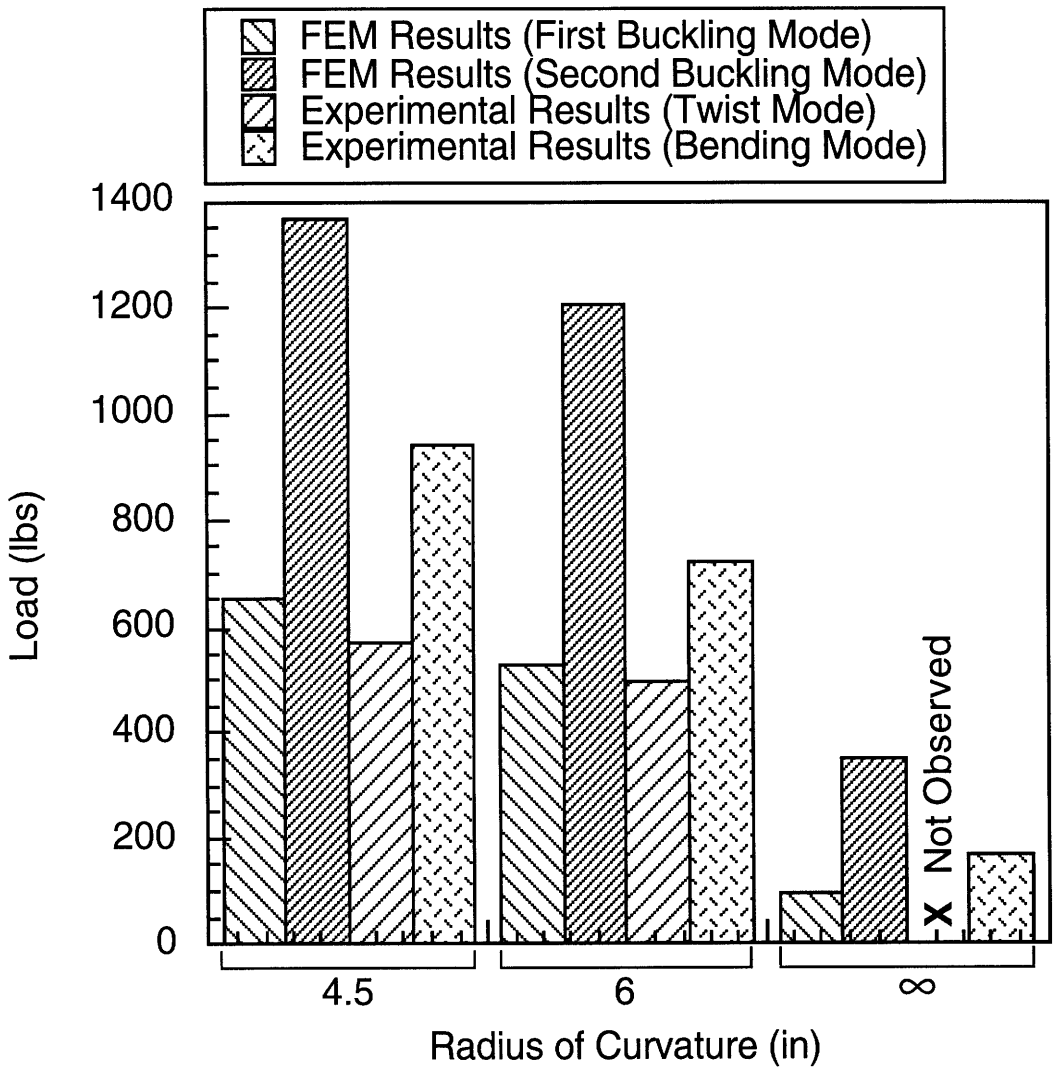


**Figure 8.2: Influence of Curvature on the Critical Buckling Load**

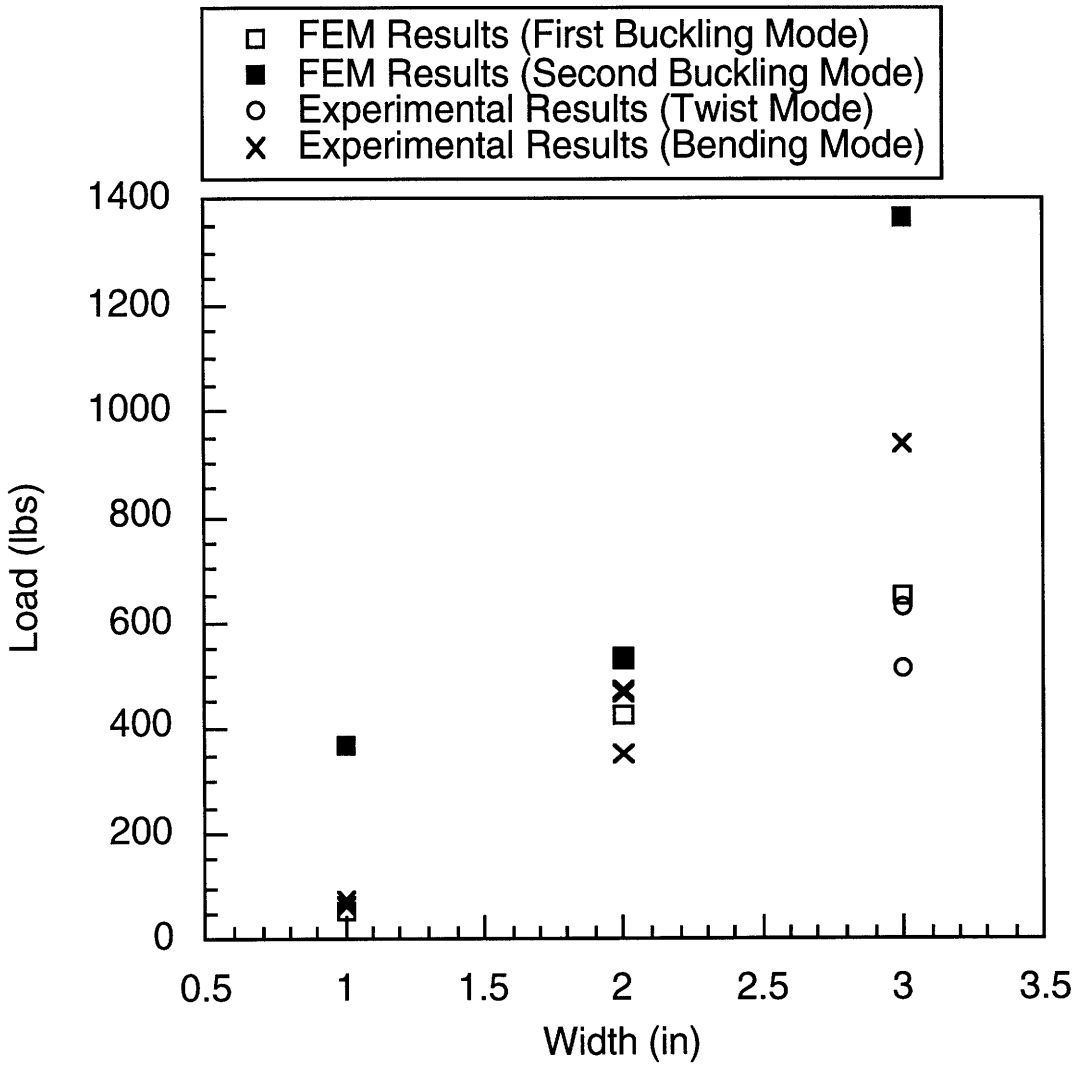


**Figure 8.3: Influence of Width on the Critical Buckling Load**

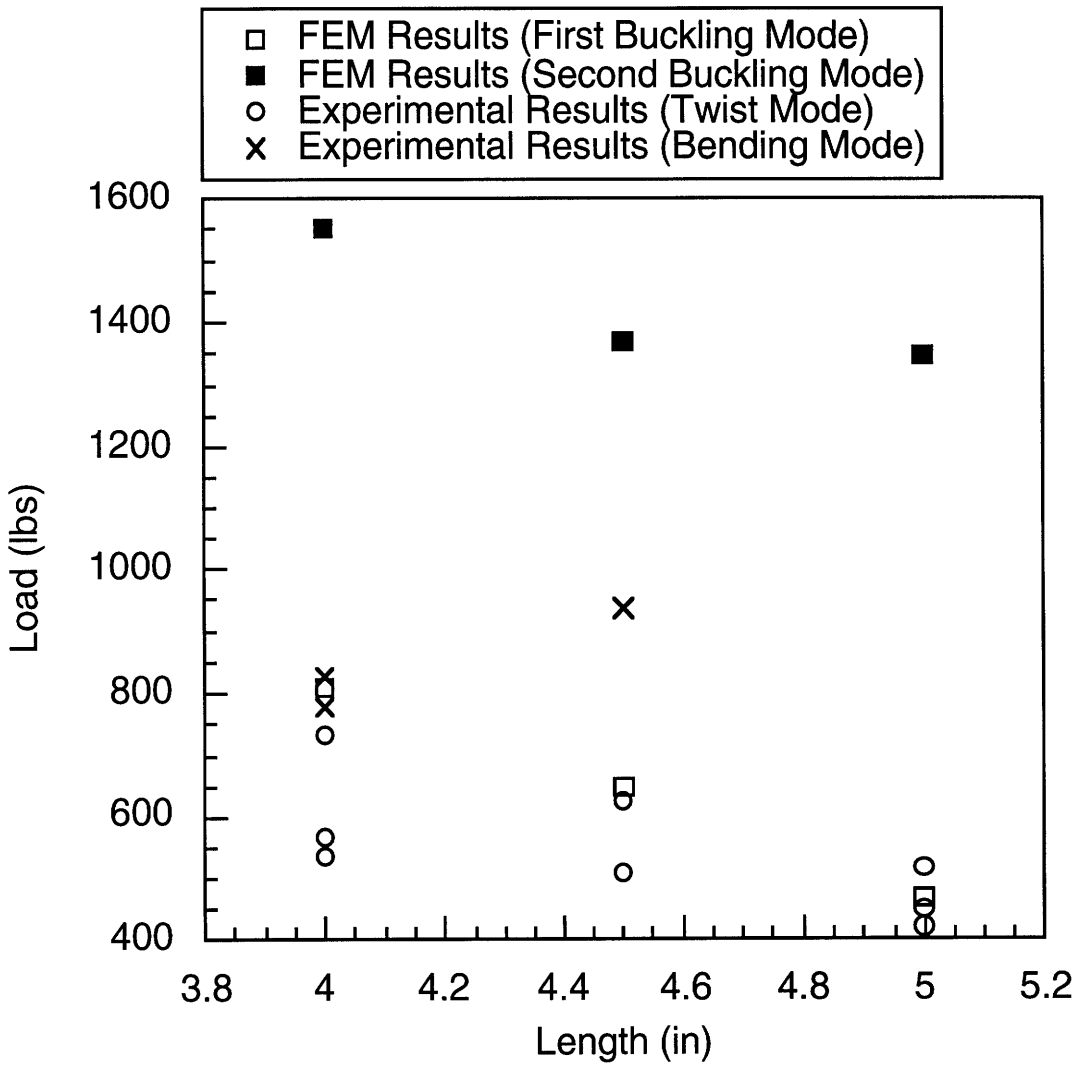


**Figure 8.4: Influence of Length on the Critical Buckling Load**

The following table summarizes the results for the critical buckling loads by comparing the average critical buckling load values predicted by the finite element modeling and those obtained through the experimental testing. Since some panels demonstrated two different mode shapes during testing, each of these mode shape values will be compared separately.

| Configuration | Finite Element (lbs) | | Experimental (lbs) | | % Difference | |
|---|---|---|---|---|---|---|
| | Bending | Twist | Bending | Twist | Bending | Twist |
| **Baseline** | 1367 | 649 | 936 | 568 | 32 | 12 |
| **Lay-Up** | | | | | | |
| Variation #1 | 1635 | 606 | 1156 | 572 | 29 | 5 |
| **Curvature** | | | | | | |
| Variation #1 | 1204 | 527 | 721 | 496 | 40 | 5 |
| Variation #2 | 93 | 351 | 170 | - | 82 | - |
| **Aspect Ratio** | | | | | | |
| Variation #1 | 533 | 665 | 431 | - | 19 | - |
| Variation #2 | 53 | 363 | 67 | - | 25 | - |
| **Length** | | | | | | |
| Variation #1 | 1550 | 810 | 802 | 613 | 48 | 24 |
| Variation #2 | 1348 | 469 | - | 463 | - | 1 |

**Table 8.1: Comparison of Critical Buckling Loads Between the Finite Element Model and Axial Compression Tests**

In addition to the critical buckling load, the other key aspect investigated was the buckling mode of the deformed composite panels. In two cases, the flat plate and the panel with an aspect ratio of one, both the model and all of the tested samples demonstrated the bending mode shape. Also, in the case of the panel with a length of four inches, both the model and all of the

tested samples went into the twist mode shape. However, in the case of the panel with an aspect ratio of two, the model predicted a twist mode behavior whereas all of the panels that were tested went into the bending mode shape. In all of the other cases, the model predicted the panels to exhibit the twist mode shape behavior. However, the test results showed that most of the panels originally went into a corner bending mode shape and then suddenly snapped into the twist mode shape. In this case, the behavior is believed to be due to the boundary conditions that were applied to the test article. In the finite element model, the composite panels were given one clamped boundary and three free edges. However, due to the test set up, these exact conditions could not be obtained. One of the edges was given a clamped boundary condition by using the designed test fixture and fixing the edge in wax. The opposite edge of the sample was in contact with the platen that was loading the structure and thus did not have a free boundary condition. Instead, the boundary condition would perhaps more properly be modeled as a frictional roller. It appears that as the load was increasing, the boundary condition was forcing the structure to deform in a corner bending mode, which is the second mode of the structure as predicted by the finite element model. However, the panels never appeared to reach the critical buckling load of the second mode which is why the experimental values are much lower than the finite element model predictions. This is due to the fact that when the energy in the system was great enough to overcome the friction of the platen surface, the system would suddenly twist into its lower, first mode shape. Therefore when investigating the critical buckling load and the mode shapes, it is necessary to note that the boundary conditions can play a crucial role. This is generally true of experimental investigations of buckling. Since in the actual gun launch, the test article will have a free boundary condition, that is the condition that is

most crucial for this study. Therefore, the crucial response that should be investigated is the critical buckling load and mode shape associated with the first buckling mode response.

When specifically investigating the first buckling mode response, the finite element model and the controlled axial compression tests are in relatively good agreement. The model predicts the correct mode shapes for all of the panels, except for the case of the panel with an aspect ratio of two. Also when investigating the critical buckling load associated with the first buckling mode, the model shows moderate agreement with the experimental results. All of the cases agree within twenty-five percent, except for the case of the flat plate. It should be noted that in general, the experimental results show a critical buckling load lower than that predicted by the finite element model. This is to be expected given imperfections in the samples and the less than ideal boundary conditions.

## 8.2 Influence of Lay-Up, Curvature, Aspect Ratio, and Length on the Critical Buckling Load

This section will use the previous results of both the finite element model and the axial compression tests to characterize the buckling behavior of the different panel configurations. Specifically, the data for the different lay-ups, curvatures, aspect ratios, and lengths will be isolated and studied individually. This discussion will be limited to the first buckling mode response since this has been recognized as the critical response of the composite panels.

The results were previously shown in Figures 8.1 through 8.4. In each case, three variations are investigated, except in the case of lay-up where there were only two variations. For each of the key variables, the general

trend of its effect on the critical buckling load can be determined. In each case, the finite element and experimental results show the same general trends. In the case of lay-up, there is not a significant difference between the two variations. However, the $[0/+45/-45]_s$ degree angle plies have a slightly higher critical buckling load than the $[0/+60/-60]_s$ degree angle plies (See Figure 8.1). The effect that curvature has on the critical buckling load can be seen in Figure 8.2. An increase in the radius of curvature leads to a decrease in the critical buckling load. The relation appears to asymptotically approach the limiting case of a flat plate, which has an infinite radius of curvature. For the investigation of the influence of the aspect ratio, the length of the plates were held at a constant length. Therefore, the aspect ratio can also be represented as a change in width. In this case, the data shows that an increase in the width, and therefore an increase in the aspect ratio, results in an increase in the critical buckling load (See Figure 8.3). The last condition that was investigated was the length of the panel (See Figure 8.4). The results show that an increase in the length leads to a decrease in the critical buckling load.

## 8.3 Discussion of Picatinny Arsenal Test Results

This section will discuss the results of the air gun tests and shock table tests performed at Picatinny Arsenal. A general discussion will be presented, followed by a discussion of a dynamic analysis that was performed in order to better understand the results of the high-g tests.

### 8.3.1 General Results Discussion

The results of the testing at Picatinny Arsenal showed that all of the samples survived the high-g tests. There was no visual damage to any of the samples and all of the samples remained in their original undeformed state.

Also, the subsequent end loading tests of the specimens showed that the samples did not experience any internal damage. Experiments performed after the high-g tests showed that the samples had the same load carrying capability and buckling response as samples that had not been tested in the high-g environment.

Although the model predicted that the samples would buckle, there is no way to tell exactly what happened to the samples in the high-g tests. From the data obtained through the finite element model and the controlled axial compression tests, it is expected that the samples did buckle under the high-g loads. As seen in the axial compression tests, it is believed that the panels behaved elastically. The hypothesis is that the panels did buckle under the high acceleration loads. However, once the load was removed, the panels returned to their original undeformed state.

Also due to the way the samples were packaged in the test canisters, it is possible that the canister wall prevented the sample from buckling or forced the sample into a higher mode, which would have a larger critical buckling load value. The axial compression tests showed that the samples could have a deflection as great as 0.5 inches without experiencing damage. In the five-inch air gun canister, the clearance between the composite sample and the canister wall was approximately 0.125 inches. In the 155-millimeter air gun, the clearance was approximately 0.55 inches. Therefore, in both cases, it would be possible for the canister wall to prevent the deformations levels from reaching a state where the panels would be permanently damaged.

Further testing is required to verify this speculation. If this does prove to be the mechanism by which the samples survived the high-g environment, it provides further justification for the use of composites. The high strain to

failure of composite laminates provides an increased survivability in the high-g environment.

### 8.3.2 Dynamic Analysis

In an attempt to better understand what exactly happened to the samples in the high-g test, the dynamics of the problem were studied. Initially it was thought that since the loading is dynamic, the problem should be analyzed by including the dynamics of the structure. In this sense, the load would be treated as a time dependent quantity, instead of as a quasi-static load. However, after an initial investigation, it was determined that the entire structure should be experiencing the peak load and therefore the problem could be studied from a static point of view. This investigation was performed by investigating the longitudinal wave propagation speed in the composite material and by looking at the natural period associated with the panels and the acceleration load. The wave propagation speed in the composite material is approximately 29,900 ft/sec. Therefore, by taking the size of the panel into account and looking at the acceleration profile, the pulse time is such that it allows for the entire structure to be subjected to load. The natural frequencies of the panel configurations were also obtained using ABAQUS™. The natural time period for all of the panel configurations are several orders of magnitude lower than the time period of the acceleration profiles. The time periods associated with the first mode of the panel configurations vary between 1.4e-4 milliseconds for the four inch long panel and 1.59e-3 milliseconds for the flat plate. Whereas the 5-inch air gun has a time period of approximately 3 milliseconds and the 155-millimeter air gun has a time period of approximately 9 milliseconds. This again supports the conclusion that the entire structure should be experiencing the maximum load given by the peak acceleration.

Therefore, these findings support the use of a static analysis to determine the buckling response of the panels to the high-g environment.

## 8.4 Design Tools for High-G Loading

The finite element model and controlled axial compression tests appear to offer a conservative design tool for curved composite panels under high-g loading. Although the design tools offer a conservative estimate of the failure load, the design tools do not capture the exact behavior of the composite panels under high-g loading. Therefore, since the exact behavior of the composites in the high-g tests is unknown, the design tool should be used with some caution.

# CHAPTER 9

# CONCLUSIONS AND RECOMMENDATIONS FOR FUTURE WORK

The work conducted herein investigated the use of composites within the WASP wing system design by studying the buckling behavior of curved composite panels under high-g loading. This chapter presents the conclusions that can be drawn from the previously presented work and makes recommendations for future work.

## 9.1 Conclusions

A finite element model was developed and experimental tests were performed to better understand the behavior of composite panels in a high-g, gun launch environment. The finite element model was developed as a design tool to model the original WASP wing as a constant thickness curved panel and to predict the buckling response of the panels. The results of the finite element model showed good agreement with the controlled axial compression tests. The finite element tool accurately predicted the buckling mode shapes of the panels. However, the design tool was only moderately accurate in predicting the critical buckling loads of the panels. In most cases, the model over-estimated the critical buckling load.

The experimental phase of this work used both controlled axial compression tests and high-g tests to determine the buckling response of composite panels. The buckling response, including mode shapes and critical

loads, was determined for the controlled axial compression tests. Also through the controlled axial compression tests, the elastic response of the composite panels was observed. Though the panels would buckle under the loading, as soon as the load was released, the panels would return to their original undeformed shape. The panels could also be reloaded multiple times and they would not show any loss in load carrying capability unless they experienced permanent damage, caused by fibers breaking. The high-g tests demonstrated that composite panels are a viable option for structural components in a high-g, gun-launched environment. All of the samples survived the high-g tests and showed no signs of damage.

The finite element model and controlled axial compression tests demonstrated a conservative value for the critical buckling load of the panels under high-g loading. Although the finite element tool and controlled axial compression tests show good agreement with each other, they do not accurately capture the response of the composite panels in the high-g environment.

## 9.2 Recommendations for Future Work

In order to better understand the gun launch environment and be able to better design high-g structural components, additional analysis and experiments need to be performed. Future work should mainly be focused on determining what exactly happened to the samples that were tested in the high-g environment. This could involve performing more tests where the samples are better instrumented to help determine if the samples buckle under the high accelerations. This could include using such techniques as strain sensitive paint or high strain rate strain gauges. The tests should also ensure that the panels are not being supported by the canister walls. Also, more

modeling should be performed to investigate the behavior of the composites under a dynamic load. Although the initial investigation showed that the dynamics should not play a role in determining the critical buckling load for the accelerations investigated, further efforts should be taken to verify this, particularly for structures in post-buckling configurations.

Also, specific to the development of the WASP vehicle's wing system, there is future work that needs to be carried out in order to design a completely composite wing. This research has focused on studying composite panels that model the first wing section. In addition to this study, the hinges used to connect the airfoil sections will have to be studied. Work needs to be performed to determine how to manufacture the hinges and how to attach them to the wing airfoil sections. Also one of the main considerations for high-g survivability, as learned through the WASP Project, is the packaging system. The packaging system will have to be investigated for a new composite wing design. The wing system should also be investigated from a manufacturing point of view. The current research used hand lay-up pre-preg, but other methods such as resin transfer molding using a stitched pre-form should be investigated. The current research has looked at one key element in the design of a high-g survivable composite wing, but there are still many issues that need to be investigated.

# References

[1] Bernstein, J. System Design for a Rapid Response Autonomous Aerial Surveillance Vehicle. Massachusetts Institute of Technology. Cambridge, MA, USA, 1997.

[2] Burba, M. System Design and Communication Subsystem of an Innovative Projectile. Massachusetts Institute of Technology. Cambridge, MA, USA, 1997.

[3] Conklin, T. MIT/Draper Technology Development Partnership Project: Systems Analysis and On-Station Propulsion Subsystem. Massachusetts Institute of Technology. Cambridge, MA, USA, 1997.

[4] Hallam, C. MIT/Draper Technology Development Partnership Project: Aerodeceleration, Structures, and System Design of a High-G Rapid Response, Deployable Unmanned Aerial Vehicle. Massachusetts Institute of Technology. Cambridge, MA, USA, 1997.

[5] Iranzo-Grues, D. Rapid Response Surveillance System Design and Aerodynamic Modeling. Massachusetts Institute of Technology. Cambridge, MA, USA, 1997.

[6] Shook, G. MIT/Draper Technology Development Partnership Project: Design, Assembly, and Test of the Launch and Flight Support and Deployment System for a Gun Launched Reconnaissance Vehicle. Massachusetts Institute of Technology. Cambridge, MA, USA, 1998.

[7] Katch, S. Concept Development, Mechanical Design, Manufacturing and Experimental Testing for a Cannon-Launched Reconnaissance Vehicle. Massachusetts Institute of Technology. Cambridge, MA, USA, 1998.

[8] Trinh, T. Investigation of Visual Cueing Aids for UAV Targetting for Real-Time Waypoint Re-Allocation. Massachusetts Institute of Technology. Cambridge, MA, USA, 1998.

[9] Gavrilets, V. Avionics System Development for Small Unmanned Aircraft. Massachusetts Institute of Technology. Cambridge, MA, USA, 1998.

[10] Casiez, T. Compact, High-G, High Efficiency Folding Wing for a Cannon Launched Reconnaissance vehicle. Massachusetts Institute of Technology. Cambridge, MA, USA, 1998.

[11] Hauss, J-M. Design of an Unmanned Aerial Vehicle. Massachusetts Institute of Technology. Cambridge, MA, USA, 1998.

[12] Chiu, H. Wide Area Surveillance Projectile Deployment Sequence. Massachusetts Institute of Technology. Cambridge, MA, USA, 1998.

[13] Primex Technologies, Inc. Annual Report. 1999.

[14] Bovais, C.S., M.E. Havat, and P.L. Toot. "Flight Testing with Sub-scale Remotely Piloted Drop Model." AIAA (1992): 92-4079.

[15] Airset. Computer software. M. Drela, Massachusetts Institute of Technology.

[16] Timoshenko, S., and J.N. Goodier. Theory of Elasticity. A McGraw-Hill Classic Textbook Reissue. 3rd ed. New York: McGraw-Hill Book Company, Inc., 1987.

[17] Timoshenko, S., and S. Woinowsky-Krieger. Theory of Plates and Shells. A McGraw-Hill Classic Textbook Reissue. 2nd ed. New York: McGraw-Hill Book Company, Inc., 1987.

[18] Bazant, A.P. and Luigi Cedolin. Stability of Structures. The Oxford Engineering Science Series. Ed. J.M. Brady, et al. New York: Oxford University Press, Inc., 1991.

[19] Mallikarjuna, and T. Kant. "A Critical Review and Some Results of Recently Developed Refined Theories of Fiber-Reinforced Laminated Composites and Sandwiches." Composite Structures 23 (1993): 293-312.

[20] Jones, R. M. Mechanics of Composite Materials. Blacksburg, VA: Taylor & Francis, 1975.

[21] Barai, A., and S. Durvasula. "Vibration and Buckling of Hybrid Laminated Curved Panels." Composite Structures 21 (1992): 15-27.

[22] Aiello, M.A., and L. Ombres. "Maximum Buckling Loads for Unsymmetric Thin Hybrid Laminates Under In-Plane and Shear Forces." Composite Structures 36 (1996): 1-11.

[23] Sheinman, I. and Y. Reichman, "A Study of Buckling and Vibration of Laminated Shallow Curved Panels." International Journal of Solids and Structures 29 (1992): 1329-1338.

[24] Wilkins, D.J. "Compression Buckling Tests of Laminated Graphite-Epoxy Curved Panels." AIAA 13 (1975): 465-470.

[25] Kicher, T.P., and J.F. Mandell. "A Study of the Buckling of Laminated Composite Plates." AIAA 9 (1971): 605-613.

[26] Hutchinson, J.W. and B. Budiansky. "Dynamic Buckling Estimates." AIAA 4 (1966): 525-530.

[27] Budiansky, B., "Dynamic Buckling of Elastic Structures: Criteria and Estimates." Dynamic Stability of Structures, Proceedings of an International Conference. Evanston, Illinois, USA. 1965.

[28] Birman, V. "Problems of Dynamic Buckling of Antisymmetric Rectangular Laminates." Composite Structures 12 (1989): 1-15.

[29] Abramovich, H. and A. Grunwald. "Stability of Axially Impacted Composite Plates." Composite Structures 32 (1995): 151-158.

[30] Hibbitt, Karlsson & Sorensen, Inc. ABAQUS Theory Manual. Pawtucket, RI: Hibbitt, Karlsson & Sorensen, Inc., 1998.

[31] Cesnik, C., Professor at Massachusetts Institute of Technology. Meeting. 1999.

[32] Lagace, P. A., Brewer, J. C. , and Varnerin, C., "TELAC Manufacturing Course Notes." TELAC Report 88-4B, Massachusetts Institute of Technology, 1990.

[33] Wardle, B. Impact and Quasi-Static Response of Cylindrical Composite Shells. Massachusetts Institute of Technology. Cambridge, MA, USA. 1995.

# APPENDIX A

# ABAQUS CODE

ABAQUS™ Code for the Baseline Design

ABAQUS™ Version 5.8

Note: Comments are in bold type and enclosed by brackets ( )

Values are in SI units

```
*HEADING
SDRC I-DEAS ABAQUS FILE TRANSLATOR  02-Mar-99   19:08:02


*NODE, SYSTEM=R
(Defining the Nodes)
(Node Number, X-Coordinate, Y-Coordinate, Z-Coordinate)


*ELEMENT,TYPE=S4R,ELSET=E0000001
(Defining Shell Elements)
(Shell Element Number, Four Node Numbers That Make Up The Element)


*SHELL GENERAL SECTION,ELSET=E0000001,COMPOSITE
(Defining the Laminate)
(Ply Thickness, Material, Orientation Angle (degrees))
      (Note: The orientation angle is the angle of rotation from the
      x-axis of the material axis system. In this analysis, x-axis is shifted by 90
      degrees between the material axis system and the global part axis system)
.000127,,LAMINA, 90.
.000127,,LAMINA,-45.
.000127,,LAMINA, 45.
*** CENTER LINE
.000127,,LAMINA, 45.
.000127,,LAMINA,-45.
.000127,,LAMINA, 90.


*MATERIAL,NAME=LAMINA
(Defining Material Name)
```

*DENSITY
**(Defining Density (kg/m$^3$))**
1660.0

*ELASTIC,TYPE=LAMINA
**(Defining Material Properties)**
**($E_1$, $E_2$, $V_{12}$, $G_{12}$, $G_{13}$, $G_{23}$)**
138.0E9, 9.0E9, .33, 6.9E9, 6.9E9, 4.5E9

*NSET,NSET=CLAMP
**(Defining Group Of Nodes To Apply A Clamped Boundary Condition)**

*ELSET,ELSET=ELEM
**(Defining Group Of Elements That Will Be Given A Gravity Load)**

*STEP
**(Initializing Analysis)**

*BUCKLE
**(Buckling Calculation Command)**
**(Number of Eigenvalues, Number of Modes)**
3,3

*BOUNDARY
**(Defining Clamped Boundary Condition)**
CLAMP, ENCASTRE

*DLOAD
**(Defining Loading)**
**(Element Group, Type of Load, Magnitude of Load, Direction of Load (x, y, z))**
ELEM, GRAV, 147150.0,0.0,0.0,1.0

*RESTART,WRITE,OVERLAY
**(Rewriting The Restart File For Iterative Process)**

*EL PRINT
**(Writing Element Results To The Results File)**
S,

*NODE FILE, LAST MODE=3
**(Writing Eigenvalue To The Results File)**
U

*END STEP
**(Ending Analysis)**

*STEP
**(Initializing Analysis)**

*FREQUENCY
**(Natural Frequency Calculation)**
**(Number of Natural Frequencies)**
5

*BOUNDARY
**(Defining Clamped Boundary Condition)**
CLAMP, ENCASTRE

*RESTART,WRITE,OVERLAY
**(Rewriting The Restart File For Iterative Process)**

*EL PRINT
**(Writing Element Results To The Results File)**
S,

*NODE FILE
**(Writing Calculated Natural Frequencies To The Results File)**
U

*END STEP
**(Ending Analysis)**

# APPENDIX B

# LOAD-DISPLACEMENT CURVES

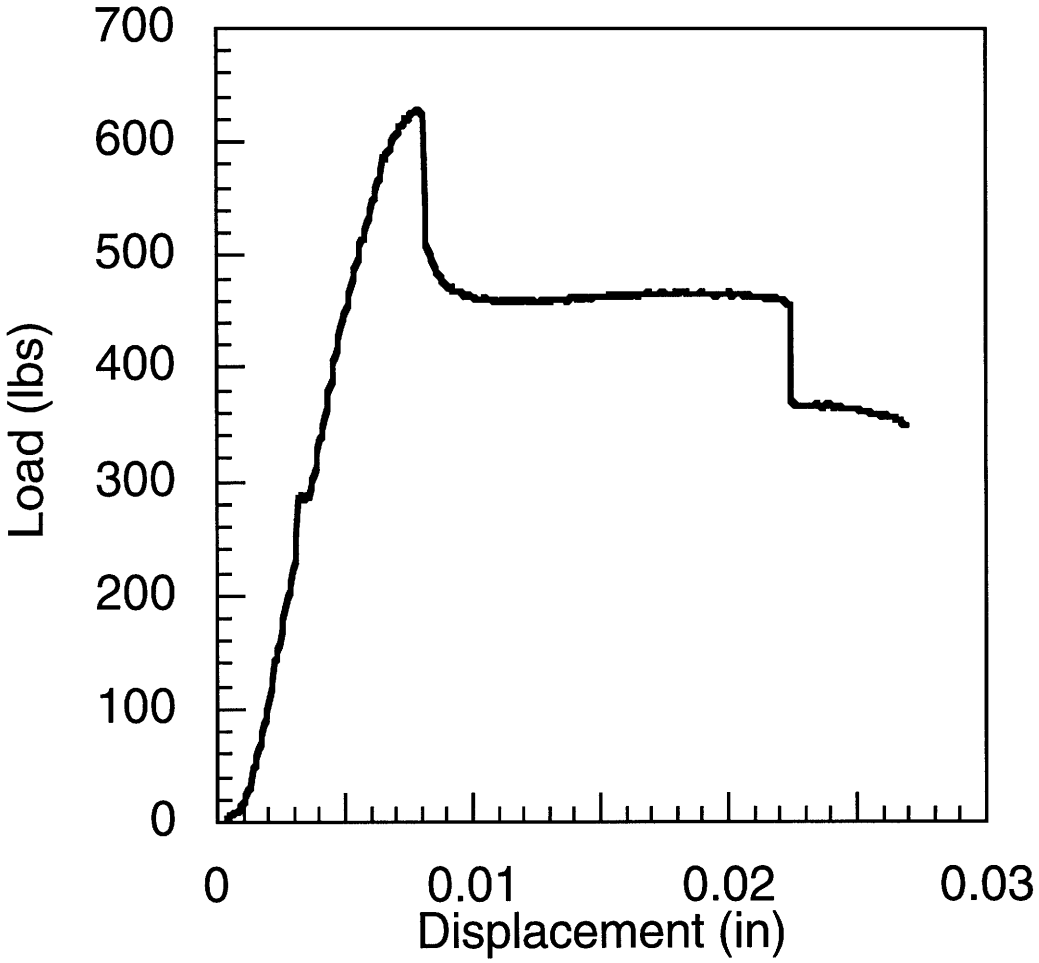


**Figure B.1: Load-Displacement Curve for Baseline Panel**

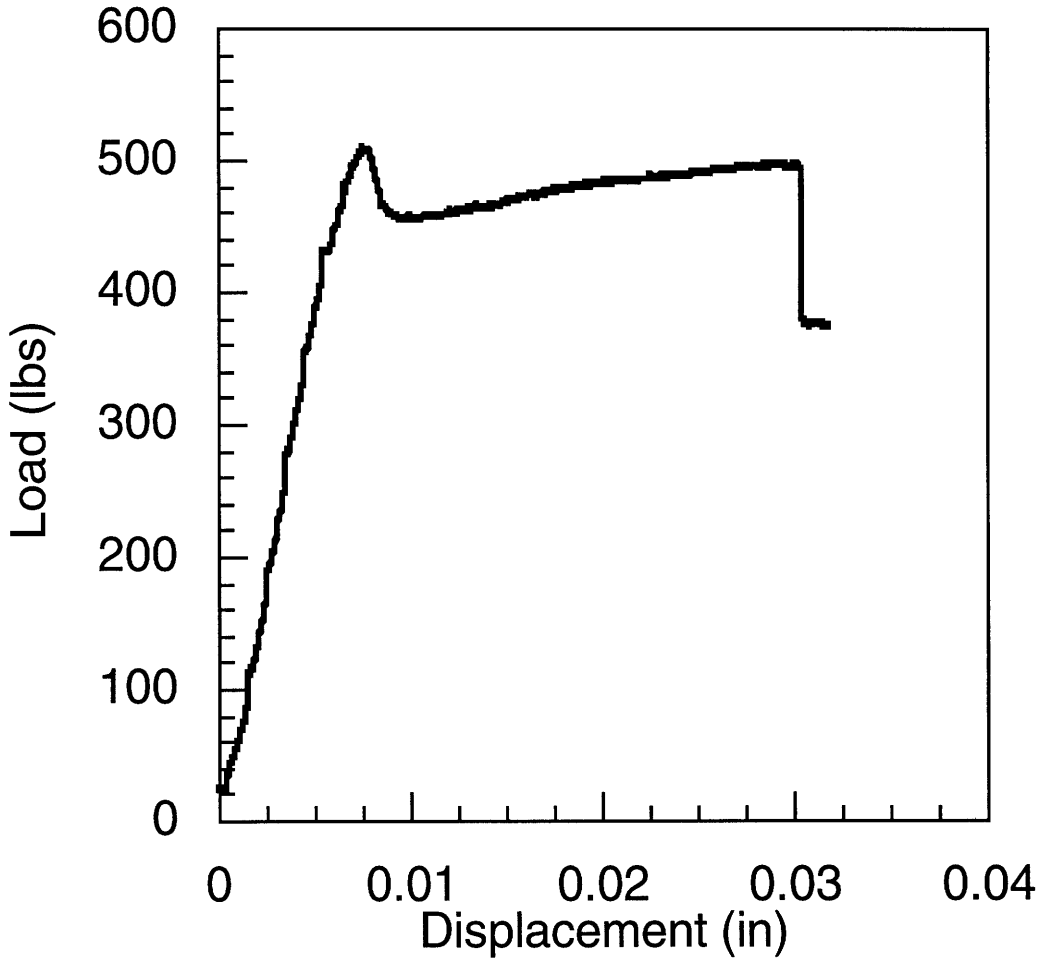


**Figure B.2: Load-Displacement Curve for Baseline Panel**

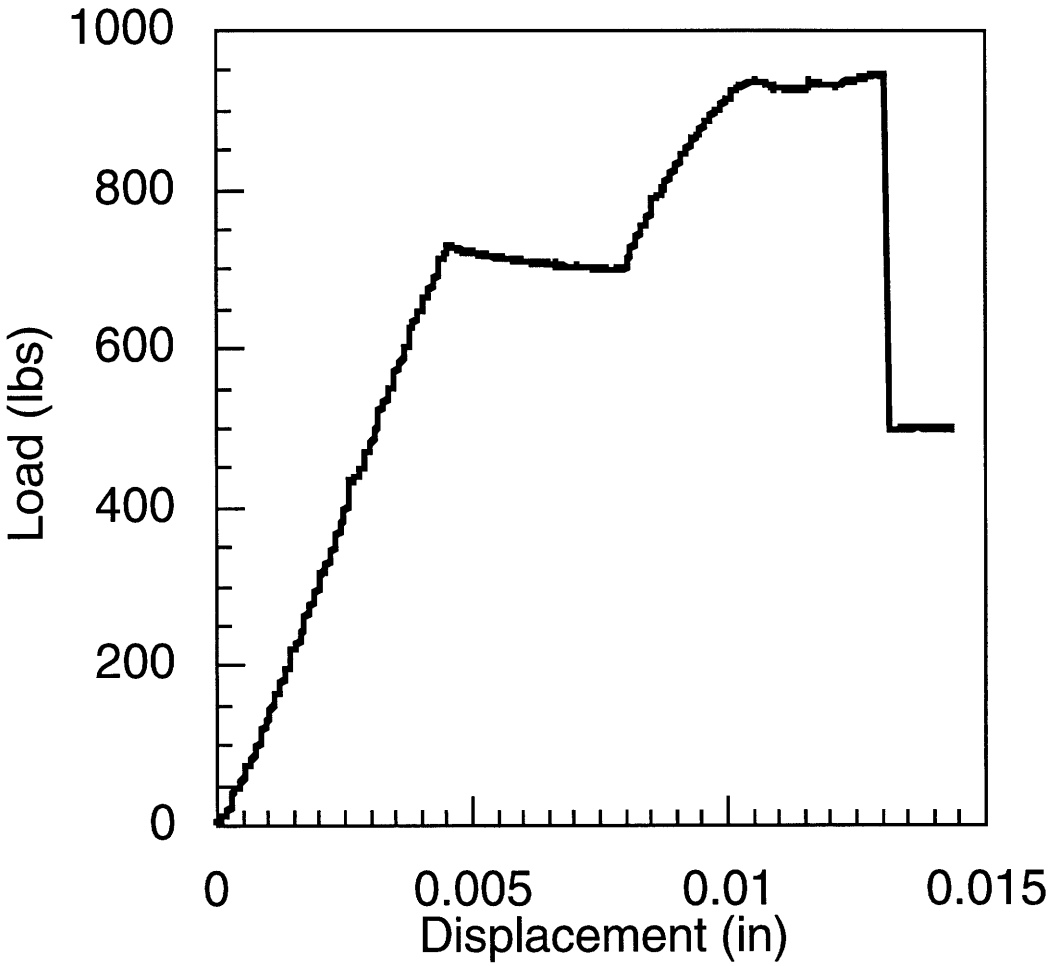


**Figure B.3: Load-Displacement Curve for Baseline Panel**

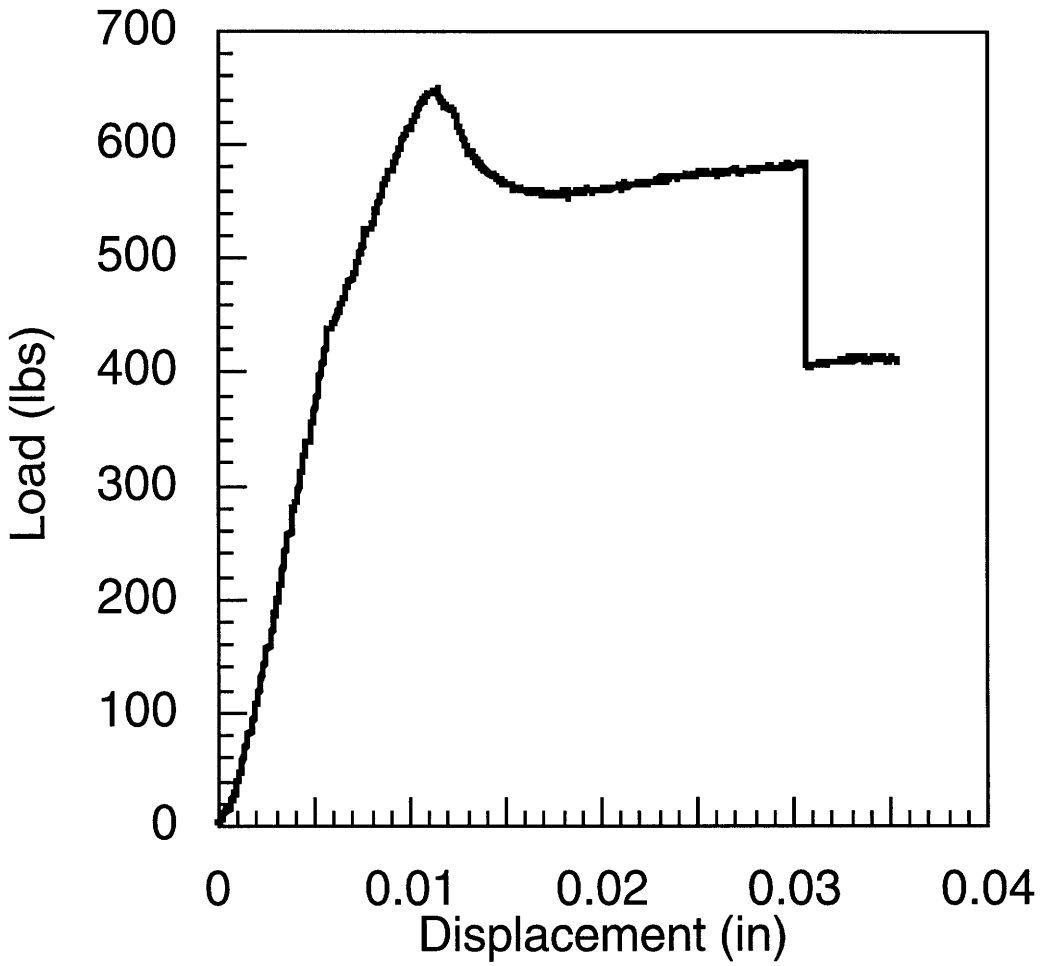


**Figure B.4: Load-Displacement Curve for $[0/+60/-60]_s$ Panel**

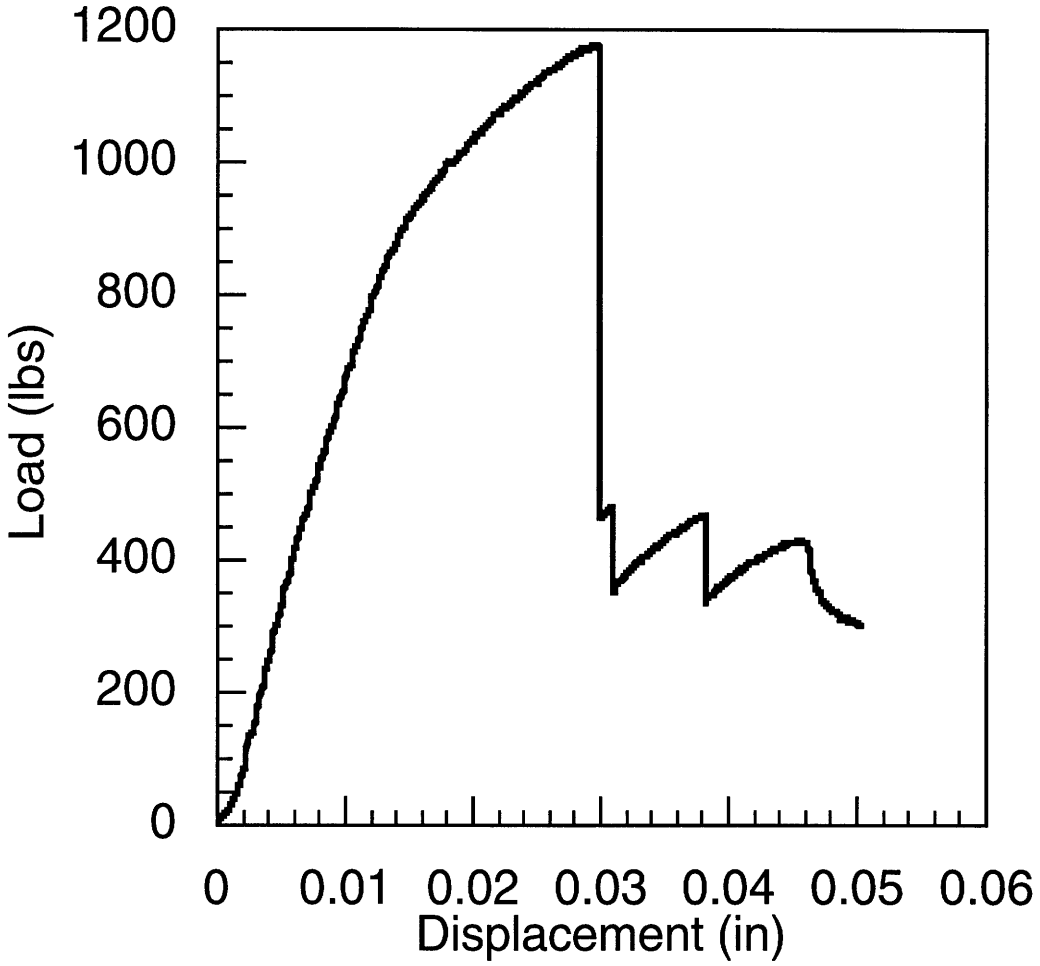


**Figure B.5: Load-Displacement Curve for $[0/+60/-60]_s$ Panel**

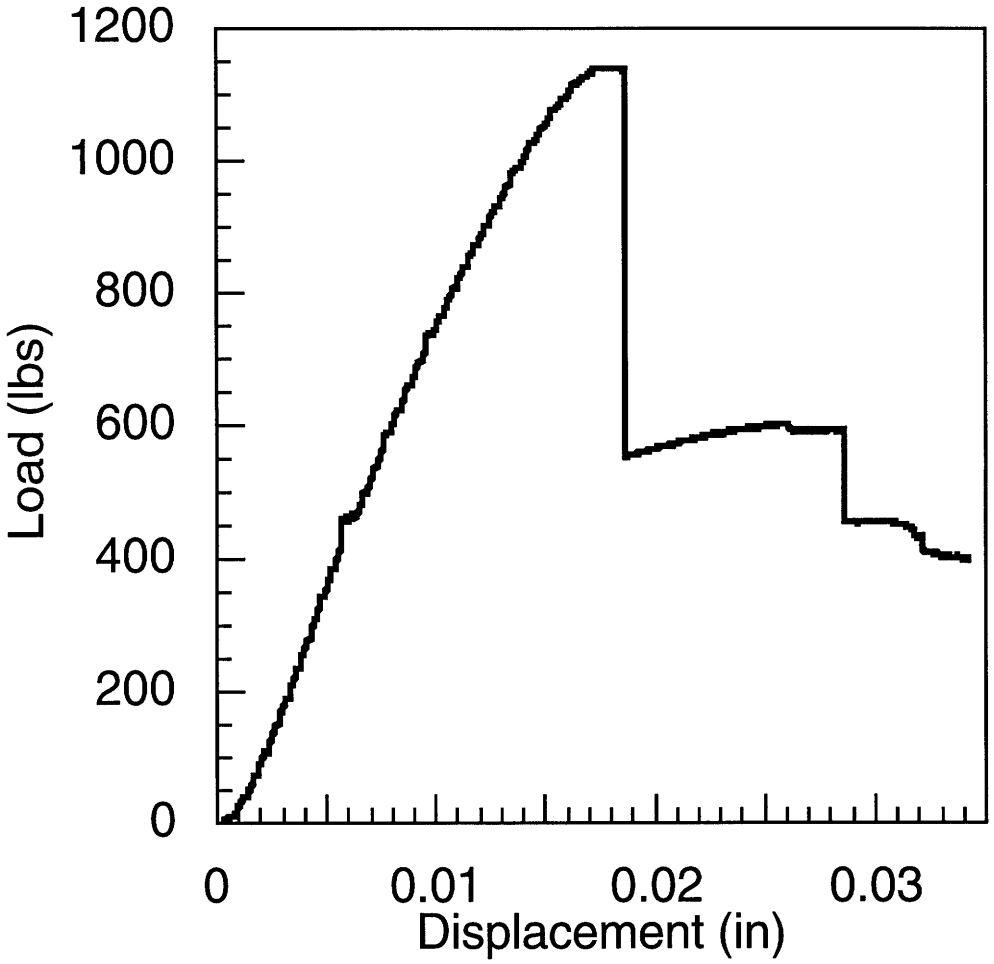


**Figure B.6: Load-Displacement Curve for $[0/+60/-60]_s$ Panel**

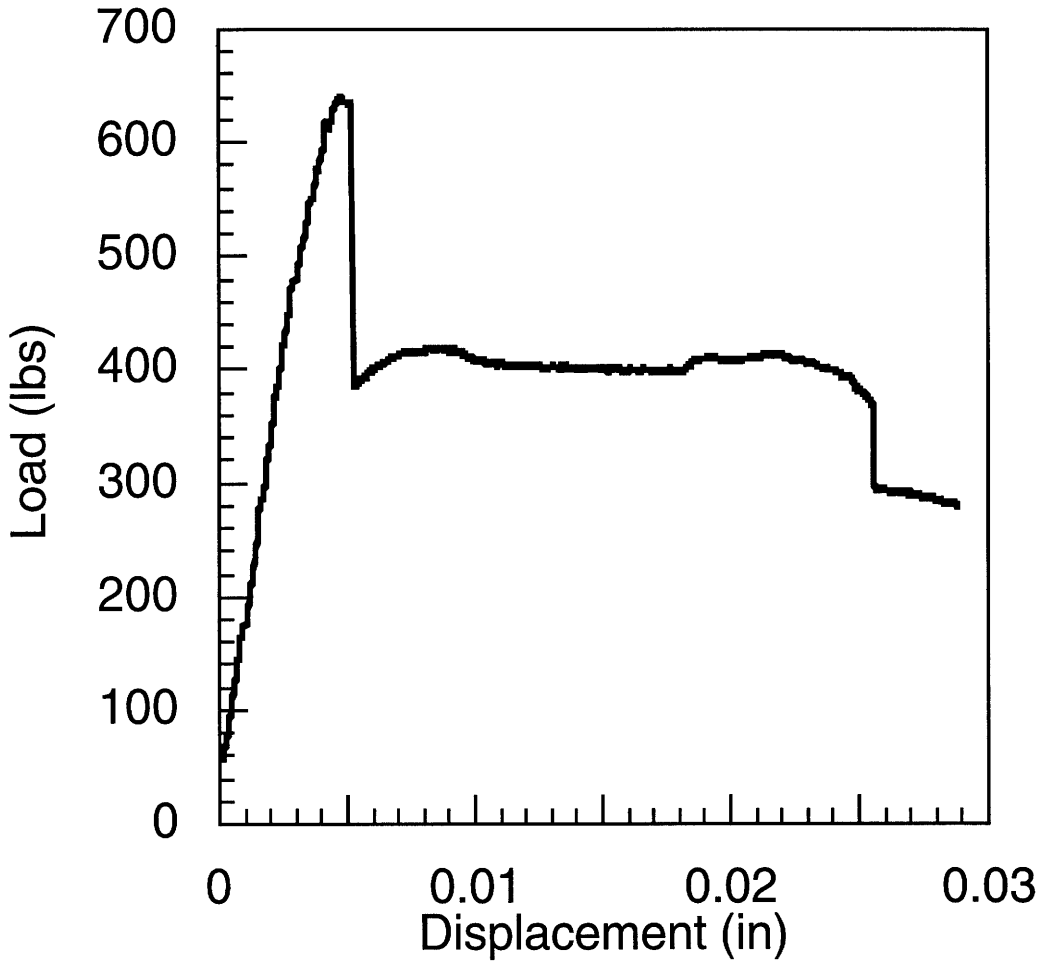


**Figure B.7: Load-Displacement Curve for Panel with 6 Inch Radius of Curvature**

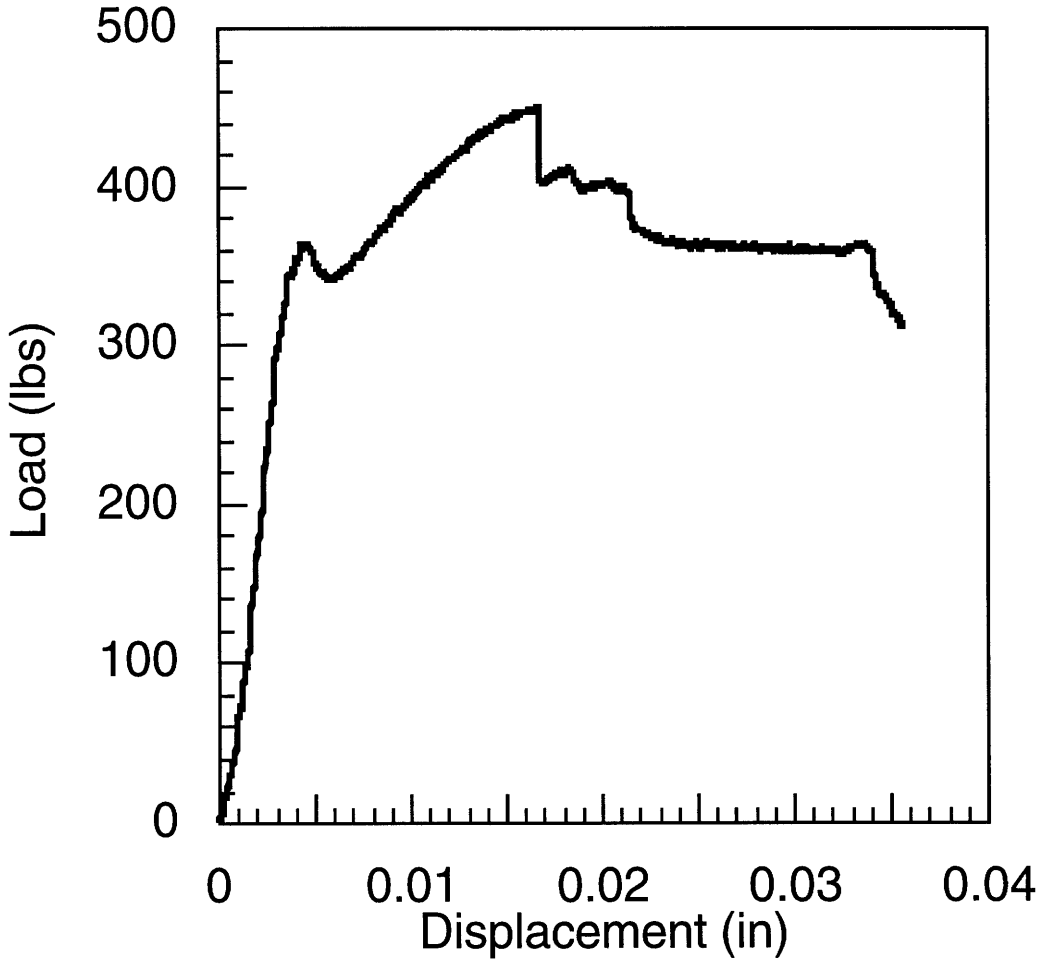


**Figure B.8: Load-Displacement Curve for Panel with 6 Inch Radius of Curvature**

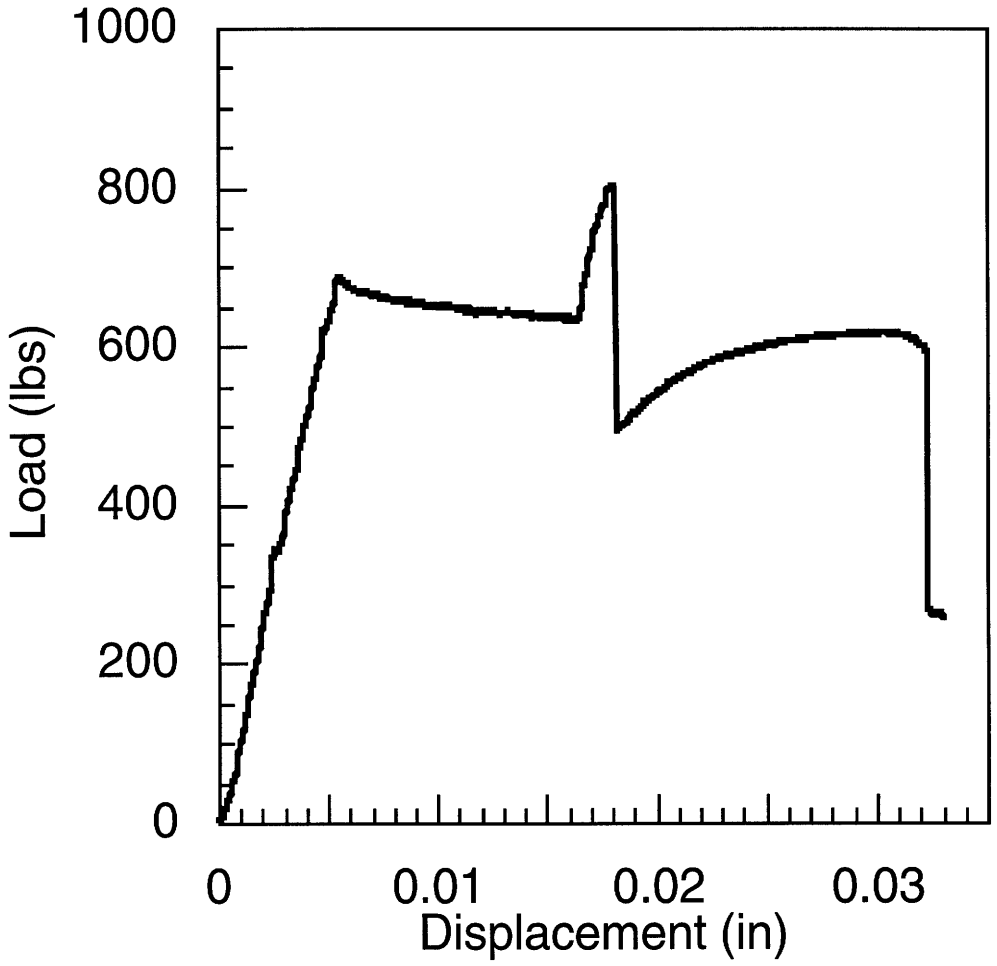


**Figure B.9: Load-Displacement Curve for Panel with 6 Inch Radius of Curvature**

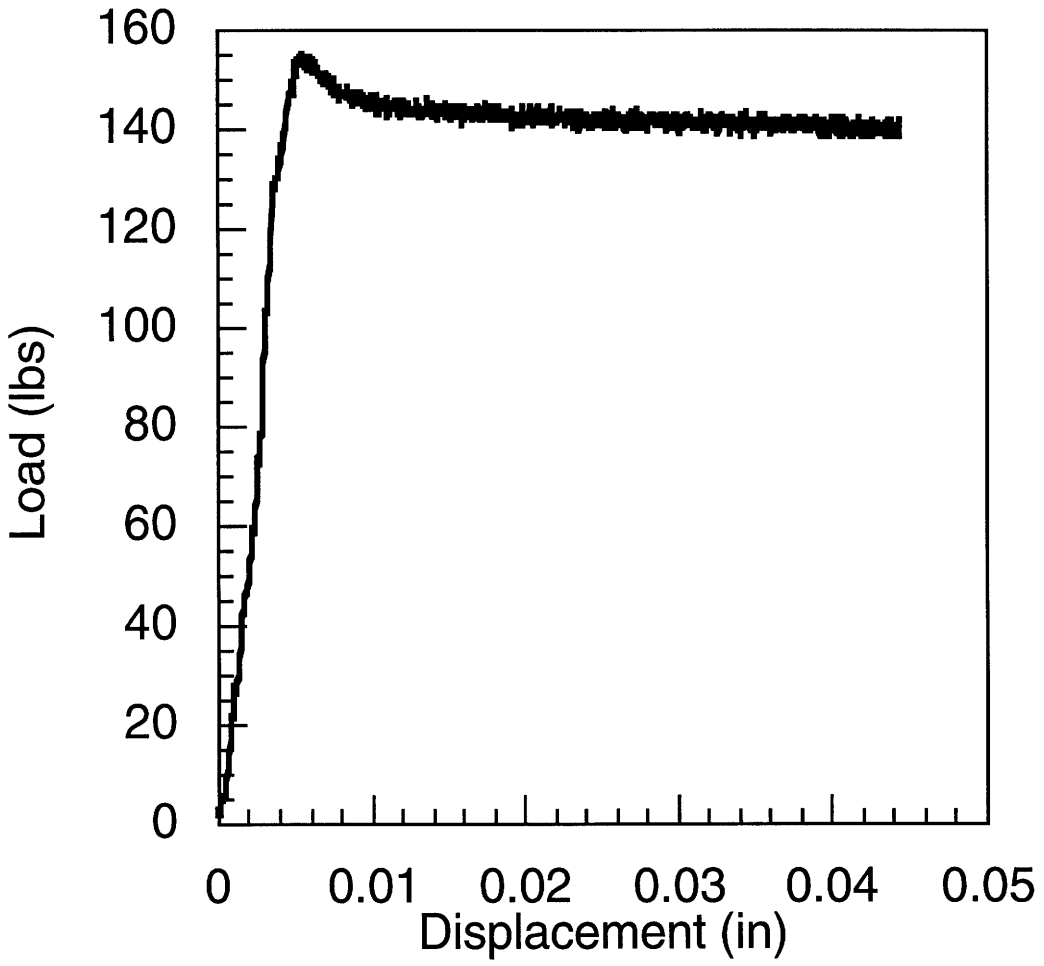


**Figure B.10: Load-Displacement Curve for Flat Plate**

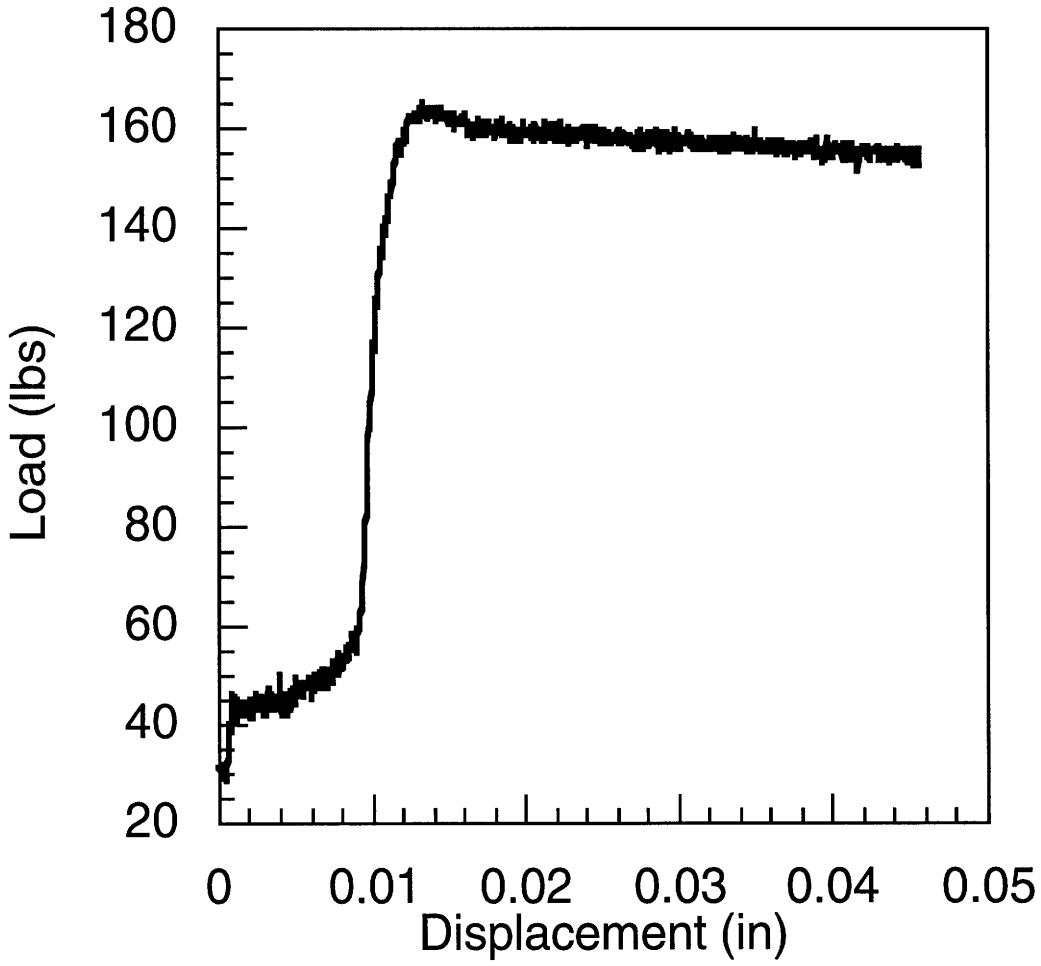


**Figure B.11: Load-Displacement Curve for Flat Plate**

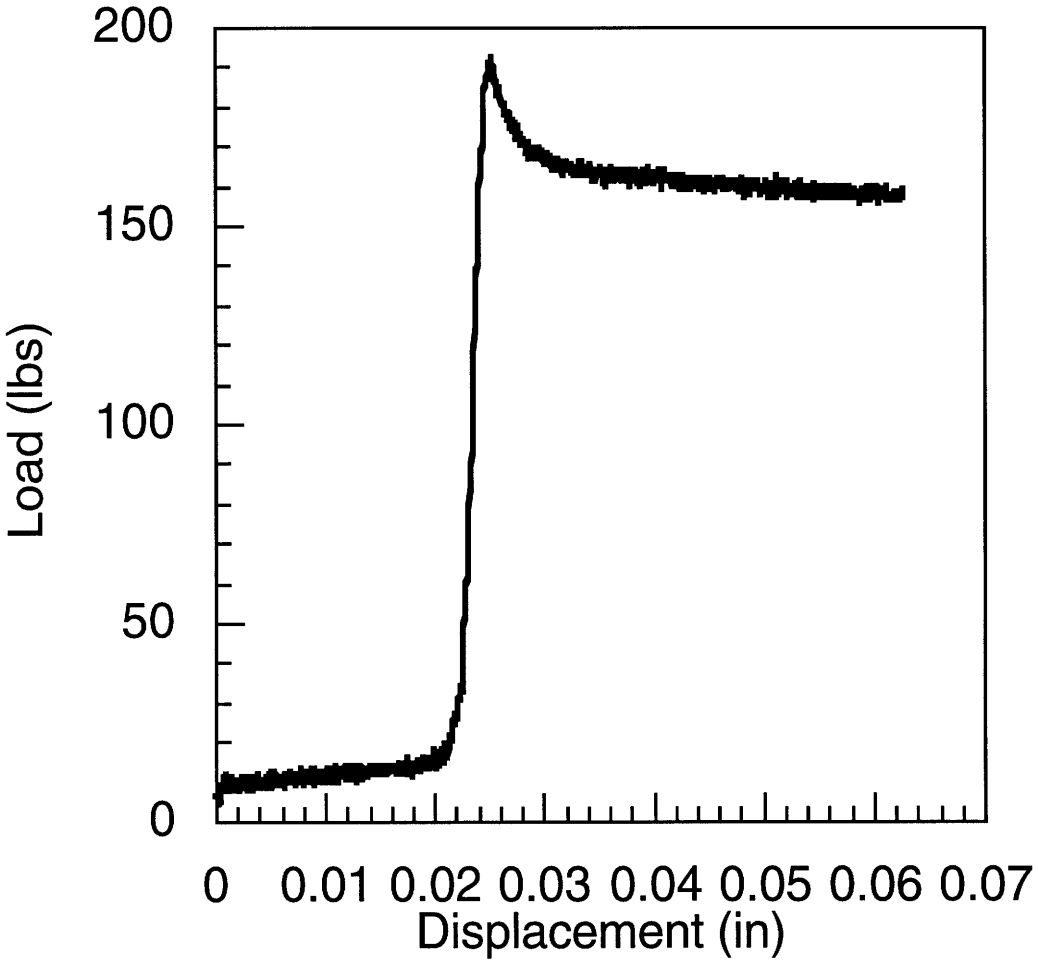


**Figure B.12: Load-Displacement Curve for Flat Plate**

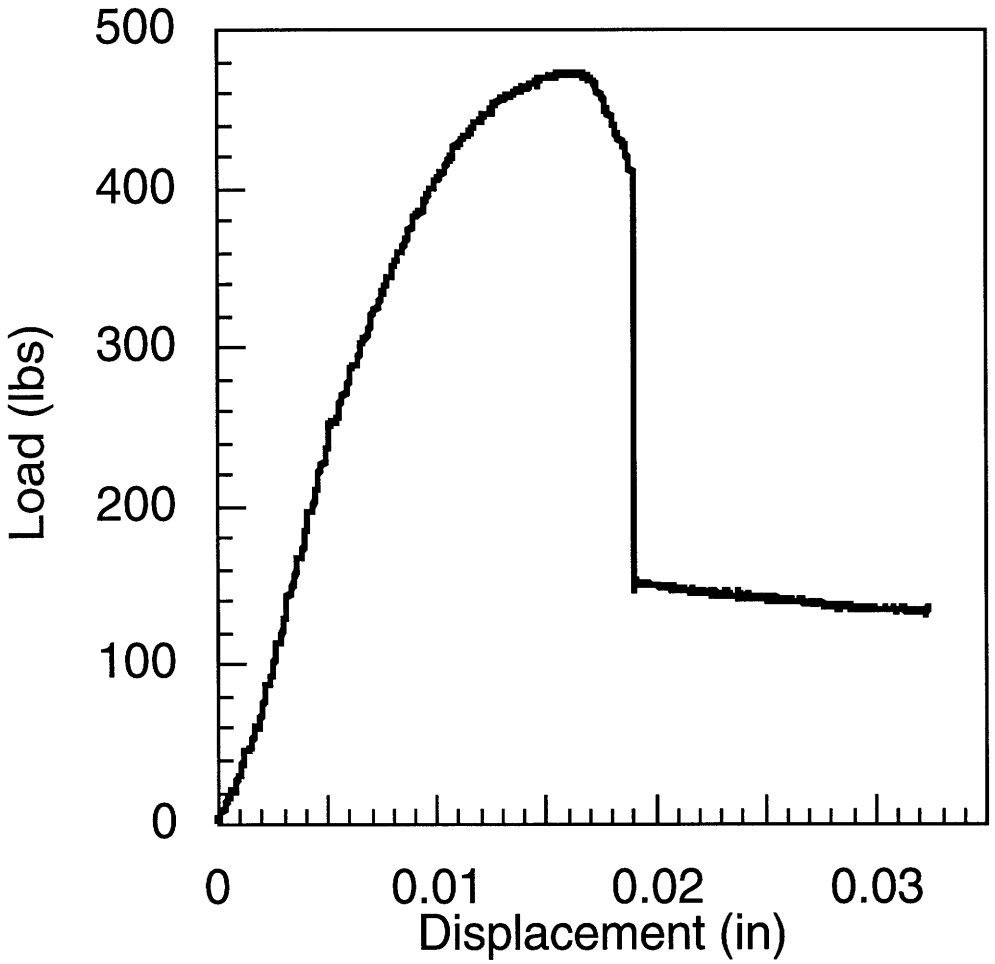


**Figure B.13: Load-Displacement Curve for 2 Inch Wide Panel**

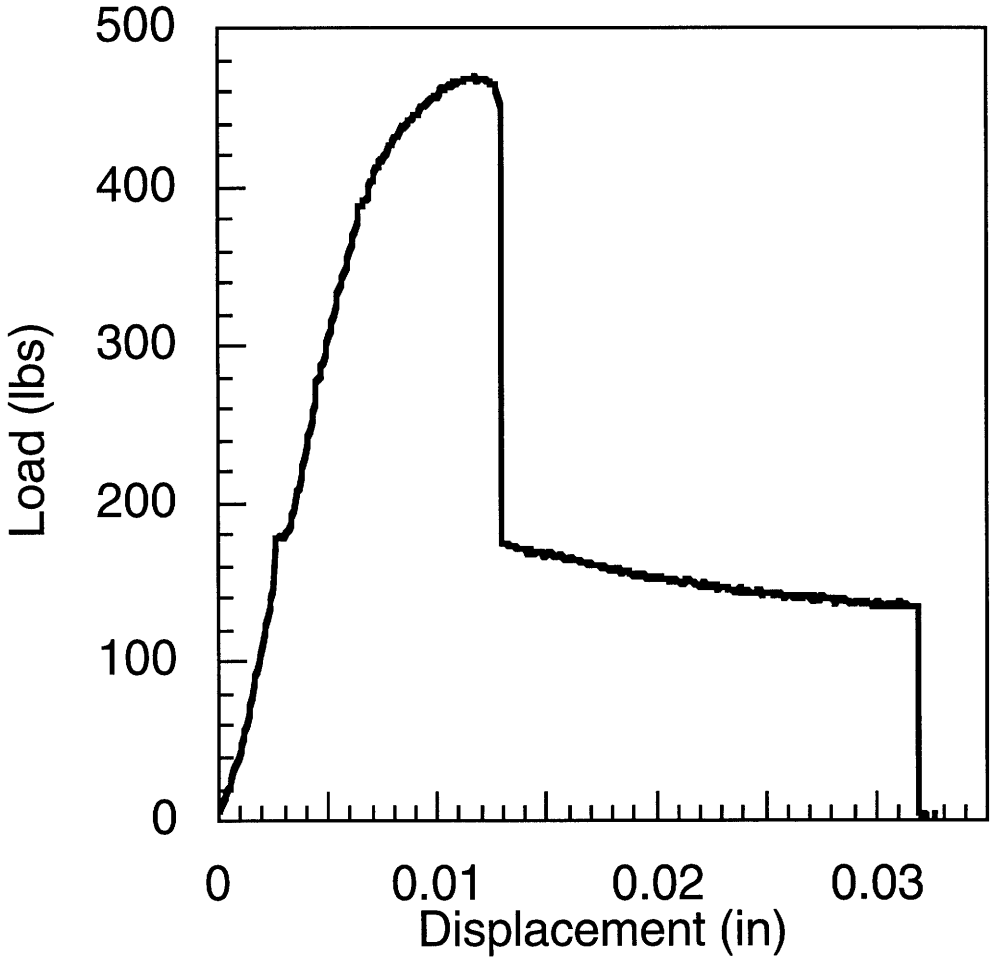


**Figure B.14: Load-Displacement Curve for 2 Inch Wide Panel**

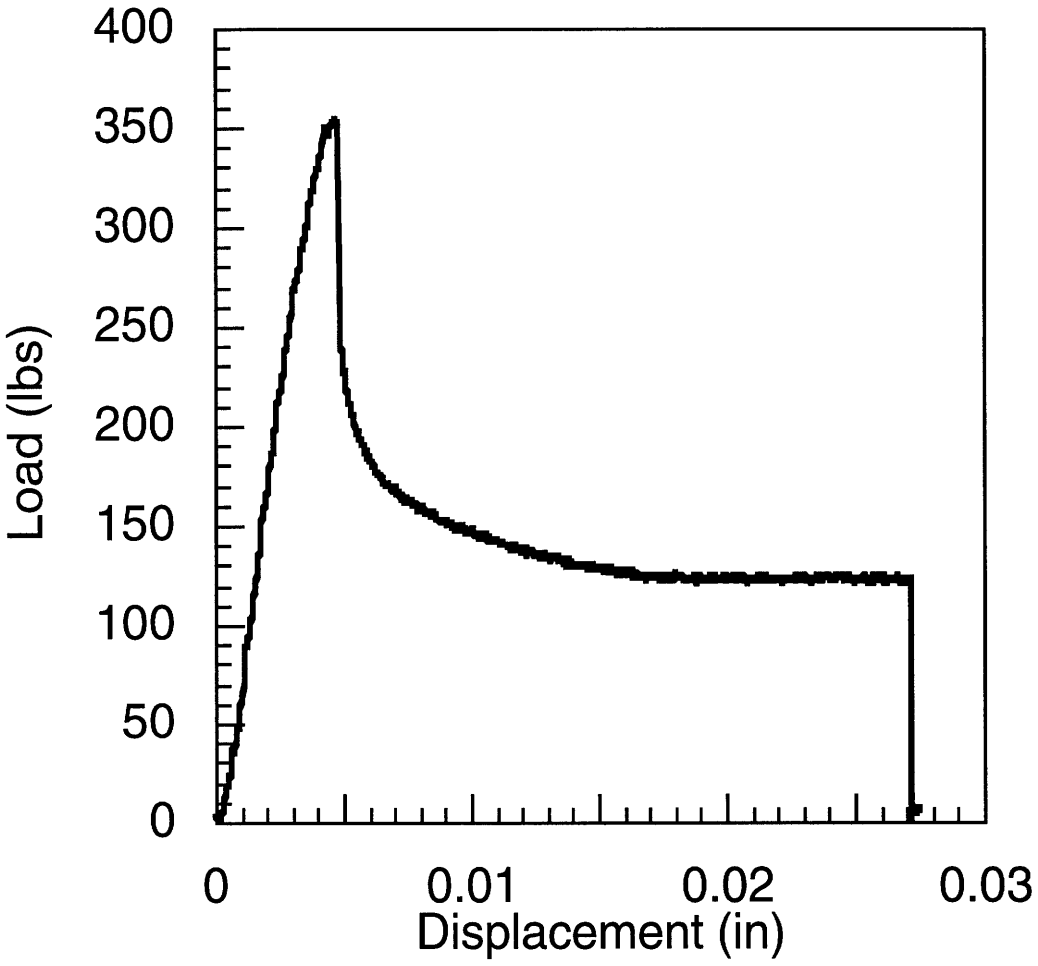


**Figure B.15: Load-Displacement Curve for 2 Inch Wide Panel**

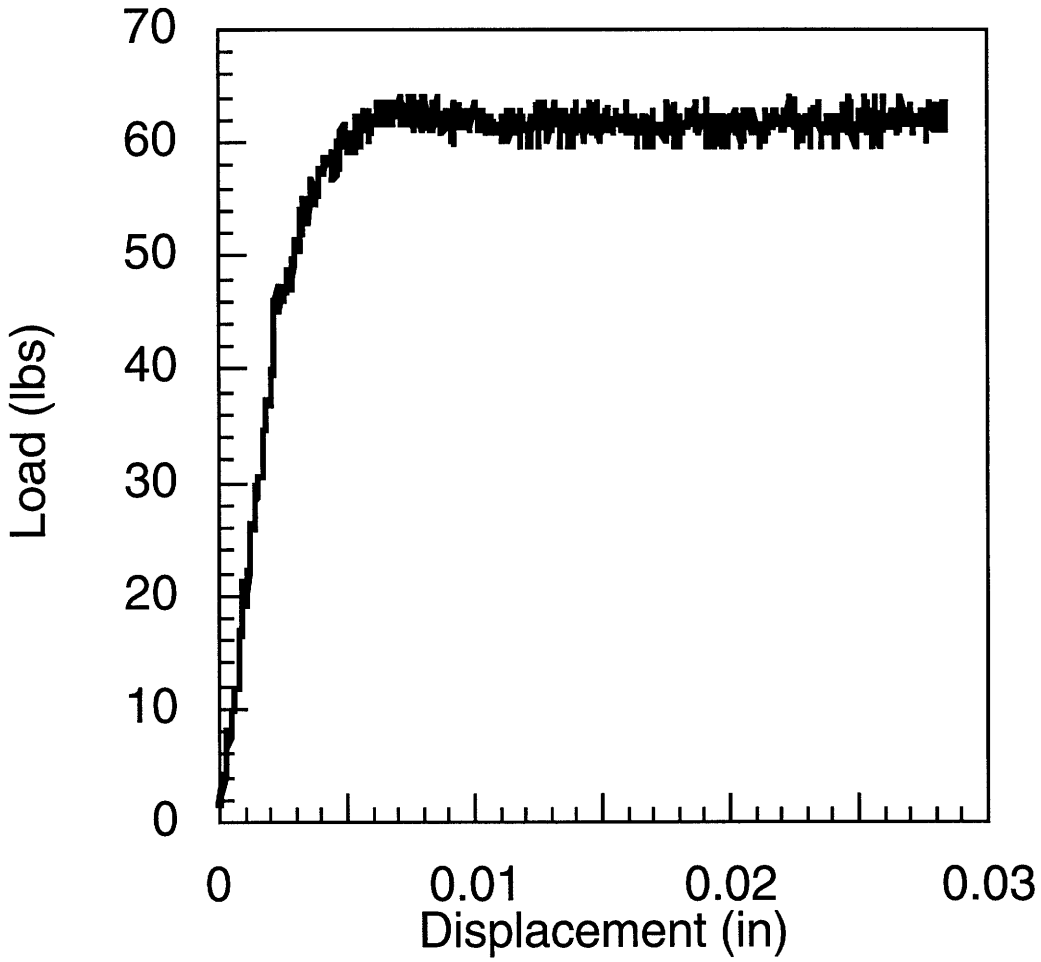


**Figure B.16: Load-Displacement Curve for 1 Inch Wide Panel**

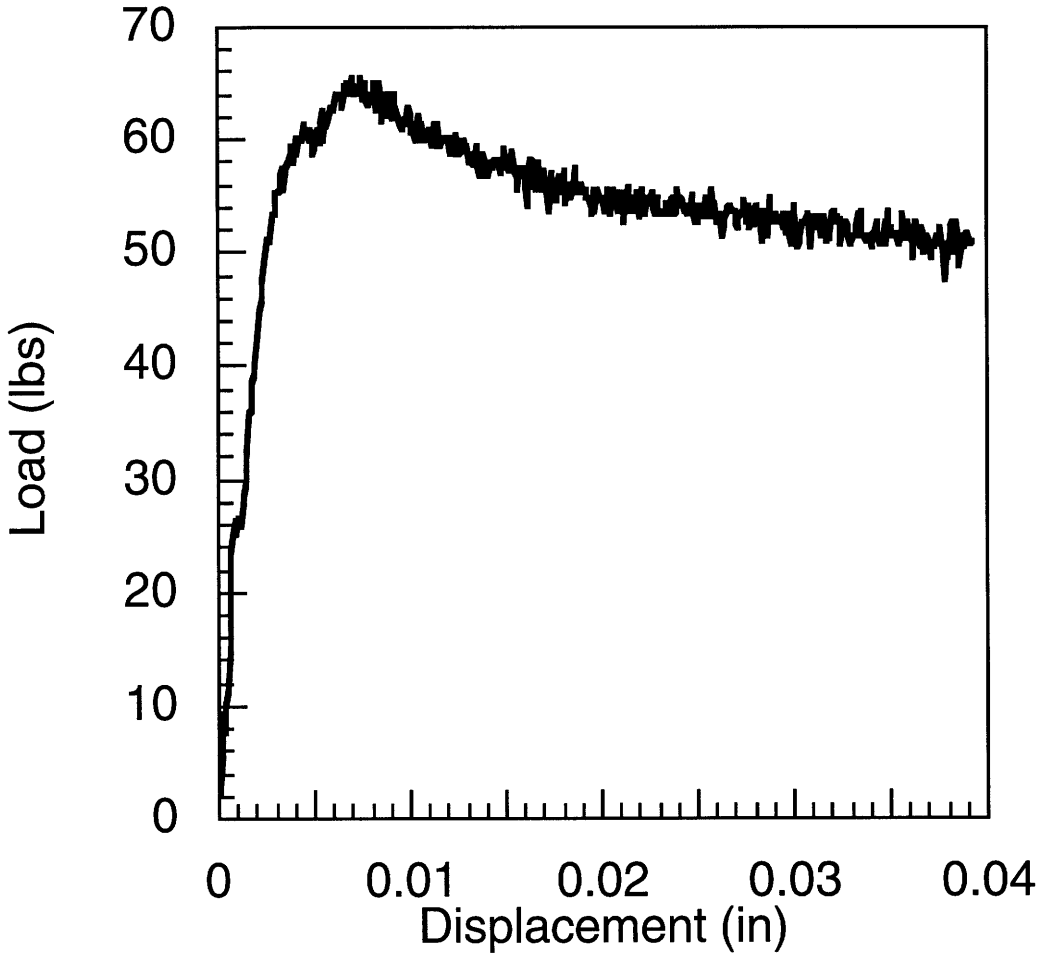


**Figure B.17: Load-Displacement Curve for 1 Inch Wide Panel**

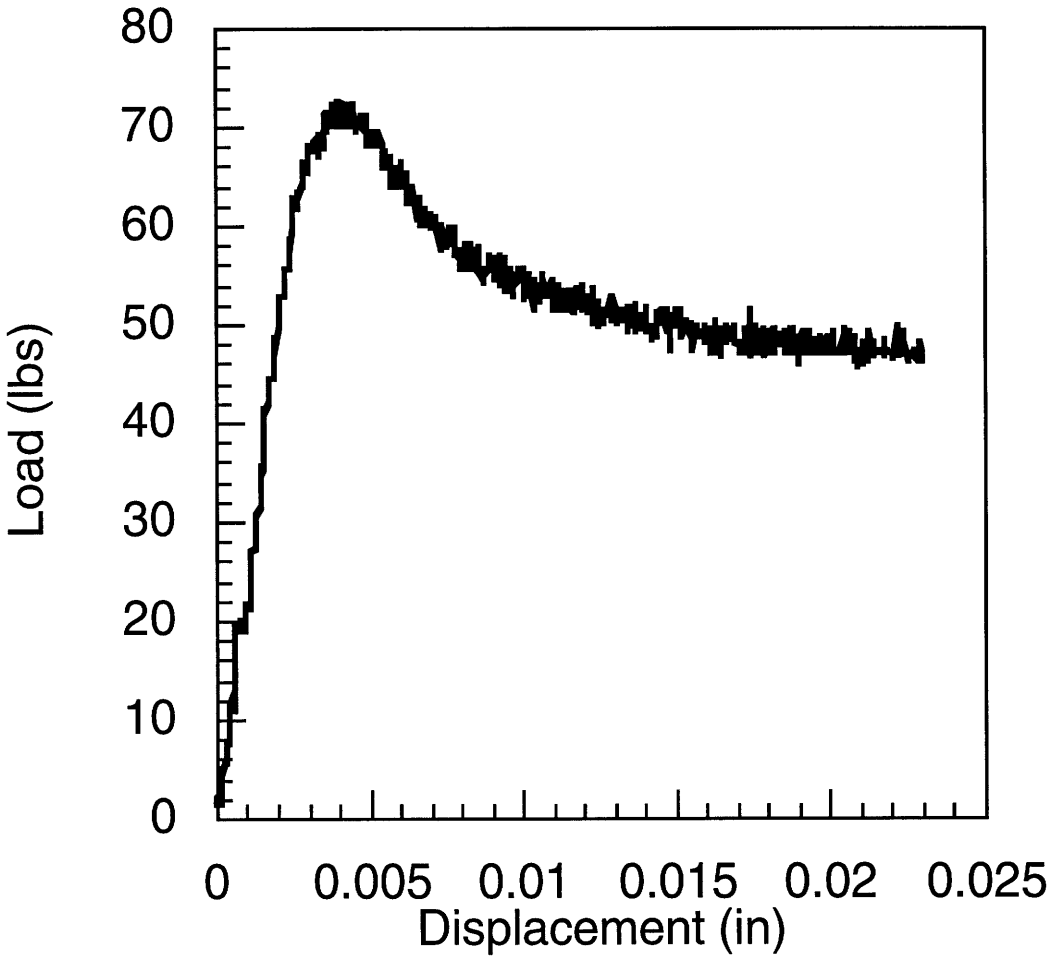


**Figure B.18: Load-Displacement Curve for 1 Inch Wide Panel**

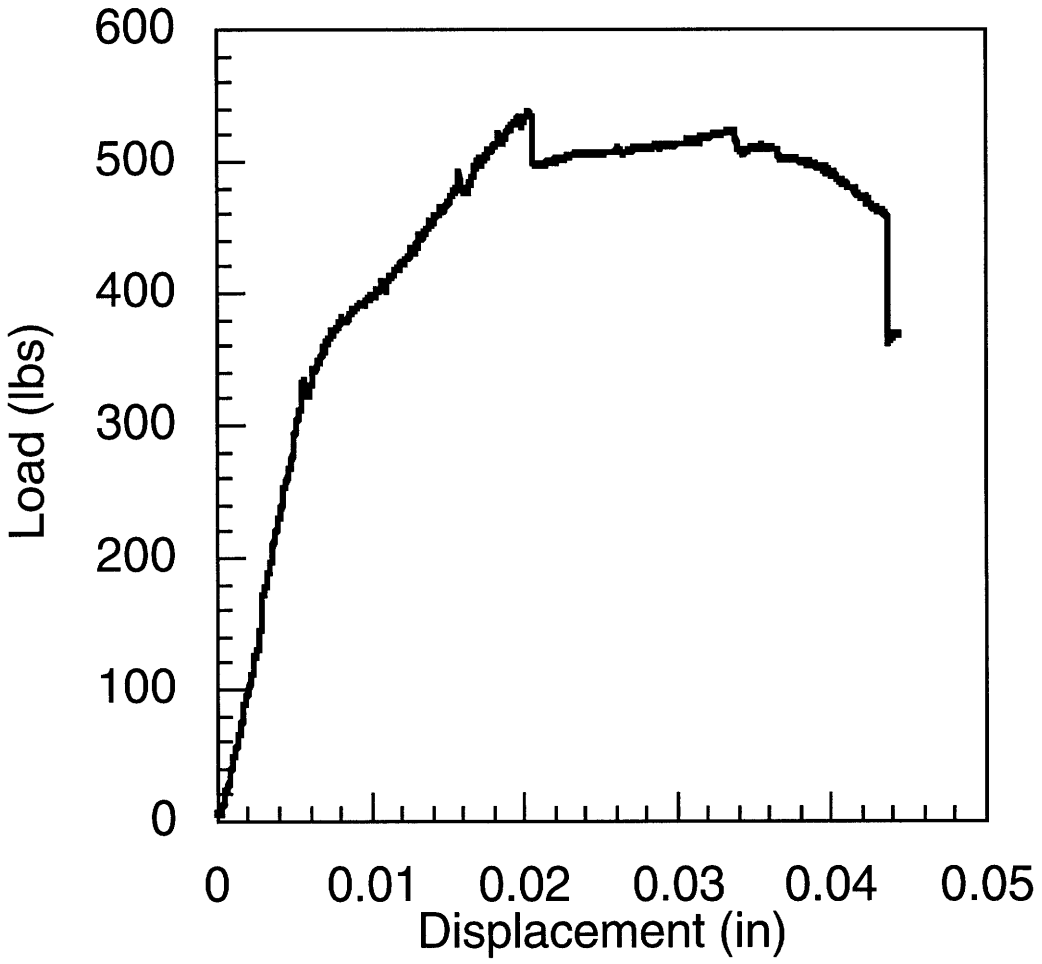


**Figure B.19: Load-Displacement Curve for 4 Inch Long Panel**

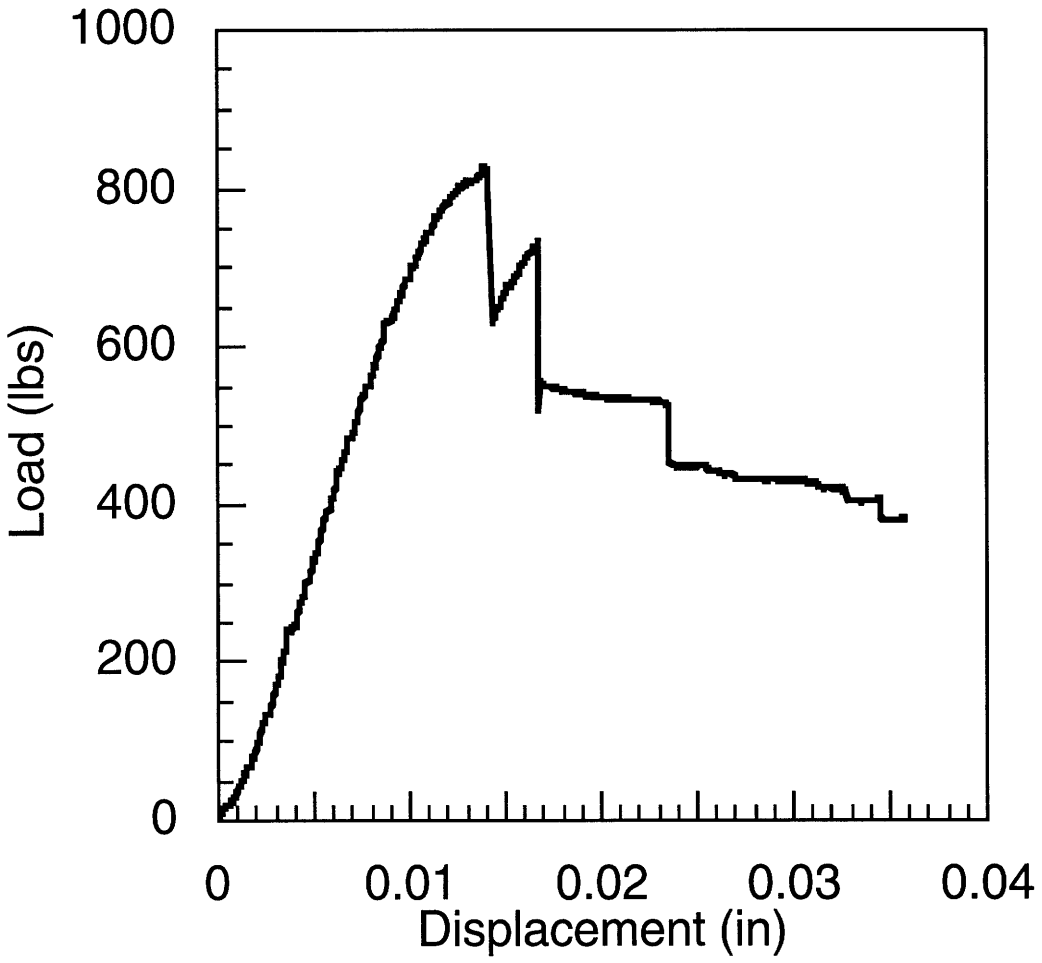


**Figure B.20: Load-Displacement Curve for 4 Inch Long Panel**

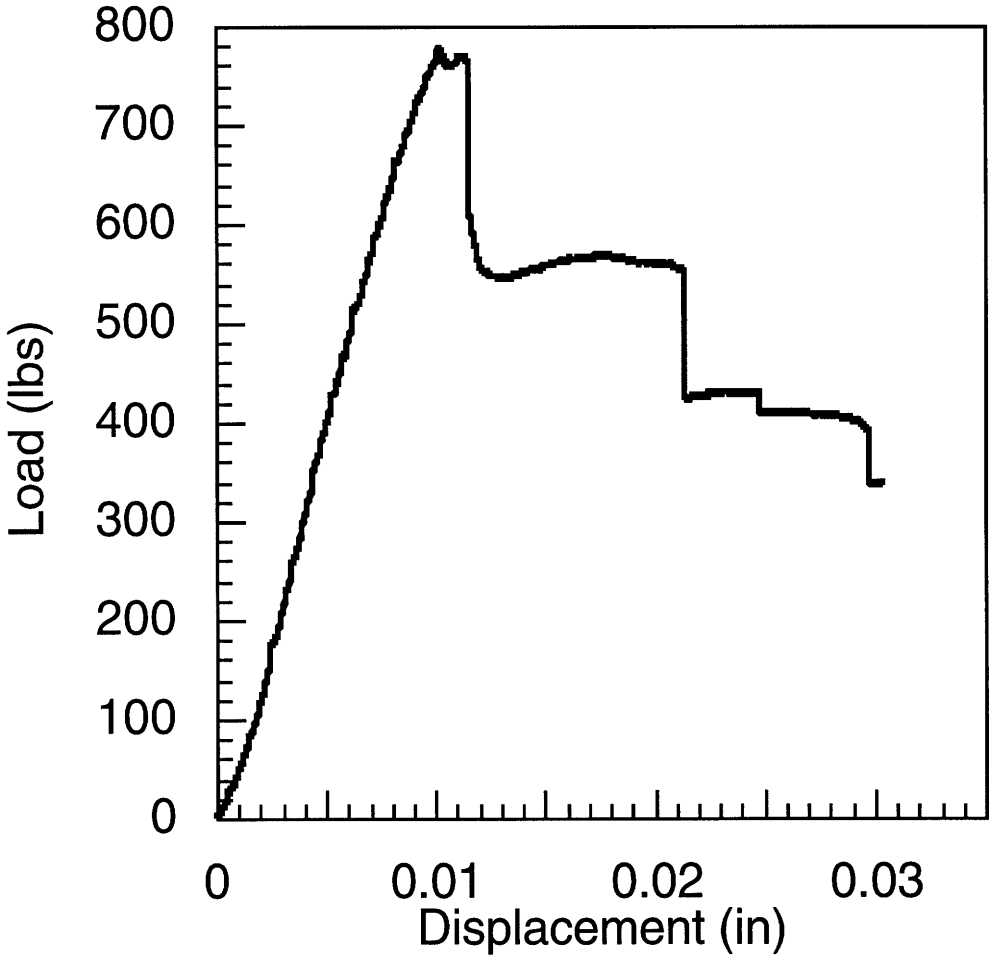


**Figure B.21: Load-Displacement Curve for 4 Inch Long Panel**

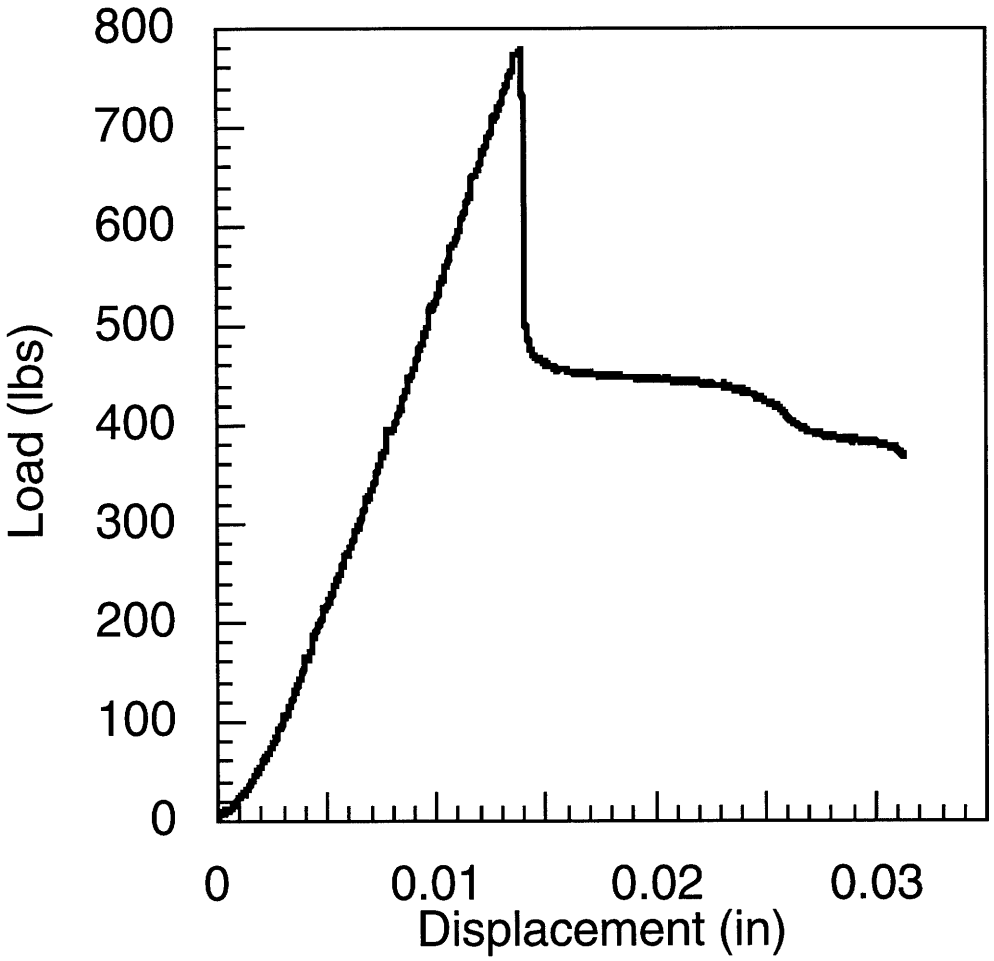


**Figure B.22: Load-Deflection Curve for 5 Inch Long Panel**

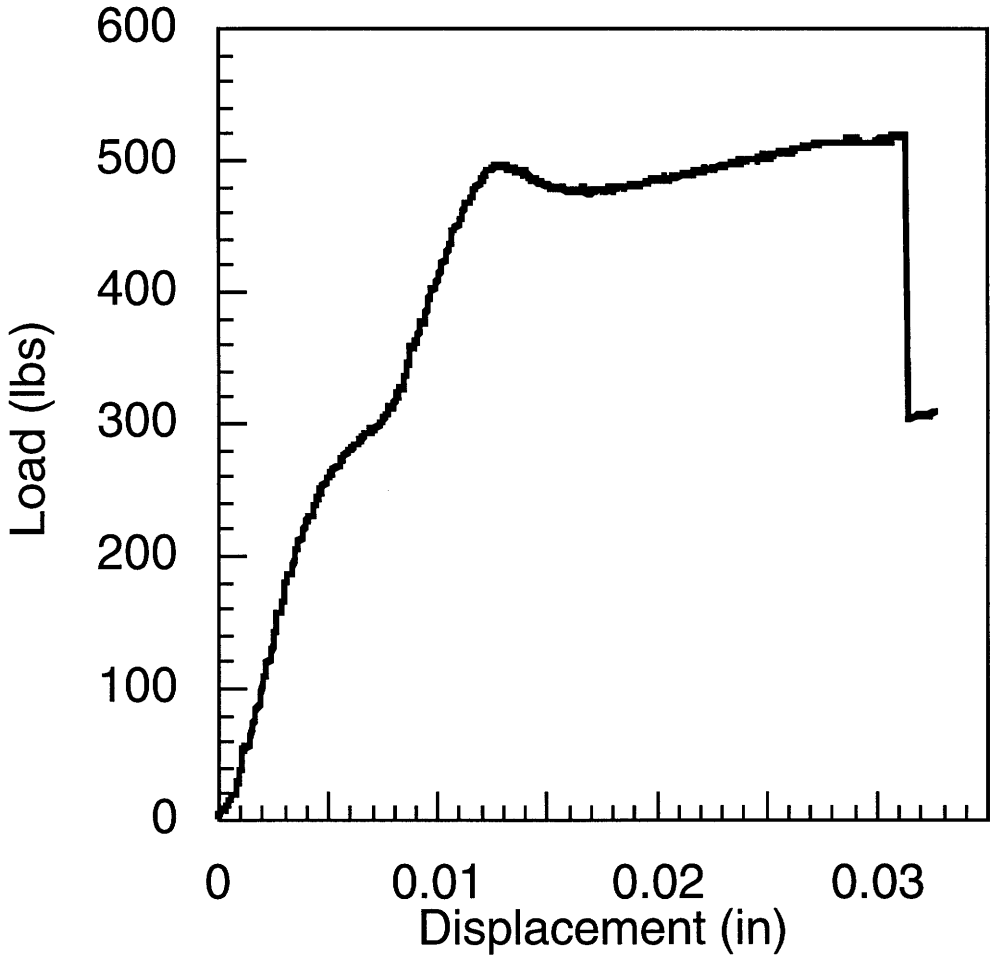


**Figure B.23: Load-Displacement Curve for 5 Inch Long Panel**

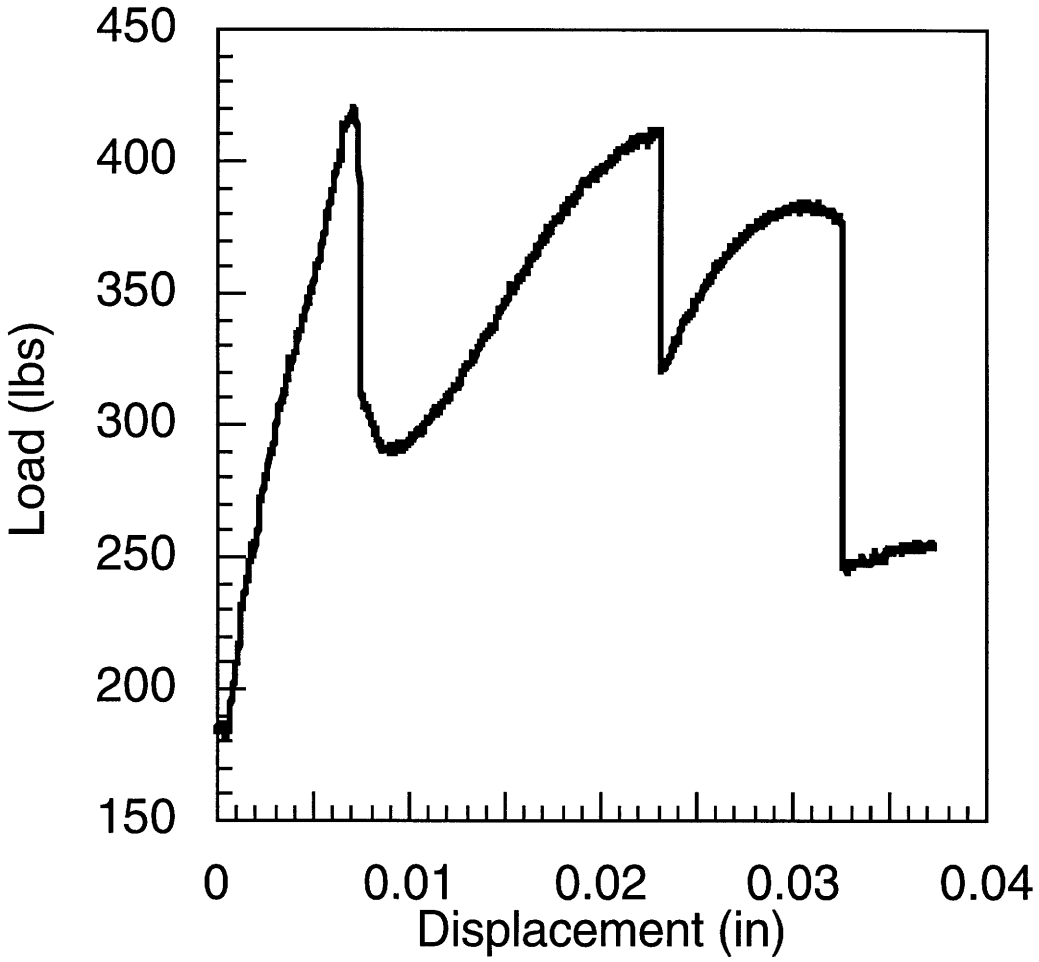


**Figure B.24: Load-Displacement Curve for 5 Inch Long Panel**